

ISSN 1732-9353 (suspended)
eISSN 2543-7496

Scientific Review

Engineering and Environmental Sciences

Przegląd Naukowy
Inżynieria i Kształtowanie Środowiska

Vol. 31 (1)

2022
Quarterly

Issue 95

SCIENTIFIC REVIEW
ENGINEERING AND ENVIRONMENTAL SCIENCES

Quarterly

EDITORIAL BOARD

Kazimierz Adamowski (University of Ottawa, Canada), **Kazimierz Banasik – Chairman** (Warsaw University of Life Sciences – SGGW, Poland), Andrzej Ciepiewski (Warsaw University of Life Sciences – SGGW, Poland), Tomáš Dostál (Czech Technical University in Prague, Czech Republic), Vidmantas Gurklys (Aleksandras Stulginskis University, Kaunas, Lithuania), Małgorzata Gutry-Korycka (University of Warsaw, Poland), Zbigniew Heidrich (Warsaw University of Technology, Poland), Silvia Kohnova (Slovak University of Technology, Bratislava, Slovak Republic), Andrzej J. Kosicki (Maryland State Highway Administration, Baltimore, USA), Hyosang Lee (Chungbuk National University, Korea), Athanasios Loukas (University of Thessaly, Volos, Greece), Jurík Luboš (Slovak Agriculture University, Nitra, Slovak Republic), Viktor Moshynskyi (National University of Water Management and Nature Resources Use, Rivne, Ukraine), Magdalena Daria Vaverková (Mendel University in Brno, Czech Republic)

EDITORIAL OFFICE

Tomasz Gnatowski (Deputy-chairman), Weronika Kowalik, Paweł Marcinkowski (Editorial Assistant Environmental Sciences), Katarzyna Pawluk, **Mieczysław Połoński (Chairman)**, Magdalena Daria Vaverková, Grzegorz Wierzbicki, Grzegorz Wrzesiński (Editorial Assistant Engineering Sciences)

The list of reviewers is published in the last issue of the volume and on the <https://srees.sggw.edu.pl>

EDITORIAL OFFICE ADDRESS

Wydział Budownictwa i Inżynierii Środowiska SGGW, ul. Nowoursynowska 159, 02-776 Warsaw, Poland
tel. (+48 22) 59 35 363, 59 35 210, 59 35 302
e-mail: srees@sggw.edu.pl
<https://srees.sggw.edu.pl>

ISSN 1732-9353 (suspended)
e-ISSN 2543-7496

Electronic version of the Scientific Review Engineering and Environmental Sciences is primary version

All papers are indexed in the data bases as follows: AGRO(Poznań), BazTech, Biblioteka Nauki, **CrossRef**, **DOAJ**, **Google Scholar**, **Index Copernicus**, INFONA, POL-Index, **SCOPUS**, SIGZ(CBR)

Scientific Review

Engineering and Environmental Sciences

Przegląd Naukowy
Inżynieria i Kształtowanie Środowiska

Vol. 31 (1)

2022

Issue 95

Contents

MOHAMED YUSOF M.K.T., SHARIPUDIN S.S., MOHAMMAD S.N., ROSLAN A., MICHAEL Z., SHAHRUL AZHAR I.I., ZAINAL ABIDIN N.A.: Feasibility study of palm oil boiler ash (POBA) as a partial replacement of sand in foamed concrete	3
Al-REKABI W.S., Al-KHAFAJI S.A., JANNA H.: Impact of dissolved oxygen on hospital wastewater quality treated by SBBR in Basrah city, Iraq	14
STEJSKALOVÁ L., ANSORGE L., KUČERA J., ČEJKA E.: Role of wastewater treatment plants in pollution reduction – evaluated by grey water footprint indicator	26
KORYTÁROVÁ J., HANÁK T.: Analysis of road construction projects price changes in the selected phases of their life-cycle	37
DUSHI M., BERILA A.: Determining the influence of population density on the land surface temperature based on remote sensing data and GIS techniques: application to Prizren, Kosovo	47
NGOC N.M., CUONG P.H., SON T.T., NAM N.V., PHONG N.T.: Experimental study of the hydraulic jump length in a smooth trapezoidal channel	63

© Copyright by Wydawnictwo SGGW, Warsaw 2022

Editorial work – Anna Dołomisiewicz, Violetta Kaska

ISSN 1732-9353 (suspended) eISSN 2543-7496

Mohamed Khatif Tawaf MOHAMED YUSOF¹✉  <https://orcid.org/0000-0001-6929-122X>

Siti Shahidah SHARIPUDIN¹  <https://orcid.org/0000-0003-1278-3084>

Shahrul Nizam MOHAMMAD¹  <https://orcid.org/0000-0002-5720-7964>

Azmi ROSLAN²  <https://orcid.org/0000-0002-8201-2923>

Zeno MICHAEL³  <https://orcid.org/0000-0002-3880-0148>

Ilya Izyan SHAHRUL AZHAR³  <https://orcid.org/0000-0002-3033-658X>

Nurrul Amilin ZAINAL ABIDIN³  <https://orcid.org/0000-0001-7376-478X>

¹ Universiti Teknologi MARA, College of Engineering, School of Civil Engineering, Malaysia

² Universiti Teknologi MARA, College of Engineering, School of Chemical Engineering, Malaysia

³ Universiti Teknologi MARA, College of Engineering, School of Mechanical Engineering, Malaysia

FEASIBILITY STUDY OF PALM OIL BOILER ASH (POBA) AS A PARTIAL REPLACEMENT OF SAND IN FOAMED CONCRETE

Key words: foamed concrete, palm oil boiler ash (POBA), sand replacement, compressive strength, water absorption

Introduction

Aside from integrating natural fiber materials into foamed concrete matrix, industrial by-products derived from agricultural crops are considered as feasible resources in the expansion of an environmentally friend-

ly and sustainable concrete. Each unwanted waste produced due to agricultural activities has distinguished properties that make them suitable in proper application in concrete. The wastes include oil palm kernel shell (OPKS), coconut shell, fly ash (Rashad, 2016), rice husk ash (RHA), and oil palm shell (OPS) (Mannan & Ganapathy, 2004). Those are referred to as additional cementitious materials due to their pozzolanic properties that improve the mechanical properties of solid concrete (Awang, Al-Mulali, Khalil

& Aljoumaily, 2014). On the other hand, the integration of industrial by-products in the foamed cellular concrete structure matrix also can aid in the establishment of the number of pores, thus creating a lighter product. By combining the effects of pozzolanic activity and pores generation in foamed concrete matrix, it will improve thermal conductivity, lightweightedness of foamed concrete, and compressive strength of foamed concrete. Malaysia is one of the world's largest producers of palm oil, where the industry generates large quantities of solid waste such as palm oil boiler ash (POBA). These oil palm wastes have contributed to a major disposal problem to the society and environment. On the other hand, global demand for concrete is expected to keep increasing and the price of concrete materials are escalating due to limited resources of cement, such as fine aggregate and coarse aggregate.

The scenario is a good opportunity to utilise POBA to be blended with foamed concrete as an alternative to the conventional high priced concrete materials. The utilisation of POBA in foamed concrete has a huge potential to reduce the weight of concrete with acceptable strength instead of being disposed of as waste materials. A few researches have been carried out to resolve the shortage of natural sand and the upsurge in the waste's disposal problems (Flores-Johnson & Li, 2012; Sankh, Biradar, Naghathan & Ishwargol, 2014; Payá et al., 2017; Castillo-Lara et al., 2020; Tran & Ghosh, 2020). By utilising those waste into the concrete blends creates opportunity in solving environmental issues. For instance, utilising oil palm shell (OPS), coconut shell, and oil palm kernel shell (OPKS) as aggregates in concrete (Awang et al., 2014; Muthusamy, Zamri, Zubir, Kushbiantoro & Ahmad, 2015) or using rice husk ash and palm oil fuel ash (POFA) as cement

replacement material (Lim, Tan, Lim & Lee, 2013), however only a few use the wastes as sand replacement in producing concrete. In 2014, there are studies where the properties of foamed concrete replaced by the semi-processed oil palm ash or POFA (Awang et al., 2014) and another study (Muthusamy et al., 2015) using POFA as cement replacement in the application of lightweight concrete. More study on 20% of POFA as cement replacement has been conducted in 2010 with different fineness where it was concluded that 20% of POFA as cement replacement but different fineness has improved the strength of POFA concrete towards the acidic corrosion (Budiea, Hussin, Muthusamy & Ismail, 2010). POFA, if treated, will enhance the mechanical and physical properties of the concrete at initial phases, which has been proven by a recent study (Alsubari, Shafigh, Ibrahim & Jumaat, 2018).

Also, it is reported that replacing the sand with coarse fly ash as filler in the foamed concrete showed a spread value 2.5 times higher than that of cement-sand mix (Jones & McCarthy, 2005b; Lim et al., 2013). If POBA can be used as sand replacement in concrete for structural applications, it would be favourable to the environment by turning these materials into an appropriate product. In addition, this concrete can be employed for construction of low-cost houses, particularly in the locality of oil palm plantations. However, the flexural behaviour and compressive strength of POBA as sand replacement in lightweight concrete must be further examined and clearly established for future development. Therefore, the objective of this study are to evaluate the feasibility of POBA as partial replacement material in foamed concrete and to determine the optimum composition of POBA to be used as sand replacement. The suitability of foamed concrete with POBA blends for conventional

concrete replacement will be determined with several tests that are being conducted which are water absorption test, density test, and compression strength test.

Methodology

Materials and sample preparation

The materials used in the laboratory to cast foamed concrete consist of original Portland cement according to the standard

BS EN 197-2000 (British Standards Institution [BSI], 2000), foaming agent, POBA, free water, and fine aggregate. POBA was collected from the Palm Oil Factory at Telok Sengat Palm Oil Mill, Kota Tinggi Johor as shown in Figure 1a and Figure 1b. The POBA was then sieved through a single size that is passing 2 mm sieve size to be used to replace sand. Preformed foamed concrete was made by using synthetic-based foaming agents. A foamed concrete with a $1,400 \text{ kg}\cdot\text{m}^{-3}$ density was designed in this study. The sand was replaced with POBA with various



FIGURE 1. Foamed concrete casting process: a, b – collection of POBA sample from Palm Oil Factory at Telok Sengat Palm Oil Mill; c – POBA sample passing 2 mm sieve; d – POBA-foamed concrete mix; e – cast into the mould; f – curing the foamed concrete sample

percentages of mass replacement such as 0, 4, 8 and 12% concerning designed density in this study. Detail of mix proportions of samples is shown in Table 1. All mixes were kept at 1.0 and 0.6 respectively for the ratios of the sand-cement (S/C) and water-cement/binder ratios. In this study, foamed concrete specimens with dimensions of $100 \times 100 \times 100$ mm were prepared. The samples were water curing in the water tank at 7, 28, 60 and 90 days. All processes are shown in Figure 1. Table 1 summarises the details of the mixed proportions of samples employed. Foamed concrete was prepared within four main steps, including the preparation of the mortar mix, foam preparation, foamed concrete production, and lastly density of the foamed concrete determination. Figure 1c to Figure 1e show the foamed concrete casting process conducted in this study. The density of the mixture was identified prior to the inclusion of the foam. Plastic density was set at about $\pm 50 \text{ kg} \cdot \text{m}^{-3}$ of the target density, which corresponds to the tolerance that is used in industry for the production of foamed concrete (Jones & McCarthy, 2005a, 2005b, 2006; Kearsley & Mostert, 2015). The additional foam was prepared as needed until the design density of the foamed concrete was achieved. The samples of the foamed concrete were cast based on guidelines in BS EN 12350-1:2009 (BSI, 2009). Portafoam was used as the foaming machine in this study to generate the foam from the foaming agent to be mixed with the concrete.

Test method

Water absorption test

Water-resistance in concrete is usually measured using water absorption tests. This test was performed in accordance with the standard BS 1881-122:2011 (BSI, 2011), which measures the water amount that penetrates the concrete samples while submerged. The positive result indicated by the lower absorption value of the concrete sample. The crystals inside the crystalline admixtures such as foamed concrete, grow continuously over time, which may affect the result of the water absorption test. Therefore, for more realistic and reliable results, the sample of the foamed concrete was tested at later ages (56 or 90 days) for its water absorption properties. Three samples of foamed concrete for each POBA mix proportion will be tested at the age of 90 days. The samples were placed in the drying oven for 72 h, as shown in Figure 2a. Then, the samples were weighed and recorded. The samples were submerged instantly in a water tank at a depth such that there was 25 ± 5 mm of water over the top of the specimen and in the position of its longitudinal axis in the horizontal as shown in Figure 2b. The sample was submerged in the water tank for a period of 30 ± 0.5 min. After that, the sample was removed from the tank and the bulk of water on the sample surface was removed by shaking the sample. Then the samples were dried up from the free water as rapidly as possible using a dry

TABLE 1. Detail of mix proportions of samples

Mixture sample	Mix proportion [$\text{kg} \cdot \text{m}^{-3}$]				Foaming agent [$\text{l} \cdot \text{m}^{-3}$]
	cement	fine aggregate	POBA	water	
Control	538	538	–	323	301.55
4 POBA	538	517	21	323	301.55
8 POBA	538	495	43	323	301.55
12 POBA	538	473	65	323	301.55



FIGURE 2. Water absorption test process: a – dry-oven the sample for 72 h; b – sample immersed in the water tank

cloth. Finally, the weight of the samples are recorded, and the percentage of water absorbed was calculated.

Uniaxial compressive strength

The compressive strength test was conducted using three samples of foamed concrete for each POBA mix proportion at the ages of 7, 28, 60 and 90 days. This test was conducted to assess the strength development of the samples with the different mix proportions of POBA, as shown in Figure 3. The size of the foamed concrete samples used in the test was $100 \times 100 \times 100$ mm, following the standard BS EN 12390-3:2009 (BSI, 2009). Compression testing machine (CTM) was used in this test and the foamed concrete

sample was positioned so that the load was applied in the opposing direction to the samples. The sample was carefully aligned and load was applied until the sample breaks. The compressive strength of a specimen was determined and recorded.

Density determination

Foamed concrete with a density of $1,400 \text{ kg}\cdot\text{m}^{-3}$ was prepared in this research. The density of foamed concrete was determined after the foamed was added to the mixture. The mixture of foamed concrete was poured into a mould and then weighed to get the wet density of the mixture. If the density was higher than $1,400 \text{ kg}\cdot\text{m}^{-3}$, it means that the amount of foamed was not

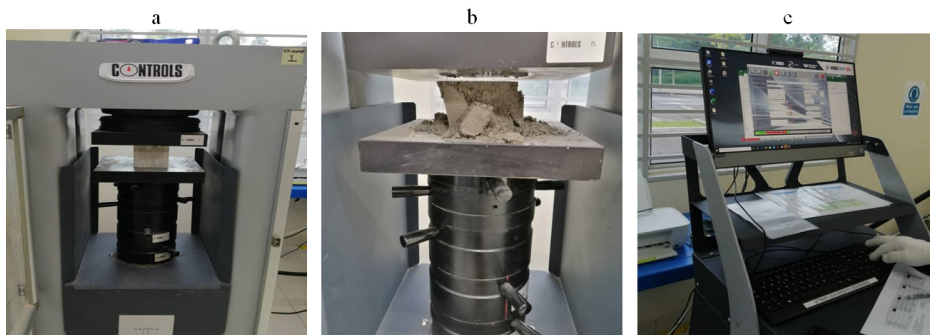


FIGURE 3. Uniaxial compressive strength process: a – sample placed in position; b – load applied until failure; c – maximum load at failed

yet sufficient in the mixture and additional foam was added before it was mixed again in the concrete mixer. Then, the mixture was poured into the mould and weighed again until the desired density was achieved. After the curing process, the foamed concrete was left to dry before the weight was determined once more. Based on the weight reading, the dry density of foamed concrete was determined.

Result and discussion

Density of the sample

Figure 4 shows the density of foamed concrete with 0, 4, 8 and 12% of POBA replacement of fine aggregate for the curing age of 7, 28, 60 and 90 days. The density are recorded lowest for foamed concrete without POBA as fine aggregate replacement, which are 1,294.7, 1,306.8, 1,358.2 and 1,362.1 $\text{kg}\cdot\text{m}^{-3}$ at 7, 28, 60 and 90 days of curing age respectively. Meanwhile, the density for foamed concrete with 12% of POBA as fine aggregate replacement recorded the highest values with 1,446.5, 1,541.0, 1,552.0 and 1,604.3 $\text{kg}\cdot\text{m}^{-3}$ at the similar curing days. Additionally, the

value of density for foamed concrete with 4% of POBA are 1,323.3, 1,345.6, 1,399.0 and 1,389.1 $\text{kg}\cdot\text{m}^{-3}$, meanwhile for foamed concrete with 8% of POBA the recorded density are 1,387.0, 1,435.5, 1,448.4 and 1,454.3 $\text{kg}\cdot\text{m}^{-3}$ for the curing age of 7, 28, 60 and 90 days respectively.

In this research, it was found that the greater percentage of POBA as replacement of fine aggregate lead to a higher value of dry density of the foamed concrete. It is because the amount of foam added in the foamed concrete is lesser for the higher percentage of POBA in foamed concrete as the density of fine aggregate is greater than POBA. Therefore, mixture with higher percentage of POBA will be added with less amount of foam so that the value of wet density of foamed concrete fixed to 1,400 $\text{kg}\cdot\text{m}^{-3}$. Thus, the sample with higher percentage of POBA will be added with less amount of foam, which dries out and create less voids in the foamed concrete during curing process. On the other hand, this research found that the value of density of foamed concrete rises with the increase of curing days. The trend shows that longer curing days will result in the higher value of density for most samples of foamed concrete.

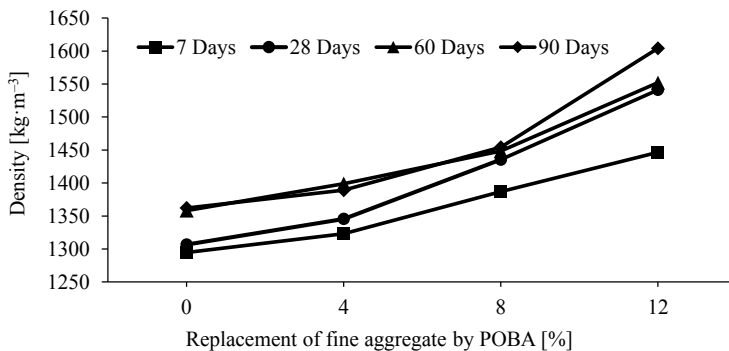


FIGURE 4. Density of the foamed concrete sample

This indicates that the uniformity of foamed concrete enhanced with the increase of curing days. As a result, the dry density of foamed concrete increase with the increase of curing days. This finding is true according to previous research that has been conducted that found water loss from concrete decreases with increasing curing days (Memon, Sam, Awang & Memon, 2018).

Water absorption test

Table 2 shows the percentage of water absorption by various percentages of POBA. The result found that the foamed concrete with 12% POBA as the sand replacement showed the highest percentage of water absorption (10.4%), while the control sample showed the lowest value.

The trend on the water absorption shown in Figure 5 indicates that the increasing amount of POBA in the foamed concrete will increase the water absorption value in the foamed concrete sample. Standard con-

crete has a mean water absorption value within a range of 3–4% and this value is expected to be much higher in foamed concrete due to the higher number of voids or porosity values in foamed concrete (Brady, Watts & Jones, 2001). The average value of water absorption for all the samples that contain POBA is 9.5% and the replacement of POBA as partial replacement of sand in foamed concrete showed an overall 28% of increment of water absorption value. This higher amount of porosity in foamed concrete depends on the concentration of the foaming agent that is being used and also the mix design proportion where its density plays an important role which has a major influence on the physical and mechanical properties of the sample such as water absorption value and compression strength.

Moreover, POBA loses some of its element during the hydration process and is diluted in water as an ion. The hydration reaction consumes these ions, forming ettringite and calcium silicate hydrate (C-S-H).

TABLE 2. Water absorption value for foamed concrete sample

Concrete sample	Criteria	Sample number				AVG
		1	2	3	4	
Control	dry weight [kg]	1 110.3	1 111.1	1 139.5	1 150.5	1 127.9
	saturated weight [kg]	1 200.8	1 199.3	1 233.0	1 239.2	1 218.1
	% of water absorbed	7.5	7.4	7.6	7.2	7.4
4%	dry weight [kg]	1 105.8	1 103.5	1 095.1	1 117.1	1 105.4
	saturated weight [kg]	1 189.1	1 196.5	1 178.9	1 206.5	1 192.8
	% of water absorbed	7.5	8.4	7.7	8.0	7.9
8%	dry weight [kg]	1 167.4	1 186.2	1 187.0	1 185.6	1 181.6
	saturated weight [kg]	1 278.2	1 311.9	1 306.3	1 309.8	1 301.6
	% of water absorbed	9.5	10.6	10.1	10.5	10.2
12%	dry weight [kg]	1 250.5	1 253.5	1 213.3	1 257.9	1 243.8
	saturated weight [kg]	1 372.2	1 386.7	1 343.4	1 390.1	1 373.1
	% of water absorbed	9.7	10.6	10.7	10.5	10.4

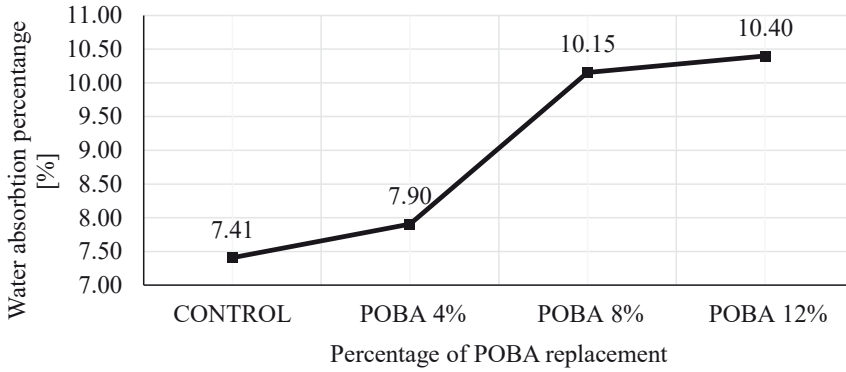


FIGURE 5. POBA and water absorption relationship

As a result, the size of POBA will reduce and has a greater tendency to leave void space during that dilution, which increases porosity in foam concrete that enhances the water absorption process.

Compressive strength

The compressive strength of foamed concrete mixes for all proportions of POBA is presented in Table 3. Besides that, Figure 6 shows the graphical compressive strength of all concrete in relation to the 4, 8 and 12% of POBA amounts. Based on the data obtained, it appears that replacing sand with palm oil boiler ash improves the strength of foamed concrete significantly. POBA foamed concrete has a higher compressive strength than the control mixture, as indicated in Table 3 and Figure 6. The compressive

strength consistently increased in the range of 4.34–13.50 N·mm⁻², when the varied amounts of POBA were increased up to 12% at all curing periods. It can also be noticed that POBA foamed concrete for all replacement levels also develops strength at a slower rate at 7 days, with values ranging from 4.34 to 5.87 N·mm⁻². According to Figure 6, it shows the strength of those concretes at 90 days increased dramatically, ranging from 5.20 to 13.50 N·mm⁻². As a result of this finding, the POBA did have a role in the later development of strength. This is in agreement with the study conducted by Abdul Munir et al. (2015). Those authors mentioned that the rate of increase in strength of foamed concrete containing palm oil fuel ash (POFA) is slower than that of the normal concrete due to the use of POFA can slow the early hardening process. Additionally, Figure 6 reveals

TABLE 3. Compressive strength results of the foamed concrete mixes

Concrete mix	Compressive strength after curing time [N·mm ⁻²]			
	7 days	28 days	60 days	90 days
Control	4.23	4.40	5.39	4.70
4% POBA	4.34	4.70	5.87	5.20
8% POBA	4.81	6.40	7.89	8.60
12% POBA	5.87	9.80	10.51	13.50

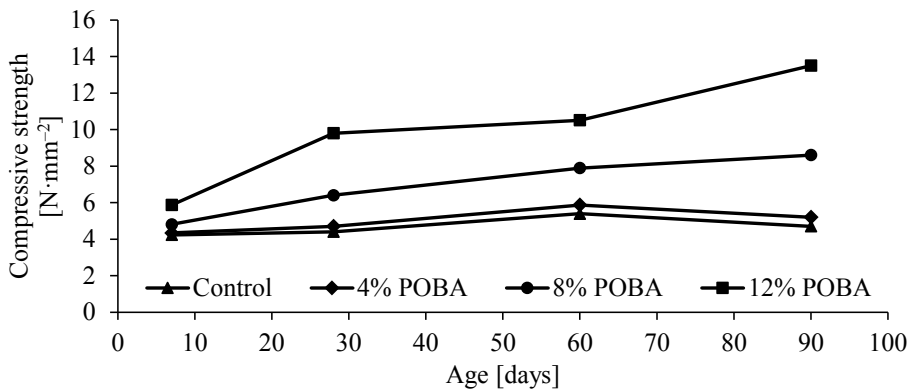


FIGURE 6. POBA and compressive strength relationship

that when POBA content was substituted at 12%, the compressive strength achieved was higher than the other specimens, with values of 5.87, 9.80, 10.51 and 13.50 $\text{N}\cdot\text{mm}^{-2}$ at 7, 28, 60 and 90 days respectively.

As a result, it obtains the maximum strength gain compared to the control mixture. This finding is achievable because C-S-H gels in the POBA produces bonding between aggregates and cement, resulting in increased concrete strength (Yee, 2017). At the same time, the fine particles in POBA are useful as a filler to fill voids in concrete (Yuan, 2012). Thus, the density of the concrete would be increased, which would aid in the development of strength. It's worth noting that foamed concrete can withstand larger levels of POBA without sacrificing strength.

Conclusions

The present study on utilising palm boiler ash (POBA) as sand replacement in concrete blends shows a promising result in lightweight foamed concrete development. Compression and water absorption tests were carried out on foamed concrete and POBA foamed con-

crete as sand replacement at 4, 8 and 12% of mass fractions with dry density of foamed concrete at $1,400 \text{ kg}\cdot\text{m}^{-3}$. The conclusions that can be deduced from this study:

- The inclusion of POBA has found to increase the compressive strength of the concrete blends, which was associated to the bonding between the aggregates and cement. The void in the concrete is filled with the fine particle of POBA which acts as filler and thus contributes to the compressive strength of the concrete. This can be seen from the results obtained, that among the three percent of replacement, 12% of POBA as sand replacement has been found to attribute the highest compressive strength.
- POBA percentage has showed a proportionally relationship to the dry density of foamed concrete mixture. The density of the foamed concrete with 12% of POBA resulted in the highest values of all percentages of POBA replacement. The integration of POBA in the foamed cellular concrete structure matrix has been found to aid in the establishment of the number of pores, thus creating a lightweight product with higher compressive strength.

The use of POBA in lightweight concrete would be qualified to reduce the amount of solid waste disposed by the palm oil industry to the environment. From this study, it is feasible to use POBA as a supplementary cementing material, however, further research on the effect of different POBA particle sizes to the compressive strength of the concrete mixture and the stability of concrete to the temperature treatment should be conducted for future research and development.

Acknowledgements

This work was supported by the Bestari Research Grant Scheme Phase 2/2020 [600-UiTM CJ (PJA.5/2)] awarded by the UiTM Cawangan Johor, Kampus Pasir Gudang, 81750 Masai, Johor.

References

- Alsubari, B., Shafiqh, P., Ibrahim, Z. & Jumaat, M. Z. (2018). Heat-treated palm oil fuel ash as an effective supplementary cementitious material originating from agriculture waste. *Construction and Building Materials*, 167, 44–54. <https://doi.org/10.1016/j.conbuildmat.2018.01.134>
- Awang, H., Al-Mulali, M. Z., Khalil, H. A. & Aljoumaily, Z. S. (2014). Utilisation of oil palm ash in foamed concrete. *MATEC Web of Conferences*, 15, 2–7. <https://doi.org/10.1051/mateconf/20141501033>
- British Standards Institution [BSI] (2000). Cement. Composition, specifications and conformity criteria for common cements (BS EN 197-2000). London: British Standards Institution.
- British Standards Institution [BSI] (2009). Testing hardened concrete. Compressive strength of test specimens (BS EN 12390-3:2009). London: British Standards Institution.
- British Standards Institution [BSI] (2011). Testing concrete. Method for determination of water absorption (BS 1881-122:2011). London: British Standards Institution.
- Brady, K. C., Watts, G. R. A. & Jones, M. R. (2001). *Specification for foamed concrete*. Crowntrone, UK: TRL Ltd.
- Budiea, A., Hussin, M., Muthusamy, K. & Ismail, M. (2010). Performance of High Strength POFA Concrete in Acidic Environment. *Concrete Research Letters*, 1 (1), 14–18.
- Castillo-Lara, J. F., Flores-Johnson, E. A., Valadez-Gonzalez, A., Herrera-Franco, P. J., Carrillo, J. G., Gonzalez-Chi, P. I. & Li, Q. M. (2020). Mechanical properties of natural fiber reinforced foamed concrete. *Materials*, 13 (14), 3060. <https://doi.org/10.3390/ma13143060>
- Flores-Johnson, E. A. & Li, Q. M. (2012). Structural behaviour of composite sandwich panels with plain and fibre-reinforced foamed concrete cores and corrugated steel faces. *Composite Structures*, 94 (5), 1555–1563. <https://doi.org/10.1016/j.compstruct.2011.12.017>
- Jones, M. R. & McCarthy, A. (2005a). Preliminary views on the potential of foamed concrete as a structural material. *Magazine of Concrete Research*, 57 (1), 21–31. <https://doi.org/10.1680/macr.2005.57.1.21>
- Jones, M. R. & McCarthy, A. (2005b). Utilising unprocessed low-lime coal fly ash in foamed concrete. *Fuel*, 84 (11), 1398–1409. <https://doi.org/10.1016/j.fuel.2004.09.030>
- Jones, M. R. & McCarthy, A. (2006). Heat of hydration in foamed concrete: Effect of mix constituents and plastic density. *Cement and Concrete Research*, 36 (6), 1032–1041. <https://doi.org/10.1016/j.cemconres.2006.01.011>
- Kearsley, E. P. & Mostert, H. F. (2015). Designing mix composition of foamed concrete with high fly ash contents. In: R.K. Dhir, M.D. Newlands & A. McCarthy (Eds.), *Use of Foamed Concrete in Construction: Proceedings of the International Conference held at the University of Dundee, Scotland, UK on 5 July 2005* (pp. 29–36). London: Thomas Telford Publishing.
- Lim, S. K., Tan, C. S., Lim, O. Y. & Lee, Y. L. (2013). Fresh and hardened properties of lightweight foamed concrete with palm oil

- fuel ash as filler. *Construction and Building Materials*, 46, 39–47. <https://doi.org/10.1016/j.conbuildmat.2013.04.015>
- Mannan, M. A. & Ganapathy, C. (2004). Concrete from an agricultural waste-oil palm shell (OPS). *Building and Environment*, 39 (4), 441–448. <https://doi.org/10.1016/j.buildenv.2003.10.007>
- Memon, R. P., Sam, A. R. M., Awang, A. Z. & Memon, U. I. (2018). Effect of Improper Curing on the Properties of Normal Strength Concrete. *Engineering, Technology & Applied Science Research*, 8 (6), 3536–3540. <https://doi.org/10.48084/etasr.2376>
- Munir, A., Abdullah, Huzaim, Sofyan, Irfandi & Safwan (2015). Utilization of palm oil fuel ash (POFA) in producing lightweight foamed concrete for non-structural building material. *Procedia Engineering*, 125 (December), 739–746. <https://doi.org/10.1016/j.proeng.2015.11.119>
- Muthusamy, K., Zamri, N., Zubir, M. A., Kusbi-antoro, A. & Ahmad, S. W. (2015). Effect of Mixing Ingredient on Compressive Strength of Oil Palm Shell Lightweight Aggregate Concrete Containing Palm Oil Fuel Ash. *Procedia Engineering*, 125, 804–810. <https://doi.org/10.1016/j.proeng.2015.11.142>
- Payá, J., Monzó, J., Borrachero, M. V., Soriano, L., Akasaki, J. L. & Tashima, M. M. (2017). New inorganic binders containing ashes from agricultural wastes. In: H. Savastano Jr, J. Fiorelli & S. Francisco dos Santos (Eds.), *Sustainable and Nonconventional Construction Materials Using Inorganic Bonded Fiber Composites* (pp. 127–164). Sawston: Woodhead Publishing. <https://doi.org/10.1016/B978-0-08-102001-2.00006-1>
- Rashad, A. (2016). Cementitious materials and agricultural wastes as natural fine aggregate replacement in conventional mortar and concrete. *Journal of Building Engineering*, 5, 119–141. <https://doi.org/10.1016/j.jobe.2015.11.011>
- Sankh, A. C., Biradar, P. M., Naghathan, S. J. & Ishwargol, M. B. (2014). Recent trends in replacement of natural sand with different alternatives. *IOSR Journal of Mechanical and Civil Engineering*, 1, 59–66.
- Tran, Q. & Ghosh, P. (2020). Influence of pumice on mechanical properties and durability of high performance concrete. *Construction and Building Materials*, 249, 118741. <https://doi.org/10.1016/j.conbuildmat.2020.118741>
- Yee, S. Y. (2017). *Optimum replacement ratio of reincinerated palm oil fuel ash (Repofa) mortar without sacrifice its properties*. Kampar: Faculty of Engineering and Green Technology. Retrieved from <http://eprints.utar.edu.my/2586>
- Yuan, L. O. (2012). *Engineering properties of lightweight foamed concrete incorporated with Palm Oil Fuel Ash (POFA)*. Universiti Tunku Abdul Rahman, Kampar [BEng project report]. Retrieved from <http://eprints.utar.edu.my/id/eprint/509>

Summary

Feasibility study of palm oil boiler ash (POBA) as a partial replacement of sand in foamed concrete. A study was conducted to explore the effect of palm oil boiler ash (POBA) on foamed concrete by varying the percentage of POBA over sand quantities (0, 4, 8 and 12%). This paper primarily discusses the water absorption test, uniaxial compressive strength, and dry density findings. It indicates that substituting sand with POBA greatly enhances the strength of foamed concrete. When the quantity of POBA was raised up to 12% throughout all curing times, the compressive strength steadily increased in the range of 4.34–13.50 N·mm⁻². Furthermore, the dry density of foamed concrete was shown to be directly related to the fraction of POBA in the mixture. The dry density of foamed concrete increases as the amount of POBA increases. Despite this, water absorption shown that increasing POBA increases water absorption percentage in foamed concrete from 7.4 to 10.4%. This is due to the fact that a composition with a high POBA percentage will generate more pores than a mixture with a low POBA percentage.

Wisam S. Al-REKABI¹

Samar A. Al-KHAFAJI¹

Hussein JANNA²  <https://orcid.org/0000-0002-7635-7992>

¹ University of Basrah, College of Engineering, Iraq

² University of Al-Qadisiyah, Civil Engineering Department, Iraq

IMPACT OF DISSOLVED OXYGEN ON HOSPITAL WASTEWATER QUALITY TREATED BY SBBR IN BASRAH CITY, IRAQ

Key words: hospital wastewater, SBBR, laboratory experiment, COD, DO, TN, TSS, TP

Introduction

Hospital wastewater (HWW) is created by all hospital activities, including medical, and non-medical activities such as surgery, emergency & first aid, laboratory, diagnosis, radiography, cooking, and laundry (Majlesi, 2001; Zgórska & Grabińska-Sota, 2019). Microorganisms that cause disease as (viruses and bacteria), residuals of medication and chemical materials used in hospital laboratories (chloroform, phenol, antibiotics, and others), toxic chemicals, and organic substances biodegradable which is found in hospital wastewater (protein, fat, carbohydrate) (Radha, Kalaivani & Lavanya, 2009).

Each hospital in the developed country produces daily 400–1,200 l per capita of wastewater, comparison with 100–400 l per capita of daily municipal sewage production, whilst in developing countries, daily value is 200–400 l per capita (Mishra, Sharma, Sarita & Ayub, 2016; Yong, Bashir, Ng, Sethupathi & Lim, 2018).

Generally, the properties of hospital wastewater are the same as those of domestic wastewater, although a part of hospital wastewater contains toxic/non-biodegradable/infectious contaminants (Sharma et al., 2015). The effluent of hospitals is commonly discharged into municipal sewage systems and frequently dumped without any treatment to reduce public health risks in developing countries (Timraz, Xiong, Al Qarni & Hong, 2017).

A biological treatment method for removing pharmaceuticals is a more cost-

 Hussein.janna@qu.edu.iq



-effective and ecologically friendly alternative to ozonation and activated carbon (Zorita, Mårtensson & Mathiasson, 2009). There are two types of biological wastewater treatment processes: suspended growth and attached growth. Suspended growth biological treatment, such as the activated sludge treatment utilized in most WWTPs, is a common example of this type of treatment. In spite of several improvements that have been reported for conventional activated sludge (CAS) (Schaar, Clara, Gans & Kreuzinger, 2010), on the other hand, numerous microorganisms, are considerably persistent in the treatment by the activated sludge method (Miège, Choubert, Ribeiro, Eusèbe & Coquery, 2009). In comparison to the activated sludge, some of these chemicals have been removed with better clearance rates in attached biofilm procedures (Zupanc et al., 2013). This shows that the biological treatment process may be further optimized, by utilizing a biofilm-based technique whereby sequencing batch biofilm reactor (SBBR) is one practical way to take advantage of the attached growth processes.

In aerobic wastewater biological treatment, oxygen serves as a terminal electron acceptor. In the activated sludge process, dissolved oxygen (DO) is an essential parameter. Low DO can enhance filamentous bacteria growth, resulting in poor sludge settleability, reduce extracellular polymer synthesis, and reduce nitrifying activities and in most cases, the reactor's DO should be kept above $2 \text{ mg} \cdot \text{l}^{-1}$ (Dangcong, Bernet, Delgenes & Moletta, 2001).

The SBBR is based on attaching microorganisms for biological wastewater treatment. It depends on the sequence batch reactor (SBR). Because of its different advantages, SBBR is extensively researched and used as a recent biological sewage treatment technol-

ogy, there has been an increase in biomass, but there has been minimal sludge, simple and easy to operate, and efficient in sewage treatment (Gieseke, Arnz, Amann & Schramm, 2002; Jasem, Jumaha & Ghawi, 2018).

The objective of this research is to utilize the potential of the SBBR as a type of attached growth biological processes reactor to treat the hospital wastewater from a local hospital at Basrah city (south of Iraq) to remove a different pollutant parameter such as COD, TN, $\text{NH}_3\text{-N}$, and TP under variation of dissolved oxygen (DO) with range of $2.15\text{--}6.55 \text{ mg} \cdot \text{l}^{-1}$ and then compared the results of SBBR with international standards of effluent sewage.

Material and methods

Reactor set-up and operation

The reactor used in this experiment is a laboratory bench-scale SBBR vessel with a cylindrical shape, the volume approximately 26.0 l with an internal diameter is 300 mm, a depth is 400 mm, and the working volume is 13.0 l. SBBR, is made from transparent plastic material of 4.0 mm thickness to easily monitor sludge and biofilm in the SBBR tank. The wastewater was fed from the bottom into the SBBR reactor as illustrated in Figure 1. Plastic fibrous filler units were attached to the reactor, which length is 300 mm with many strands of fiber. During aeration in the SBBR vessel, flexible fiber thread swayed with the wastewater to increase absorption in the biofilm, and many filaments were diffused to produce a large surface area. An air pump was used to supply air to the SBBR reactor. The aeration air sprays were positioned at the top of the sedimentation zone to permit big particles

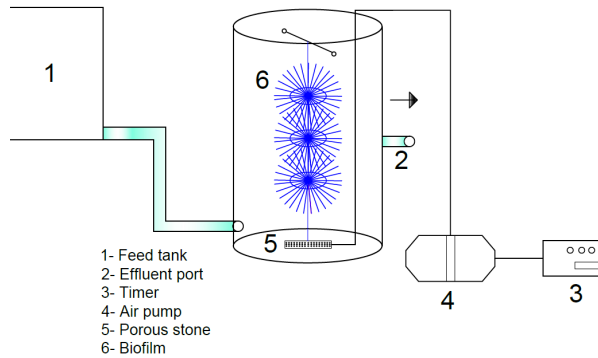


FIGURE 1. SBBR system schematic (adopted from Al-Rekabi, 2021)

that were not attached to the biofilm to settle during the aeration operation (Al-Rekabi, Al-Khafaji, Hassan & Janna, 2021).

Activated sludge was collected from a local municipal wastewater treatment plant as seeds material for the SBBR system. Timers were used to monitor the operation of reactor processes such as feeding, aeration, settling, and discharge. A cover was placed over the reactor, but it was not sealed, and an air pump was used to create an aeration condition.

Usually, biofilm carriers influence the condition of microorganisms in the SBBR, which is an important property for the reactor's proper startup.

Even though biofilm helps microorganisms the attachment, it as well serves as filters, keeping suspended solids (SS) and other pollutants out of the treated water area (Dinçer & Kargi, 2001).

The operation cycle of the SBBR was 8/24 h. The operation of the SBBR was divided into (0.5-hour fill, 6.0-hour reaction time, 1.0-hour settle time, and 0.5-hour settles time). When the aerator was powered up, it allowed the DO of the reactor to be kept at 2.15–6.55 mg·l⁻¹. During the period of starting up one month to create a biofilm on fibers filler, the SBBR research test period

lasted about one month. The SBBR was operated for approximately one month to guarantee that the biological treatment processes were overripe and that start-up conditions were reached.

Analytical methods and collection samples

Dissolved oxygen, pH and temperature (the device was calibrated using standard solutions prior to measurement) were examined by a digital device. The COD, BOD, TSS, TDS, TP, NH₃-N and TN under the standard method (American Public Health Association [APHA], 1998). The samples tests are analyzed by using DR_{5,000} and DR_{1,900} Hach spectrophotometric. The samples of wastewater are filtered by using filter paper (pore size 0.45 μm) when the test needs that.

For this research, samples were gathered from the SBBR influent and effluent in a cleaned plastic bottle adopting standard methods (APHA, 1998). Samples were taken one time a day at (12 a.m.) throughout October and the beginning of November. All of the samples were analyzed immediately after the samples were collected with a field device, and the other duplicate samples were

kept in a fridge at 5°C in the sanitary laboratory at the University of Basrah’s College of Engineering.

Result and discussion

In this study, raw wastewater was collected from one of the outlet points of a man-hole in the Al-Taalemie hospital in Basrah 400 beds, Iraq. For the present study, the important properties of hospital wastewater components are compared with universal concentrations of wastewater (Table 1).

Concerning contaminants like COD, BOD, TSS, and TN, it indicates that raw sewage is more than medium concentration and less than high concentration. On the contrary, raw hospital wastewater has high concentrations with respect to contaminants such as TDS and NH₃-N. TDS level was higher because of rising saline in Basra’s drinking water supplies (United Nations Children’s Fund [UNICEF], 2019).

As during the acclimatization period, originally 6–8 l of activated sludge was a seed in the reactor without additives, the aeration is supplied using many diffusers, and for biofilm maturation, the concentration of DO is controlled higher than 3 mg·l⁻¹ during the aerobic condition, in accordance

with Rusten, Eikebrokk, Ulgenes and Lygren (2006), to keep the biofilm active in the normal conditions, they ensure a minimal level of DO equals to 3 mg of O₂ per 1 l in the reactor of SBBR. In the experiment operations, the exchange volume was put at 50% and the temperature was kept at 26–33°C to maintain the high performance of microorganisms, which has a substantial effect on their oxygen consumption ratio.

TSS removal

The SBBR was able to reduce total suspended solid perfectly as compared with normal bioreactors in hospital wastewater treatment plants, settling time has a significant impact on normal bioreactors that are dependent on gravity separation to remove TSS (Yong et al., 2018). SBBR’s reduced TSS is due to the presence of biofilm, which absorbs insoluble contaminants in the wastewater (Rittmann, 2017). To remove TSS, SBBR adsorption is a better option than the separation process. As a result, it’s thought that SBBR could help biological treatment by removal soluble recalcitrant chemicals and insoluble pollutants so that TSS removal efficiency was 91% conducted by SBBR for hospital wastewater in this study.

TABLE 1. Standard raw domestic wastewater concentrations comparison with Al-Taalemie hospital Wastewater characteristics in Basrah

Contaminants	Raw wastewater average values [mg·l ⁻¹]	SD	Concentrations of standard wastewater (Metcalf & Eddy, 2003)		
			low	medium	high
COD	550	7.12	250	430	800
BOD	280	7.48	110	190	350
TN	55	3.56	20	40	70
NH ₃ -N	44	2.90	12	25	45
TP	6.4	0.88	4	7	14
TDS	2325	4.97	270	500	860
TSS	225	2.16	120	210	400

Effect of dissolved oxygen on the removal of various pollutants

The aeration quantity was monitored in this research so that the DO level in the SBBR raised progressively from 2.15 to 6.55 mg·l⁻¹. Table 1 shows the quality of raw sewage at this phase. Aerobic conditions have a significant impact on COD, NH₃-N, TN and TP removals in microbiological investigations, and aeration with a medium volume is considered preferable for all pollutants removal except TP removal.

COD removal at different DO concentration

The SBBR was conducted periodically in an individualized bioreactor through anaerobic and aerobic operation, resulting in a balance of anaerobic and aerobic microorganisms that allowed for COD removal. COD elimination was attributable to the SBBR's efficient removal of organic materials; however, the SBBR also partially removed difficult compounds, resulting in COD removal that was higher than the hospital wastewater treatment plant. This finding confirms the theory that polychlorinated biphenyls can be successfully destroyed by alternating an-

aerobic and aerobic treatments (Pathiraja, Egodawatta, Goonetilleke & Te'o, 2019). When the COD concentration in the effluent reached 215 mg·l⁻¹, and the level of the DO was about 2.1 mg·l⁻¹, the water quality was bad. Concentrations of COD effluent considerably reduced to approximately 95 mg·l⁻¹ or as a result when the DO concentration was equal to 2.83 mg·l⁻¹ (Fig. 2).

Due to insufficiency of appropriate DO concentration, microbial behavior was decreased, and microorganisms were unable to degrade organic matter sufficiently in the case of insufficient oxygen. In this study, SBBR improved COD removal by decomposing refractory components in hospital wastewater including lignin and its derivatives. As a result, SBBR removed refractory chemicals more effectively than conventional bioreactors, resulting in improved COD and another pollutant removal which is existed in wastewater of hospitals.

COD removal efficiency by SBBR under different DO concentrations is shown in Figure 3. This figure shows that increasing DO concentration led to reducing COD concentration in effluent then COD removal efficiency increased so that the DO with

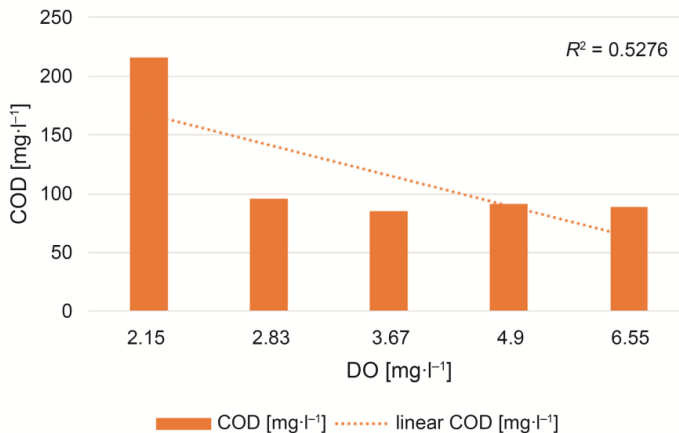


FIGURE 2. COD removal variation under different DO concentration

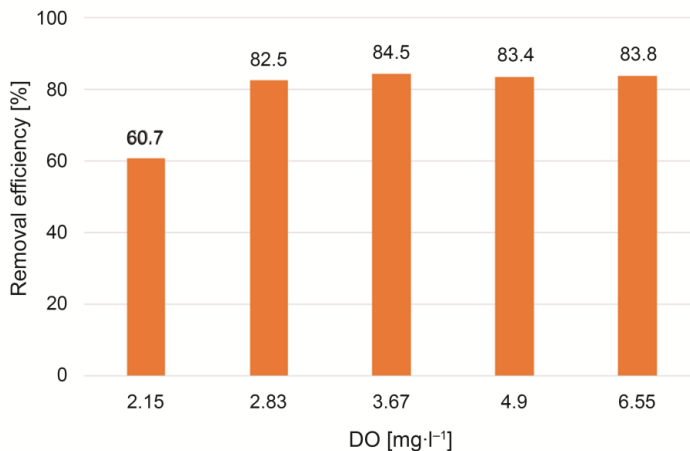


FIGURE 3. COD removal efficiency with different DO concentration

concentration value 3.67 mg·l⁻¹ is taken as the best effluent value with 84.55% removal efficiency.

NH₃-N and TN removal at different DO concentration

As shown in Figures 4 and 5, the concentration of the NH₃-N and TN was decreased by increased concentration of DO and reduced by TN's effluent levels

from 50 to 12 mg·l⁻¹ for DO concentrations 2.15 and 3.67 mg·l⁻¹ respectively. Although at 4.9 mg·l⁻¹ of DO concentration the level of NH₃-N in the effluent stays high and equal to 18 mg·l⁻¹, while for DO 6.55 mg·l⁻¹ the concentration of TN effluent has stayed low, the effluent content was 16 mg·l⁻¹.

In the SBBR reactor, microorganisms attach themselves to the fibrous membrane

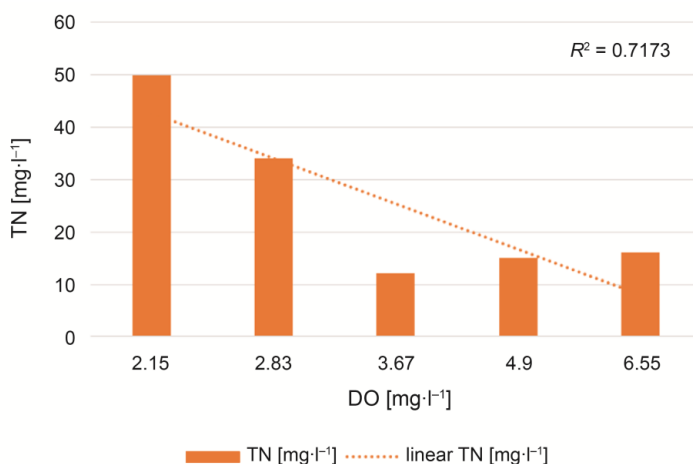


FIGURE 4. TN removal variation under different DO concentration

and then grow to become dense biological membranes. These are called biofilms. As the wastewater is attached to the biofilm, suspended organic particles are adsorbed on the biofilm surface, and because of the thickness of the biofilm, DO offers a gradient, necessitating a DO transfer process from the water to the zone of the biofilm. DO concentration in biofilms zone is very poor approximately equal to $2 \text{ mg}\cdot\text{l}^{-1}$ at the start of the research, which reduces the efficiency of aerobic nitrifying bacteria, for example, nitrification is not fully accomplished. As a result, the effluent contained high levels of $\text{NH}_3\text{-N}$ and TN, although, the rate at which oxygen is transferred to the biofilm is enhanced at higher DO levels equal to $4.9 \text{ mg}\cdot\text{l}^{-1}$.

The higher DO level extends the stratum of aerobic and compresses the stratum of anoxic, then increases the degradation rate for organic matter. As a result, all denitrification processes and sources of carbon are decreased, implying that denitrifying bacteria efficiency is reduced and nitrate nitrogen cannot be converted to nitrogen (Pochana, Keller & Lant, 1999; Marek, Pawęska & Bawiec, 2021). As a consequence, the efflu-

ent of TN concentration progressively raises. Effective TN removal takes place at DO approximately equal to $3.67 \text{ mg}\cdot\text{l}^{-1}$ according to the results of this research.

As shown in Figure 6, TN removal efficiency is increased with increased DO concentration until DO $3.674 \text{ mg}\cdot\text{l}^{-1}$ which give 78.18% as removal efficiency, while the removal efficiencies for DO 4.9 and $6.550 \text{ mg}\cdot\text{l}^{-1}$ is decreased to 72.73 and 70.91% respectively so that will be considered DO $3.67 \text{ mg}\cdot\text{l}^{-1}$ as the most suitable DO for TN removal in the operation of SBBR for hospital wastewater treatment in this research.

The $\text{NH}_3\text{-N}$ removal efficiencies are shown in Figure 7, this efficiency is increased clearly with increased DO especially for DO 2.15 and $2.83 \text{ mg}\cdot\text{l}^{-1}$ with removal efficiency 11.36 and 43.18%, while removal efficiency is increased slightly for DO 3.67, 4.9 and $6.55 \text{ mg}\cdot\text{l}^{-1}$ with removal efficiencies 65.9, 59.10 and 67.05% respectively, concerning these results the removal efficiencies of $\text{NH}_3\text{-N}$ was fairly good in the last three values for DO 3.67, 4.9 and $6.55 \text{ mg}\cdot\text{l}^{-1}$, this due to raising the rate of nitrification when

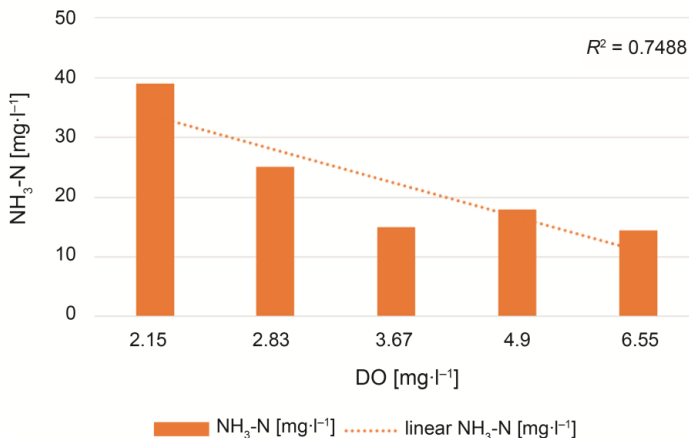


FIGURE 5. $\text{NH}_3\text{-N}$ removal variation under different DO concentration

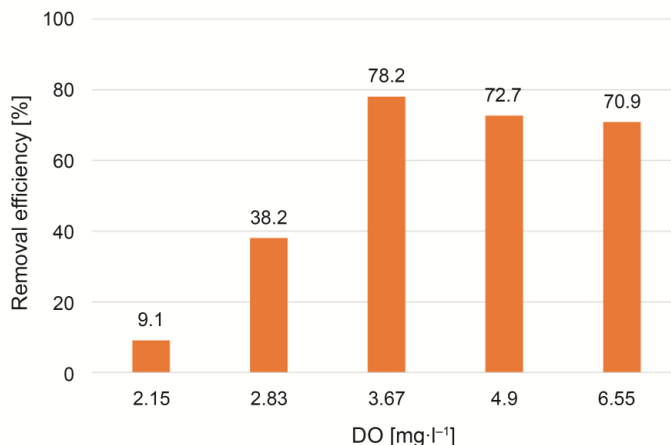


FIGURE 6. TN removal efficiency with different DO concentration

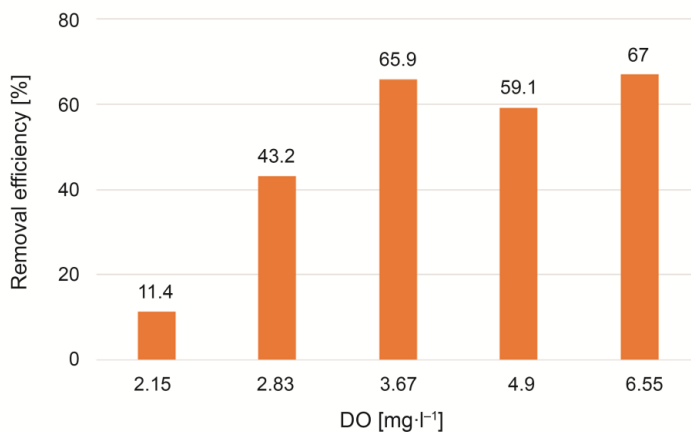


FIGURE 7. NH₃-N removal efficiency with different DO concentration

the dissolved oxygen is high so that removal efficiency increased.

As concluded above results the NH₃-N removal efficiency of 65.9% for DO 3.67 mg·l⁻¹ is near to the NH₃-N removal efficiency of 67.05% for DO 6.55 mg·l⁻¹, so that in this study will be considered DO 3.67 mg·l⁻¹ as the most suitable DO for NH₃-N removal in the operation of SBBR for hospital wastewater treatment.

TP removal at different DO concentration

As the DO concentration raised from 2.15 to 6.55 mg·l⁻¹, the effluent of TP concentration was reduced from 4.9 to 1.3 mg·l⁻¹ (Fig. 8). The effluent of TP concentration was supposed to increase with DO concentration in the early phase, besides that, no this activity was noticed. It was due to the efficiency of phosphorus absorbing is decreased during that period. It could be ob-

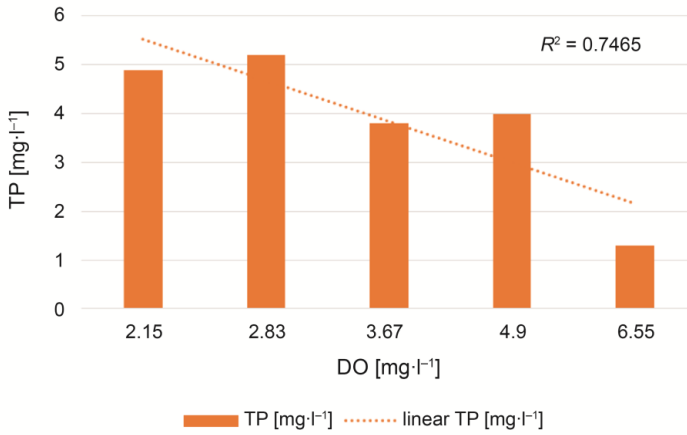


FIGURE 8. TP removal variation under different DO concentration

served that increasing the concentration of DO, as a result, there is more aerobic phosphorus absorption and thus reduces the time required for the desired aeration at the same phosphorous released content (Rong, Peng, Zhang & Fang, 2008). The concentration of DO was confirmed to be around 3.67 mg·l⁻¹ for the current study, with the aeration period to be 5 h, based on the rate of phosphorus removal, phosphorus utilization rate, aeration period, and usage of energy.

TP removal efficiency increased with rising dissolved oxygen values up to 6.55 mg·l⁻¹ within the limits of this study is 2.15–6.55 mg·l⁻¹, as shown in Figure 9. Therefore, it can be concluded that the value of DO with the removal efficiency of 79.70% is the most suitable value for total phosphorous removal in the case of SBBR to hospital wastewater treatment in this study, while the value of DO 3.67 mg·l⁻¹ is not suitable to TP removal

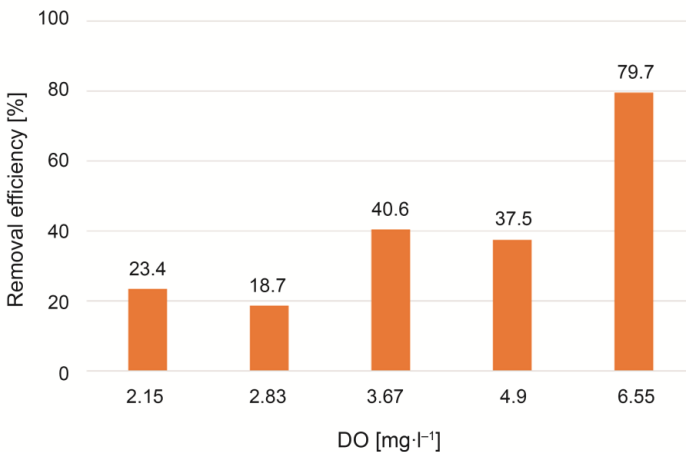


FIGURE 9. TP removal efficiency with different DO concentration

as compared with COD, NH₃-N, and TN removal efficiencies under same DO concentration.

SBBR performance as compared with global standards

The effluent quality from SBBR is compared with global standards for the discharge of treated sewage into the water body as detailed in Table 2. Values of COD, TN, and TP in the effluent of SBBR comply with all WHO, European, and Chinese standards, while ammonia satisfies just Chinese standards and outside WHO and European standards.

Conclusions

For the recent study, the reactor of SBBR is being used in the treatment of hospital wastewater. Operation of SBBR cycle mode was divided into (0.5-hour fill, 6.0-hour reaction time, 1.0-hour settle time, and 0.5-hour settles time), and the range of DO as 2.15–6.55 mg·l⁻¹. The following conclusions can be obtained from the current study's tests and results:

1. Influent wastewater of Al-Taalimi hospital in Basrah was compared to untreated domestic wastewater's typical characteristics, BOD is 280 mg·l⁻¹, COD is 550 mg·l⁻¹, TN is 55 mg·l⁻¹, and TSS is

225 mg·l⁻¹, were taken into consideration more than medium strength and less than high strength, on the contrary, raw hospital wastewater has high concentration with respect pollutants like NH₃-N is 44 mg·l⁻¹ and TDS is 2,325 mg·l⁻¹, while TP is 6.5 mg·l⁻¹ are considered to be in the median concentration value.

2. SBBR system is considered efficient in the treatment of hospital wastewater in Basrah city under different DO concentrations, for DO 3.67 mg·l⁻¹ the removal efficiencies of COD, NH₃-N, and TN, were 84.55, 65.91 and 78.18% respectively, while DO 6.55 mg·l⁻¹ given higher removal efficiency for TP 79.7%, this means that total phosphorus needs higher value for DO to get higher removal efficiency.
3. Comparison effluent values of SBBR with European, WHO, and Chinese discharge standards, it was mentioned that concentration of COD 85 mg·l⁻¹, TN 12 mg·l⁻¹, and TP 1.3 mg·l⁻¹ will meet all standards (European, WHO, and China), while NH₃-N 15 mg·l⁻¹ satisfies just China standard and outside (WHO and European) standards, SBBR's efficiency was studied in this paper, and it achieved properly as appropriate biological treatment operation for hospital wastewater treatment in Basrah city.

TABLE 2. SBBR effluent compared with effluent discharge standards

Contaminants	Effluent of SBBR [mg·l ⁻¹]	SD	Global standards of effluent wastewater [mg·l ⁻¹]		
			European (van Riesen, 2004)	WHO (WHO, 2006)	China (ZDHC, 2016)
COD	85	1.41	125	100	100
NH ₃ -N	15	2.16	10	6	15
TP	1.3	0.26	5	2	4
TN	12	2.20	20	15	25

References

- Al-Rekabi, W. S., Al-Khafaji, S. A., Hassan, A. H. & Janna, H. (2021). Effectiveness of sequencing batch biofilm reactor technology to treat domestic wastewater in Basrah City. *Journal of Ecological Engineering*, 22 (8), 234–242. <https://doi.org/10.12911/22998993/138999>
- American Public Health Association [APHA] (1998). *Standard methods for the examination of water and wastewater*. Washington: American Public Health Association.
- Dangcong, P., Bernet, N., Delgenes, J. P. & Molletta, R. (2001). Simultaneous organic carbon and nitrogen removal in an SBR controlled at low dissolved oxygen concentration. *Journal of Chemical Technology & Biotechnology: International Research in Process, Environmental & Clean Technology*, 76 (6), 553–558. <https://doi.org/10.1002/jctb.419>
- Dinçer, A. R. & Kargi, F. (2001). Salt inhibition kinetics in nitrification of synthetic saline wastewater. *Enzyme and Microbial Technology*, 28 (7–8), 661–665. [https://doi.org/10.1016/S0141-0229\(01\)00312-X](https://doi.org/10.1016/S0141-0229(01)00312-X)
- Gieseke, A., Arnz, P., Amann, R. & Schramm, A. (2002). Simultaneous P and N removal in a sequencing batch biofilm reactor: insights from reactor-and microscale investigations. *Water Research*, 36 (2), 501–509. [https://doi.org/10.1016/S0043-1354\(01\)00232-9](https://doi.org/10.1016/S0043-1354(01)00232-9)
- Jasem, Y. I., Jumaha, G. F. & Ghawi, A. H. (2018). Treatment of medical wastewater by moving bed bioreactor system. *Journal of Ecological Engineering*, 19 (3), 135–140. <https://doi.org/10.12911/22998993/86152>
- Majlesi, N. M. (2001). Study of wastewater disposal status and effluent quality in hospitals of Shahid Beheshti University of Medical Sciences. *Researcher Bulletin of Medical Sciences (Pejouhandeh)*, 6 (4), 371–376.
- Marek, K., Pawęska, K. & Bawiec, A. (2021). Treatment of Wastewater with High Ammonium Nitrogen Concentration. *Journal of Ecological Engineering*, 22 (4), 224–231. <https://doi.org/10.12911/22998993/134079>
- Metcalf & Eddy, Inc. (2003). *Wastewater engineering: treatment and reuse*. Boston: McGraw-Hill Companies.
- Miège, C., Choubert, J. M., Ribeiro, L., Eusèbe, M. & Coquery, M. (2009). Fate of pharmaceuticals and personal care products in wastewater treatment plants – conception of a database and first results. *Environmental Pollution*, 157 (5), 1721–1726. <https://doi.org/10.1016/j.envpol.2008.11.045>
- Mishra, K., Sharma, A. & Sarita, A. S., Ayub, S. (2016). A study: biomedical waste management in India. *IOSR Journal of Environment Science, Technology and Food Technology*, 10 (5), 64–67.
- Pathiraja, G., Egodawatta, P., Goonetilleke, A. & Te'o, V. S. J. (2019). Effective degradation of polychlorinated biphenyls by a facultative anaerobic bacterial consortium using alternating anaerobic aerobic treatments. *Science of the Total Environment*, 659, 507–514. <https://doi.org/10.1016/j.scitotenv.2018.12.385>
- Pochana, K., Keller, J. & Lant, P. (1999). Model development for simultaneous nitrification and denitrification. *Water Science and Technology*, 39 (1), 235–243. [https://doi.org/10.1016/S0273-1223\(98\)00789-6](https://doi.org/10.1016/S0273-1223(98)00789-6)
- Radha, K. V., Kalaivani, K. & Lavanya, R. (2009). A case study of biomedical waste management in hospitals. *Global Journal of Health Science*, 1 (1), 82–88.
- Riesen, S. van (2004). European Wastewater Standards. Presentation at the Wastewater Forum of IFAT China 2004: International Trade Fair for Environmental Protection.
- Rong, H., Peng, Y., Zhang, C. & Fang, Q. (2008). Study on effect of aeration rate on biological phosphorus removal in sequencing batch biofilm reactor. *China Water and Wastewater*, 24 (5), 72–76.
- Rittmann, B. E. (2018). Biofilms, active substrata, and me. *Water Research*, 132, 135–145. <https://doi.org/10.1016/j.watres.2017.12.043>
- Rusten, B., Eikebrokk, B., Ulgenes, Y. & Lygren, E. (2006). Design and operations of the Kaldnes moving bed biofilm reactors. *Aquacultural Engineering*, 34 (3), 322–331. <https://doi.org/10.1016/j.aquaeng.2005.04.002>
- Schaar, H., Clara, M., Gans, O. & Kreuzinger, N. (2010). Micropollutant removal during biological wastewater treatment and a subsequent ozonation step. *Environmental Pollution*, 158 (5), 1399–1404. <https://doi.org/10.1016/j.envpol.2009.12.038>
- Sharma, P., Mathur, N., Singh, A., Sogani, M., Bhatnagar, P., Atri, R. & Pareek, S. (2015).

- Monitoring hospital wastewaters for their probable genotoxicity and mutagenicity. *Environmental Monitoring and Assessment*, 187 (1), 4180. <https://doi.org/10.1007/s10661-014-4180-0>
- Timraz, K., Xiong, Y., Al Qarni, H. & Hong, P. Y. (2017). Removal of bacterial cells, antibiotic resistance genes and integrase genes by on-site hospital wastewater treatment plants: surveillance of treated hospital effluent quality. *Environmental Science: Water Research & Technology*, 3 (2), 293–303. <https://doi.org/10.1039/C6EW00322B>
- United Nations Children's Fund [UNICEF] (2019). *Multi-tiered approaches to solving the water crisis in Basra*. New York: UNICEF.
- World Health Organization [WHO] (2006). A compendium of standards for wastewater reuse in the Eastern Mediterranean Region. Geneva: World Health Organization.
- Yong, Z. J., Bashir, M. J., Ng, C. A., Sethupathi, S. & Lim, J. W. (2018). A sequential treatment of intermediate tropical landfill leachate using a sequencing batch reactor (SBR) and coagulation. *Journal of Environmental Management*, 205, 244–252. <https://doi.org/10.1016/j.jenvman.2017.09.068>
- Zero Discharge of Hazardous Chemicals [ZDHC] (2016). *Textile industry wastewater discharge quality standards: literature review*.
- Zgórska, A. & Grabińska-Sota, E. (2019). Klasyfikacja toksyczności ścieków szpitalnych w odniesieniu do kryteriów ich szkodliwości względem biocenozy wodnych [The toxicity classification of hospital wastewater in relation to the criterion of their harmfulness in reference to water biocenosis]. *Inżynieria Ekologiczna – Ecological Engineering*, 20 (4), 5–13. <https://doi.org/10.12912/23920629/112650>
- Zorita, S., Mårtensson, L. & Mathiasson, L. (2009). Occurrence and removal of pharmaceuticals in a municipal sewage treatment system in the south of Sweden. *Science of the Total Environment*, 407 (8), 2760–2770. <https://doi.org/10.1016/j.scitotenv.2008.12.030>
- Zupanc, M., Kosjek, T., Petkovšek, M., Dular, M., Kompare, B., Širok, B., Blažeka, Ž. & Heath, E. (2013). Removal of pharmaceuticals from wastewater by biological processes, hydrodynamic cavitation and UV treatment. *Ultrasonics Sonochemistry*, 20 (4), 1104–1112. <https://doi.org/10.1016/j.ultsonch.2012.12.003>

Summary

Impact of dissolved oxygen on hospital wastewater quality treated by SBBR in Basrah city, Iraq. The hospitals close to the residences can make problems for the environment as a consequence of sewage drained into the water stream. Sequencing batch biofilm reactor (SBBR) offers advantages for treating sewage; such as simple operation, flexible process, and cost-effective. The laboratory bench-scale experiments were carried out treating hospital wastewater (HWW) of one of Basrah hospital city by a fabricated SBBR reactor of 26 l working volume. The hospital wastewater has the following characteristics (average values): pH 7.3, BOD equal to $280 \text{ mg} \cdot \text{l}^{-1}$, COD equal to $550 \text{ mg} \cdot \text{l}^{-1}$, total phosphorus (TP) equal to $6.4 \text{ mg} \cdot \text{l}^{-1}$, ammonia ($\text{NH}_3\text{-N}$) equal to $44 \text{ mg} \cdot \text{l}^{-1}$ and total suspended solid (TSS) equal to $272 \text{ mg} \cdot \text{l}^{-1}$. This research aims to estimate the performance of the SBBR system for treating hospital wastewater to enhance different effluent parameters such as COD, total nitrogen (TN), ammonia, and total phosphorous (TP) with various dissolved oxygen (DO) with range of $2.15\text{--}6.55 \text{ mg} \cdot \text{l}^{-1}$, the best DO values give these removal efficiencies for COD equal to 84.55%, $\text{NH}_3\text{-N}$ equal to 65.91% and TN between 78 and 18% for DO equal to $3.67 \text{ mg} \cdot \text{l}^{-1}$, while TP removal efficiency was 79.70% for DO equal to $6.55 \text{ mg} \cdot \text{l}^{-1}$. By comparison of the SBBR effluent with international standards for effluent sewage, it noticed COD concentration $85 \text{ mg} \cdot \text{l}^{-1}$, TN $12 \text{ mg} \cdot \text{l}^{-1}$ and TP $1.3 \text{ mg} \cdot \text{l}^{-1}$ met all standards (European, WHO, and China), while $\text{NH}_3\text{-N}$ $15 \text{ mg} \cdot \text{l}^{-1}$ was outside WHO and European standards, while satisfies only Chinese standard.

Lada STEJSKALOVÁ ✉  <https://orcid.org/0000-0003-2271-7574>

Libor ANSORGE  <https://orcid.org/0000-0003-3963-8290>

Jiří KUČERA  <https://orcid.org/0000-0002-7540-4750>

Elżbieta ČEJKA  <https://orcid.org/0000-0001-8154-7005>

T.G. Masaryk Water Research Institute, p.r.i., Czech Republic

ROLE OF WASTEWATER TREATMENT PLANTS IN POLLUTION REDUCTION – EVALUATED BY GREY WATER FOOTPRINT INDICATOR

Key words: grey water footprint, Odra river basin, pollution, wastewater treatment plant, water footprint assessment

Introduction

The wastewater collection and treatment systems are increasingly centralized. The objective of the Council Directive 91/271/EEC concerning urban wastewater treatment is to protect the environment from the adverse effects of urban wastewater discharges. In December 2019, the European Commission published the Evaluation of the Urban Wastewater Treatment Directive where evaluated whether the existing rules have reached their objectives and whether they still serve their purpose (Pistocchi et al., 2019). The assessment confirms that the Directive has proved

very effective overall when fully implemented. The reduction of organic matter and other pollution in treated wastewater has improved water quality throughout the European Union. Though implementing the Directive has been expensive, benefits clearly outweigh the costs.

In this study, we focused on the evaluation of a 15-year period of intensive construction of new and intensification and modernization of existing wastewater treatment plants. For the evaluation, the grey water footprint (GWF) methodology was used. The water footprint assessment (WFA) was introduced in 2002 (Hoekstra & Hung, 2003) and methodology was standardized by the Water Footprint Network (WFN) (Hoekstra, Chapagain, Aldaya & Mekonnen, 2012). The grey water footprint is defined as the volume of freshwater required to assimilate the load

of pollutants; based on natural background concentrations and existing ambient water quality standards.

The GWF studies are often focused on agriculture, energy sector, industry, organizations, regions or states, river basins, households, etc. The application of the grey water footprint methodology on wastewater treatment plants has so far been limited to a few studies: Shao and Chen (2013), Gu et al. (2016), Morera, Corominas, Poch, Aldaya and Comas (2016), Gómez-Llanos, Durán-Barroso and Matías-Sánchez (2018), Ansorge, Stejskalová, Dlabal and Kučera (2019), Johnson and Mehrvar (2019), Yapicioğlu (2019), Ansorge, Stejskalová, Dlabal and Čejka (2020), Gómez-Llanos, Matías-Sánchez and Durán-Barroso (2020), Stejskalová, Ansorge, Kučera and Vološinová (2021).

This work assesses the pollution discharged from 251 wastewater treatment plants throughout the Odra river basin in the Czech Republic. The development of pollution produced in municipalities and discharged from WWTPs over the period of 15 years (2004–2018) has been analyzed, from a point of view of basic chemical pollution parameters reduction.

This work is an extension of the publication (Ansorge et al., 2020) monitoring the impact of municipal wastewater treatment plants on the reduction of pollutants in the Czech part of the international Odra basin.

Methods

Grey water footprint (GWF)

Grey water footprint is a part of the water footprint introduced in 2002 (Hoekstra & Hung, 2003) and points to the level of pollution. It is defined as the volume of freshwa-

ter required to assimilate a load of pollutants to the level of existing ambient water quality standards. The GWF calculation was made in accordance with the “Water Footprint Assessment Manual” (Hoekstra et al., 2012). The calculation is carried out in three steps: for each pollutant (i) and discharge point (j), the $GWF_{j,i}$ is calculated according to Equation (1). The pollutant with the highest value of the GWF at the point of j then indicates the GWF at j (Eq. 2). The GWF of a system under assessment is the sum of the GWFs of all pollutant emission points into the aquatic environment (Eq. 3).

$$GWF_{j,i} = \frac{L_{j,i}}{C_{\max,j,i} - C_{\text{nat},j,i}} \quad (1)$$

$$GWF_j = \max\{GWF_{j,1}, GWF_{j,2}, \dots, GWF_{j,i}\} \quad (2)$$

$$GWF = \sum_{j=1}^n GWF_j \quad (3)$$

where:

$GWF_{j,i}$ – GWF of the pollutant i released into water at the point j [volume unit per time unit],

GWF_j – GWF of pollutant at the point j [volume unit per time unit],

GWF – GWF of the subject [volume unit per time unit],

$L_{j,i}$ – quantity of the pollutant i being emitted into water at the point j [weight unit per time unit],

$C_{\max,j,i}$ – maximum permissible concentration of the substance i in receiving water at the point j [weight unit per volume unit],

$C_{\text{nat},j,i}$ – natural concentration of the substance i in receiving water at the point j [weight unit per volume unit],

n – number of discharge points.

Site description – Odra river basin

Two large European rivers have their springs in the central part of Europe, in the Czech Republic – Elbe and Odra. The analysis was carried out for the Odra river basin in the Czech Republic (Fig. 1). A share of the Odra river on the total run-off from the Czech Republic is 9.8% and its district occupies about 7% of the total territory of the Czech Republic, with the area of 7,217 km².

Data sources

For the purpose of this study, data on all WWTPs listed in the Water balance database (ces. *vodní balance*) were analyzed. The principles of operation and data collection of the Water balance are regulated by the Decree of the Ministry of Agriculture 431/2001 (Vyhláška Ministerstva zemědělství 431/2001 Sb.). It is a national register of withdrawals and discharges. It orders all subjects discharging wastewater into surface or groundwater in quantities exceeding annu-

ally 6,000 m³ or monthly 500 m³ to forward data on the water quantity and quality. In the Czech part of the Odra river basin, a total of 3,056 records concerning 251 wastewater treatment plants are registered for the period from 2004 to 2018.

According to the outflow volume and incoming organic pollution, the WWTPs were divided into seven size categories, which reflect the most common size division of wastewater treatment plants according to EU and Czech regulations and standards (the annual amount of treated wastewater is given in brackets):

- Category I for less than 50 PE (< 2,000 m³),
- Category II for 51–200 PE (2,001–8,000 m³),
- Category III for 201–500 PE (8,001–20,000 m³),
- Category IV for 501–2,000 PE (20,001–80,000 m³),
- Category V for 2,001–10,000 PE (80,001–400,000),



FIGURE 1. Odra river basin district in the middle-north Europe (the area of interest is highlighted by hatch pattern; coordinates 49°95' N, 18°33' E)

- Category VI for 10,001–100,000 PE (400,001–4,000,000 m³),
- Category VII for more than 100,000 PE (> 4,000,000 m³).

When evaluating the GWF, special attention must be paid to the selection/setting of the use of concentration limits, as these strongly affect the GWF value (Liu, Antonelli, Liu & Yang, 2017; Miglietta et al., 2017). Maximum acceptable concentrations (C_{max}) of a pollutant in a receiving watercourse are set by the Czech Technical Standard ČSN 75 7221 determining classification of surface water quality (Class II – Moderate polluted water) (Mičaník, Hanslík, Němejcová & Baudišová, 2017). Surface water quality according to Class II is described as being affected by human activities, but water quality indicators still reach values that allow for the existence of a rich, balanced and sustainable ecosystem. Natural concentration values (C_{nat}) are given by the same standard (Class I – Unpolluted water). The difference between the values of maximum acceptable concentration (C_{max}) and natural concentration (C_{nat}) is described as the assimilation capacity of the flow (Jamshidi, 2019). A list

of monitored parameters with their natural and maximum concentration values is given in Table 1.

Results and discussion

Pollution produced

Over the course of 15 years, the number of WWTPs in the Czech part of the Odra river basin increased by 38% (from 164 to 227 facilities) and the GWF of inflowing pollution to WWTPs increased in total by 33%. Progression in the amount of pollution supplied and treated at WWTPs as well as the increasing number of WWTPs in a given period are shown in Figure 2.

If we relate the development of the produced pollution of individual pollutants to the beginning of the monitoring, we find that suspended solids show a permanent slight decrease in the order of percent units. The decline in suspended solids could be related to the drought of recent years. The phosphorus pollution produced remains more or less at the same level (phosphate detergents have been replaced by others, which could cause

TABLE 1. Monitored parameters with their natural and maximum concentration values

Parameter	Symbol	Unit	C_{nat}	C_{max}	Assimilation capacity ($C_{max} - C_{nat}$)
Biochemical oxygen demand	BOD ₅	mg·l ⁻¹	2	4	2
Chemical oxygen demand	COD	mg·l ⁻¹	15	25	10
Suspended solids	SS	mg·l ⁻¹	15	25	10
Dissolved inorganic solids*	DIS	mg·l ⁻¹	300	450	150
Inorganic nitrogen	N _{inorg}	mg·l ⁻¹	2.75	5.55	2.8
Total phosphorus	P _{tot}	mg·l ⁻¹	0.05	0.15	0.1
Ammonium nitrogen	N-NH ₄ ⁺	mg·l ⁻¹	0.2	0.4	0.2

*There are no values in the regulations set for the DIS assimilation capacity. It was derived based on the assumption that DIS are a subset of total dissolved solids (TDS). The DIS assimilation capacity was determined on the level of 1% assimilation capacity of TDS (Ansoerge et al., 2019) according to the ČSN 75 7221 (Česká agentura pro standardizaci [ČAS], 1998).

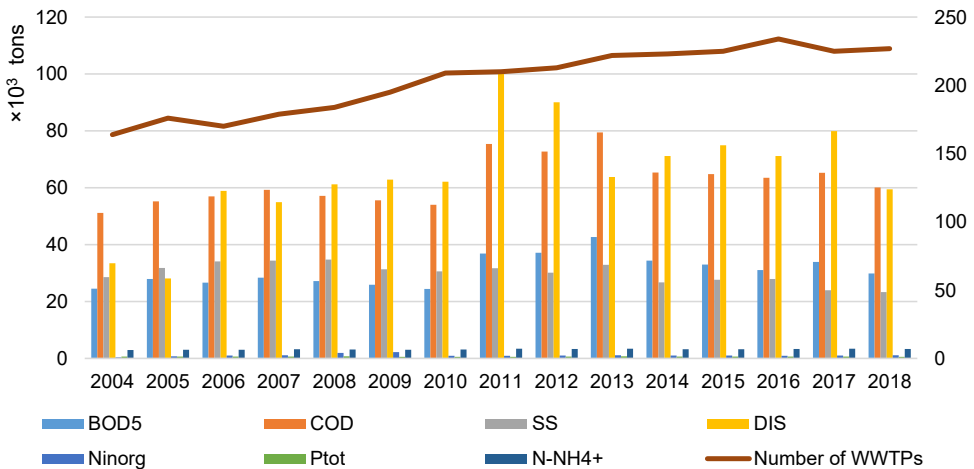


FIGURE 2. Development of the amount of pollution treated at the WWTPs in individual monitored parameters (Y-axis) and the increasing number of WWTPs (secondary Y-axis) in the monitored area (source: the Water balance database)

phosphorus stagnation). The initial increase and subsequent decrease of organic pollution (expressed in BOD₅ and COD) at inflows to WWTPs may be caused by the originally growing popularity of kitchen waste disposers, which have fallen into disfavor in recent years and are clearly not recommended. The amount of DIS pollution shows doubled values (compared to 2004) and the amount of produced inorganic nitrogen pollution tripled.

Pollution discharged and the GWF reduction

More efficient methods of wastewater treatment are making a reduction in GWF more significant. While the average reduction of GWF at WWTPs in 2004 was 86%, after 15 years it was 93% (in 2018). The value of the GWF reduction has more or less stabilized over the last eight years especially in the size categories over 20,000 m³ per year (Fig. 3).

While the total GWF at the WWTPs inflows was $3.06 \cdot 10^{11}$ m³, the total GWF at the WWTPs effluents was $2.6 \cdot 10^{10}$ m³, detailed in Table 2. Also the increasing efficiency of the GWF reduction at WWTPs is significant (Fig. 3).

While the GWF of incoming pollution is caused predominantly by ammonium nitrogen (³/₄ of cases), after passing through the WWTP, the GWF of the discharged pollution is caused, in addition to ammonium nitrogen, mainly by the discharged phosphorus.

Parameters causing the GWF

Comparison between inflows and outflows from a point of view which parameter causes pollution the most is given in Figure 4. This has not been investigated in former studies which calculate GWF reduction at WWTPs. In the studied area, the GWFs at inflows were often determined by different parameter than the GWFs at outflows

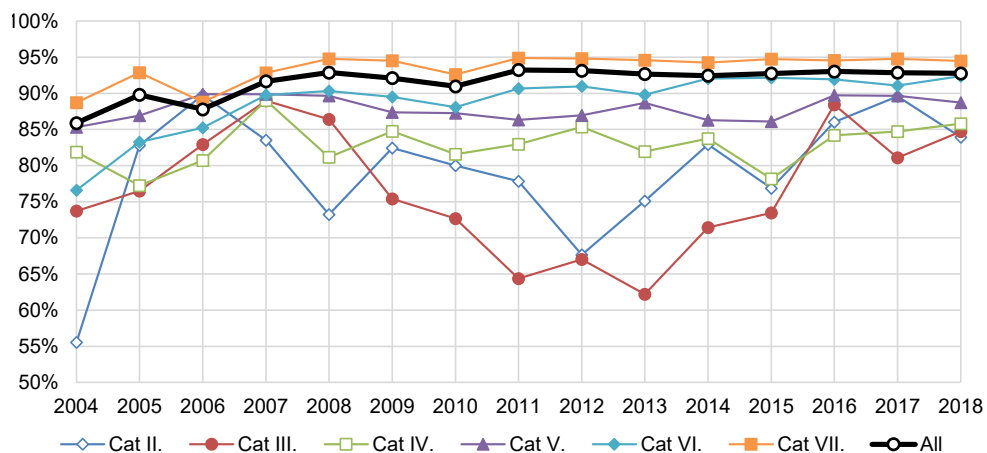


FIGURE 3. The GWF reduction at monitored WWTPs

TABLE 2. Comparison of the GWF at inflows and outflows from WWTPs

Year	GWF at the WWTP		GWF reduction by passing through the WWTP size category						
	inflows	outflows	all	Cat. II	Cat. III	Cat. IV	Cat. V	Cat. VI	Cat. VII
	×10 ⁶ m ³		%						
2004	16 089	2 301	86	56	74	82	85	77	89
2005	18 177	1 866	90	83	76	77	87	83	93
2006	17 670	2 173	88	90	83	81	90	85	89
2007	18 684	1 581	92	84	89	89	90	90	93
2008	19 052	1 384	93	73	86	81	90	90	95
2009	17 439	1 406	92	82	75	85	87	90	94
2010	17 219	1 585	91	80	73	82	87	88	93
2011	24 104	1 650	93	78	64	83	86	91	95
2012	23 981	1 663	93	68	67	85	87	91	95
2013	27 236	2 072	92	75	62	82	89	90	95
2014	18 251	1 439	92	83	71	84	86	92	94
2015	21 641	1 637	92	77	73	78	86	92	95
2016	21 608	1 586	93	86	88	84	90	92	95
2017	23 429	1 758	92	90	81	85	90	91	95
2018	21 337	1 555	93	84	85	86	89	92	94
	total		AVG						
	305 918	25 655	91.4	79	78	83	88	90	94

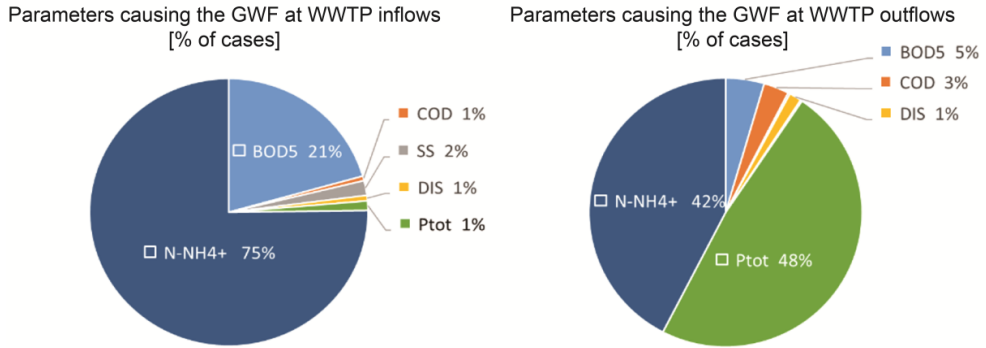


FIGURE 4. Proportional overview of pollutants which causes the GWF (comparison between inflows and outflows of WWTPs)

TABLE 3. Parameters causing the GWF at inflows and outflows, overviewed according to WWTP size categories

WWTP size category	BOD ₅		COD		SS		DIS		N _{inorg}		P _{tot}		N-NH ₄ ⁺	
	inflow	outflow	inflow	outflow	inflow	outflow	inflow	outflow	inflow	outflow	inflow	outflow	inflow	outflow
	% of cases													
Cat. II	43	23	2	8	0	1	2	2	0	0	1	23	54	43
Cat. III	17	5	1	3	0	0	0	0	0	0	2	33	81	59
Cat. IV	18	4	1	3	1	0	0	0	0	0	2	46	79	47
Cat. V	18	2	0	3	1	0	0	1	0	0	1	65	80	30
Cat. VI	19	2	0	3	3	1	3	3	0	0	1	49	74	42
Cat. VII	30	0	0	1	13	0	1	11	0	0	1	57	55	31

(Table 3). When considering the size categories, the overview is provided in Table 3.

Effect of a WWTP size category on the GWF

Wastewater treatment plants, which belong to the two largest size categories (> 10,000 PE and > 100,000 PE), account for 82% of the total GWF value of discharged pollution. The share of medium-sized WWTPs (2,001–10,000 PE) is 10%

and the share of GWF pollution discharged from all WWTPs smaller than 2,000 PE is only 8% (Table 4).

In the case of the smallest and small WWTPs, the GWF of the discharged pollution is almost always caused by ammonium nitrogen (Tables 3 and 5). Small WWTPs generally must deal with less stable nitrification (some older small WWTPs are not equipped for the process of nitrification at all) – this results in higher GWF caused by ammonium nitrogen at their effluents.

TABLE 4. Contribution of particular WWTP size categories on the total GWF of discharged pollution

WWTP size category	Annual amount of treated wastewater	Number of records in the Water balance	Contribution to GWF of total discharged pollution [%]
Cat. I	< 50 PE	3	0
Cat. II	51–200 PE	127	0
Cat. III	201–500 PE	312	2
Cat. IV	501–2 000 PE	674	6
Cat. V	2 001–10 000 PE	575	10
Cat. VI	10 001–100 000 PE	343	38
Cat. VII	> 100 000 PE	114	44

In addition, small WWTPs are often not operated very professionally and emission standards for ammonium nitrogen are set up for WWTPs from the capacity of 2,000 PE, so the operators do not have to focus on the ammonium nitrogen removal.

As the size of the WWTP enlarges, the share of the effluent GWF caused by total phosphorus increases. For the WWTPs size category IV (i.e. of projected capacity for 501–2,000 PE), the GWF of discharged pollution is almost equally caused either by ammonium nitrogen (47%) or by total phosphorus (46%). For WWTPs of 2,000 PE and larger, the effluent GWF is most often determined by total phosphorus (Tables 3 and 5).

The effect of the WWTP size category on total GWF reduction is given in Table 5. The average value of GWF reduction for all categories, was 91.4%.

The GWF of the WWTPs inflows is most often caused by ammonium nitrogen. This is due to the composition of municipal wastewater and the prevailing reduction conditions in the sewer.

In terms of effluents from WWTPs, the greatest burden for watercourses under the WWTPs is pollution caused by ammonium

nitrogen and total phosphorus (among basic chemical parameters).

The level of discharged nitrogen is important for two reasons – eutrophication and the ammonium nitrogen toxicity to fish (the dissociated form of NH_4^+ , which predominates at lower pH, is relatively harmless to fish; however the undissociated NH_3 causes acute poisoning of fish at very low concentrations, $\leq 0.1 \text{ mg}\cdot\text{l}^{-1}$). On the other hand, ammonium nitrogen is not stable in surface water and after discharge, it undergoes the nitrification relatively quickly – so the negative effect on water quality is rather local.

Both essential nutrients – nitrogen and phosphorus – contribute significantly to water eutrophication. In conditions of the Czech Republic, the nitrogen supply from point sources of pollution is prevailed by nitrogen load from agriculture and other diffuse pollution sources although action plan to reduce nitrogen load from agriculture exists (Hrabánková, 2016, 2018). Conversely, phosphorus load discharged from the point sources of pollution prevails the diffuse pollution sources.

High calculated GWF values of ammonium nitrogen and total phosphorus are inter alia caused due to these parameters have the

TABLE 5. General overview – total values of the GWF at inflows and outflows during the reported period; parameters that predominantly determine the GWF at inflows and outflows; and the percentage of GWF reduction at particular WWTPs size categories

WWTP size category	GWF at the WWTPs inflows [$\times 10^6 \text{ m}^3$]	Parameter predominantly causing the GWF at inflows	GWF at the WWTPs outflows [$\times 10^6 \text{ m}^3$]	Parameter predominantly causing the GWF at outflows	GWF reduction by WWTPs [%]	Change of indicator causing the GWF at inflows vs. outflows* [% of cases]
Cat. I	1.3	N-NH ₄ ⁺	0.3	N-NH ₄ ⁺	74	0
Cat. II	198	N-NH ₄ ⁺	41	N-NH ₄ ⁺	79	39
Cat. III	1 361	N-NH ₄ ⁺	306	N-NH ₄ ⁺	78	41
Cat. IV	8 269	N-NH ₄ ⁺	1 389	N-NH ₄ ⁺ /P _{tot}	83	57
Cat. V	22 132	N-NH ₄ ⁺	2 637	P _{tot}	88	73
Cat. VI	79 311	N-NH ₄ ⁺	8 272	P _{tot}	90	61
Cat. VII	194 021	N-NH ₄ ⁺	12 389	P _{tot}	94	87

*The percentage of cases when the GWF of inflow is caused by a different parameter than the GWF of outflow.

lowest determined water assimilation capacity; the difference between the maximum concentration in the receiving water body and the determined natural (background) concentration are only 0.1 mg·l⁻¹ for P_{tot}, and 0.2 mg·l⁻¹ for N-NH₄⁺.

Conclusions

The substantial contribution of this study is the long-term data interpretation using a tool of grey water footprint. The grey water footprint is defined as the volume of freshwater required to assimilate the load of pollutants.

The study deals with the grey water footprint of municipal pollution in the Odra river basin on the Czech Republic territory. Over the course of 15 years, the number of WWTPs increased in the analyzed area by 38%, i.e. from 164 to 227 facilities. The grey water footprint of pollution drained from municipalities by sewers to WWTPs increased

by 33%, mainly due to the construction of new WWTPs.

The reconstructions and introduction of more efficient techniques and advanced technologies into the process of wastewater treatment have made the GWF reduction very significant. While in 2004 the average GWF reduction by passage through the WWTP was 86% (total GWF at WWTPs inflows and outflows were 16·10⁹ and 2.3·10⁹ m³ respectively); in 2018, the average GWF reduction at municipal WWTPs was 93% (total GWF at WWTPs inflows and outflows were 21·10⁹ and 1.55·10⁹ m³ respectively).

The efficiency of the smallest WWTP size categories in GWF reduction is less and during the analyzed period risen up from 56 to 84%. As the wastewater treatment plant's capacity increases, the percentage of GWF reduction rises up. The GWF reduction at largest WWTPs was 89% in 2004 and in average 94% in 2018.

The GWF of pollution at inflows to the WWTPs is predominantly caused by

ammonium nitrogen and secondarily also by BOD₅. The GWF of pollution at the WWTPs discharges is most often caused by total phosphorus (it occurs mainly at effluents from larger and large WWTPs) and ammonium nitrogen (mainly at effluents from small WWTPs). In 5% of cases, the GWF of discharged pollution is caused by BOD₅.

When evaluating the GWF, special attention must be paid to the concentration limits, as these strongly affect the final GWF value.

The pollution evaluation via the GWF methodology can offer a suitable complement to the traditional quantification of absolute values of the amount of pollution.

Acknowledgements

The study was supported by the institutional resources for the long-term development of the T. G. Masaryk Water Research Institute, public research institution, Prague, Czech Republic (Project 3600.52.02/2021).

References

- Ansorge, L., Stejskalová, L., Dlabal, J. & Čejka, E. (2020). Wpływ oczyszczalni ścieków na redukcję zanieczyszczeń odprowadzanych w czeskiej części dorzecza Odry [Effect of wastewater treatment plants to the reduction of pollution discharged in the Czech part of the Odra river]. *Scientific Review Engineering and Environmental Sciences*, 29 (2), 123–135. <https://doi.org/10.22630/PNIKS.2020.29.2.11>
- Ansorge, L., Stejskalová, L., Dlabal, J. & Kučera, J. (2019). Šedá vodní stopa jako ukazatel udržitelného vypouštění odpadních vod – případová studie Povodí Ohře [Grey water footprint as an indicator of sustainable wastewater discharge – Ohře River Basin case study]. *Entechno*, 2 (2), 12–18. <https://doi.org/10.35933/ENTECHO.2019.12.001>
- Council Directive 91/271/EEC of 21 May 1991 concerning urban waste-water treatment. OJ L 135, 30.05.1991.
- Česká agentura pro standardizaci [ČAS] (1998). *Jakost vod – Klasifikace jakosti povrchových vod* (ČSN 75 7221). Praha: Česká agentura pro standardizaci.
- Gómez-Llanos, E., Duran-Barroso, P. & Matías-Sánchez, A. (2018). Management effectiveness assessment in wastewater treatment plants through a new water footprint indicator. *Journal of Cleaner Production*, 198, 463–471. <https://doi.org/10.1016/j.jclepro.2018.07.062>
- Gómez-Llanos, E., Matías-Sánchez, A. & Durán-Barroso, P. (2020). Wastewater treatment plant assessment by quantifying the carbon and water footprint. *Water*, 12 (11), 3204. <https://doi.org/10.3390/w12113204>
- Gu, Y., Dong, Y. N., Wang, H., Keller, A., Xu, J., Chiramba, T. & Li, F. (2016). Quantification of the water, energy and carbon footprints of wastewater treatment plants in China considering a water–energy nexus perspective. *Ecological Indicators*, 60, 402–409. <https://doi.org/10.1016/j.ecolind.2015.07.012>
- Hoekstra, A. Y., Chapagain, A. K., Aldaya, M. M. & Mekonnen, M. M. (2012). *The water footprint assessment manual: setting the global standard*. London: Earthscan.
- Hoekstra, A. Y. & Hung, P. Q. (2003). Virtual water trade: A quantification of virtual water flows between nations in relation to international crop trade. In A. Y. Hoekstra (Ed.), *Virtual water trade. Proceedings of the International Expert Meeting on Virtual Water Trade* (pp. 25–47). Delft: IHE Delft.
- Hrabánková, A. (2016). Ochrana vod před dusičnany ze zemědělství [Water protection against nitrates from agriculture]. *Vodohospodářské technicko-ekonomické informace*, 58 (5), 34–39.
- Hrabánková, A. (2018). Zjišťování účinnosti akčního programu podle nitrátové směrnice 91/676/EHS v době klimatické změny [Determining of effectiveness of the action program according to the nitrate directive in a period of climate change]. *Vodohospodářské technicko-ekonomické informace*, 60 (5), 30–33. <https://doi.org/10.46555/VTEI.2018.07.004>

- Jamshidi, S. (2019). An approach to develop grey water footprint accounting. *Ecological Indicators*, 106, 105477. <https://doi.org/10.1016/j.ecolind.2019.105477>
- Johnson, M. B. & Mehrvar, M. (2019). An assessment of the grey water footprint of winery wastewater in the Niagara Region of Ontario, Canada. *Journal of Cleaner Production*, 214, 623–632. <https://doi.org/10.1016/j.jclepro.2018.12.311>
- Liu, W., Antonelli, M., Liu, X. & Yang, H. (2017). Towards improvement of grey water footprint assessment: with an illustration for global maize cultivation. *Journal of Cleaner Production*, 147, 1–9. <https://doi.org/10.1016/j.jclepro.2017.01.072>
- Mičaník, T., Hanslík, E., Němejcová, D. & Baudišová, D. (2017). Klasifikace kvality povrchových vod [Classification of surface water quality]. *Vodohospodářské technicko-ekonomické informace*, 59 (6), 4–11.
- Miglietta, P. P., Toma, P., Fanizzi, F. P., De Donno, A., Coluccia, B., Migoni, D., Bagnardo, F. & Serio, F. (2017). A grey water footprint assessment of groundwater chemical pollution: case study in Salento (southern Italy). *Sustainability*, 9 (5), 799. <https://doi.org/10.3390/su9050799>
- Morera, S., Corominas, L., Poch, M., Aldaya, M. M. & Comas, J. (2016). Water footprint assessment in wastewater treatment plants. *Journal of Cleaner Production*, 112, 4741–4748. <https://doi.org/10.1016/j.jclepro.2015.05.102>
- Pistocchi, A., Dorati, C., Grizzetti, B., Udias, A., Vigiak, O. & Zanni, M. (2019). *Water quality in Europe: effects of the Urban Wastewater Treatment Directive. A retrospective and scenario analysis of Dir. 91/271/EEC*. Luxembourg: Publications Office. <https://doi.org/10.2760/303163>
- Shao, L. & Chen, G. Q. (2013). Water footprint assessment for wastewater treatment: method, indicator, and application. *Environmental Science & Technology*, 47 (14), 7787–7794. <https://doi.org/10.1021/es402013t>
- Stejskalová, L., Ansorge, L., Kučera, J. & Vološinová, D. (2021). Grey water footprint as a tool for wastewater treatment plant assessment – Hostovice case study. *Urban Water Journal*, 18 (10), 796–805. <https://doi.org/10.1080/1573062X.2021.1941134>
- Vyhlaška Ministerstva zemědělství ze dne 3. prosince 2001 o obsahu vodní bilance, způsobu jejího sestavení a o údajích pro vodní bilanci. 431/2001 Sb.
- Yapicioğlu, P. (2019). Seasonal water footprint assessment for a paint industry wastewater treatment plant. *Sakarya Üniversitesi Fen Bilimleri Enstitüsü Dergisi*, 23 (2), 175–183. <https://doi.org/10.16984/saufenbilder.411137>

Summary

Role of wastewater treatment plants in pollution reduction – evaluated by grey water footprint indicator. The study assesses the pollution discharged from 251 wastewater treatment plants (WWTPs) throughout the Odra river basin in the Czech Republic. The development of pollution production over a period of 15 years (2004–2018) together with a number of WWTPs in the Odra river basin were analyzed. The grey water footprint (GWF) of discharged pollution was determined both in terms of individual size categories of WWTPs and in terms of the parameter that most affects the level of pollution. The share of the small WWTPs size categories (up to 2,000 PE) on the total GWF value of discharged pollution is only 8%, although these are the most numerous. The share of the WWTPs of the size category > 10,000 PE on the total GWF value of discharged pollution is 82%. Total phosphorus (at large WWTPs) and ammonium nitrogen (at small WWTPs) were identified as the key pollutants that most determine the value of the grey water footprint of discharged pollution.

Jana KORYTÁROVÁ  <https://orcid.org/0000-0002-0046-0141>

Tomáš HANÁK   <https://orcid.org/0000-0002-7820-6848>

Brno University of Technology, Faculty of Civil Engineering, Czech Republic

ANALYSIS OF ROAD CONSTRUCTION PROJECTS PRICE CHANGES IN THE SELECTED PHASES OF THEIR LIFE-CYCLE

Key words: road construction project, LCC, estimated value, contract price, actual price

Introduction

Road construction projects belong to the most costly public procurement activities worldwide. It is, therefore, crucial to manage these projects appropriately from the cost point of view from the early stages of the project through the construction phase and operation phase until demolition. Public authorities tend to apply the life-cycle cost (LCC) approach more frequently recently, however, in practice, there is a lack of data and experience in order to predict future costs precisely. Accurate estimation of the LCC is essential as it contributes to the informed decisions about the selection of the optimal project alternative from the long-term per-

spective. The underestimation of costs may lead to inefficient allocation of resources and it is also considered as major source of risk in project appraisal (Odeck, Welde & Volden, 2015). Makovšek, Tominc and Logožar (2012) even speak about systematic cost overruns in transport infrastructure projects that lead to distorted cost-benefit analysis, where LCC is on the side of cost, while benefits represent items such as savings in travel time or reduction in accidents (Korytářová & Papežiková, 2015).

Unfortunately, road construction projects are extremely complex and difficult to manage, and therefore frequently facing misinformation about the costs. This often results in high-cost overruns which may also affect the quality of works, service life and overall viability of the project itself. According to Kennedy, Pantelias, Makovšek, Grewe and Sindall (2018), the uncertainty in cost esti-

mation evolves over the project life-cycle and arises from the difficulties in estimating construction, maintenance, operation and financing costs.

One of the serious problems are discrepancies between planned costs (estimated in the early stages of the project) and actual realized costs (after the completion of the works) (Peško et al., 2017). Chong and Hopkins (2016) claim that the variability between planned and actual costs may cause the reduced scope of works (the project is not implemented in the full range), cancellations and non-fulfilment of expected rates of return.

According to Tijanić, Car-Pušić and Šperac (2020), the discrepancies between planned and actual costs stem from the lack of data and information in the conceptual phase of the project. The incompleteness of the data makes the cost estimation difficult and burdened by uncertainty. As a result, errors in the project are usually transformed into price adjustments and the extended duration of the construction phase (Pilger, Machado, de Assis Lawisch-Rodriquez, Zappe, Rodriquez-Lopez, 2020).

The spectrum of cost overrun causes is wide due to the complexity of road construction projects. Numerous researchers (e.g.: Cantarelli, Flybjerg, Molin & van Wee, 2010; Adel, Elyamany, Belal & Kotb, 2016) reported four categories of cost overruns origin: technical (e.g. inadequate data), economic (e.g. deliberate underestimation due to lack of resources), psychological (e.g. tendency to underestimate time, costs and risks) and political (cost underestimation to increase the probability of project acceptance). From the economic point of view, it is also important to take into account the prices of raw materials as road construction projects are of a long-term perspective.

These prices are affected by future economic development and, therefore, may be difficult to predict (Loulizi, Bichiou & Rakha, 2019). The LCC of real projects can also be affected by the contract type. It has been shown on the example of national roads in Indonesia that the use of performance-based contracts has the potential to create lower LCC compared to traditional approaches (as performance-based contracts are lowered by preventive interventions that may delay and limit road structure deterioration, i.e. reduce long-term costs (Susanti, Wirahadikusumah, Soemardi & Sutrisno, 2019). For this purpose, it is important to identify maintenance and repair works for a particular structure as well as their average repetition. For instance, Bhaskaran, Palaniswamy and Rengaswamy (2006) listed normally occurring repair works for a concrete road bridge (sealing of cracks, repairing spalled portion, worn coating, joints expansion and concrete railing). The resulting bid price is affected also by other influencing factors, such as competition of many bidders in the tender process (Hanák & Muchová, 2015) or by the use of electronic reverse auctions (Hanák & Serfat, 2018). On the other hand, the accuracy of the estimation of the planned costs might be affected by an estimator itself. As Odeck et al. (2015) claim, estimates by experts who are contracted as external consultants are more accurate compared to the estimates made by contracting authorities themselves. Therefore, it is important to cooperate with experienced stakeholders as their experience achieved from previous projects may help to prevent possible errors (Tijanić et al., 2020). According to Pilger et al. (2020), many errors result from geological, geotechnical and soil quality studies.

The application of control mechanisms, advanced methods and tools to manage the

costs of road construction projects is highly needed since the great magnitude of cost overruns is evident. Researchers applied various approaches to improve cost estimation, e.g. neural networks were applied for early cost estimation of road tunnel construction (Petroutsatou, Georgopoulos, Lambropoulos & Pantouvakis, 2012). Their models enable decision-makers to compare design alternatives from a cost perspective which supports the creation of viable financial plans. Tijić et al. (2020) proposed general regression neural network model of early cost estimate of road construction projects with the MAPE (mean absolute percentage error) of 13.06% providing better results than multilayer perceptron, radial basis function neural network and linear regression.

Peško et al. (2017) compared neural networks and support vector machine for the purpose of urban road construction cost and duration estimation. The best support vector machine model achieved higher precision with the MAPE of 7.06% when compared to neural networks. Wang, Yu and Chan (2012) compared the success of different models for predicting construction costs between logistic regression, artificial neural networks (ANN), more specifically single ANNs, bootstrap aggregating ANNs and adaptive boosting ANNs, and support vector machine. They have shown on the sample of 92 projects that the best overall prediction accuracy was achieved by a support vector machine. Furthermore, different models can be combined to create hybrid models, as applied by Petrusheva, Car-Pušić and Zileska-Pancovska (2019). Their support vector machine-based hybrid model achieved accuracy with the MAPE of 1.01% and correlation coefficient between actual and planned values of 0.998.

The available body of literature confirms the need for advanced LCC management of

road construction projects. Although the researchers use different quantitative as well as qualitative approaches to tackle how the LCC prediction can be improved, there is a lack of data based on a detailed analysis of contractual documentation between the contracting authorities and contractors. This paper, therefore, aims to address this specific issue by examining the documentation of the sample of regional road construction projects in the South Moravian Region (Czech Republic). In particular, the presented study seeks to reveal and discuss the causes of cost overruns that are contained in contractual documentation. The study focuses on selected phases of the building object life-cycle, more specifically procurement and construction phases.

The content of this paper is structured as follows. The following section presents materials and methods employed to achieve the aim of this paper. The third section presents and discusses results of the analysis and the final section summarises general conclusions, states research limitations and outline future research directions.

Material and methods

This study effectively combines qualitative and quantitative research methods to address the researched topic. First of all, the set of contractual documentation for road construction projects in the studied area (South Moravian Region) has been collected from available public sources. In addition, the research sample contains two road bridge projects in the urban area, which seamlessly connect to the city's road networks. This involves data from contracts for works and supplementary documentation such as the investor's website where information about basic project characteristics can be obtained

as well as data from the Journal of Public Procurement (ces. *Věstník veřejných zakázek*). All analysed projects are by the same contracting authority. Regarding the procurement procedure, contractors were selected on the basis of the lowest bid price under the open procedure. All projects belong to the category of below-threshold and above-threshold contracts according to the Czech Public Procurement Act (*Zákon 134/2016 Sb.*), i.e. **small-scale contracts are not included** in the dataset.

In total, data on 41 projects were collected. Each project has been characterised by numerical data and by data describing the causes of cost overruns. The project was included in the dataset under the condition that all necessary documents and variables are provided and that the execution of construction works has been completed. This has resulted in a reduced final dataset of 16 projects. Such a large reduction of the dataset points to the fact that despite the obliga-

tion to make all these data publicly available, in the reality, a significant part of the data is missing.

Dataset of road construction projects

Each project has been characterized by a set of variables that were taken from collected documentation. This involves the estimated value (*EV*) of the project set before the public procurement procedure has started, contract price (*CP*) that has been negotiated between the contracting authority and winning supplier in the contract for work, actual price (*AP*) representing the resulting price from the contract when all the amendments and changes to the project are taken into account. It follows that only completed projects were considered and analysed. Furthermore, the number of tenderers (*NoT*) and the number of amendments (*NoA*) subsequently agreed to the contract are also provided for each project (Table 1).

TABLE 1. Basic description of the dataset

ID	Project	<i>EV</i> [EUR]	<i>CP</i> [EUR]	<i>AP</i> [EUR]	<i>NoT</i>	<i>NoA</i>
1	II/379 Tišnov – Drásov	2 756 242	2 278 646	2 329 758	4	2
2	II/413 Dobelice – Hostěradice	1 549 609	929 688	1 007 877	6	2
3	II/373, III/37367 Březina transit	2 763 594	1 732 422	1 841 804	12	3
4	III/49918 Hrubá Vrbka transit	1 792 373	1,239 839	1 248 275	8	3
5	II/431 Kojátky relocation	2 265 670	1 660 155	1 784 674	3	2
6	II/408 Hrádek transit	2 381 967	1 845 055	1 836 386	6	3
7	II/432 Kyjov – Milotice – Ratiškovice	2 110 664	1 126 126	1 083 382	10	2
8	II/408 Krhovice transit	1 321 836	945 341	958 565	5	2
9	II/421 Terezín – Velké Pavlovice	4 426 793	3 426 768	3 501 449	4	3
10	II/602 Brno Jihlavská, bridge	1 236 680	734 346	753 952	6	2
11	II/152 Jamolice transit	2 561 016	1 791 016	1 918 373	14	6
12	II/602 Ostrovačice transit, 2 nd construction	847 305	605 437	681 151	11	1
13	II/430 Tučapy – Vyškov (non-urban area)	2 843 453	2 296 057	2 388 838	9	2
14	II/380 Moutnice transit	2 740 586	1 898 170	1 933 059	8	6
15	II/422 Podivín – Lednice	3 066 406	2 295 987	2 390 955	6	4
16	III/15289 Brno Evropská, bridge	3 945 313	3 108 418	3 145 540	8	3

Tenders' data processing

The following variables were defined in order to reveal the magnitude of the relative differences between *EV*, *CP* and *AP*:

$$CP_{EV} = \frac{CP - EV}{EV} 100\%$$

where *CP_{EV}* stands for the ratio between the contract price and the estimated value. This variable indicates whether the resulting price from the public tender is lower or higher when compared to the estimated value.

The next variable *AP_{CP}* (actual price – contract price ratio) shows how the price for the contract changed since signing the contract for work until the completion of works and invoicing. *AP_{CP}* is defined by the following equation:

$$AP_{CP} = \frac{AP - CP}{CP} 100\%$$

Finally, the *AP_{EV}* ratio is calculated in order to find out whether the actual price tends to get closer to the estimated value when compared to the tender price as

a consequence of negotiation of contractual amendments with extra works, price adjustments etc.

$$AP_{EV} = \frac{AP - EV}{EV} 100\%$$

Finally, the tender documentation was analysed from the qualitative point of view in order to reveal potential causes of project value/price relative differences. In particular, contract for works and all related amendments were considered from this perspective.

Results and discussion

Quantitative evaluation

A comparison of construction costs in individual project phases (stated in prices without VAT) is shown in Figure 1. The three variables analysed (*CP*, *EV*, *AP*) show the difference between the contract price and the estimated value, the actual price and the contract price, the actual price and the estimated value.

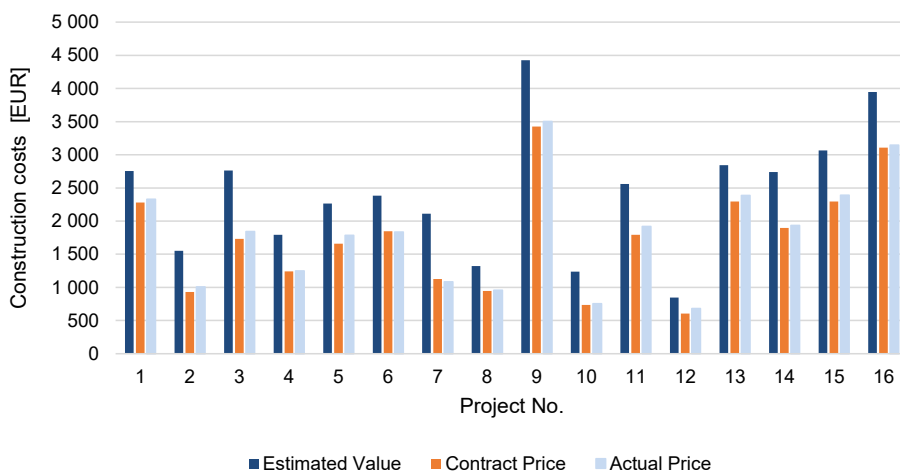


FIGURE 1. Comparison of construction costs in individual project phases

Data in Figure 1 and Table 2 clearly show significant differences between the estimated value and contract price. The mean value for the CP_EV variable is -29.25% and the median value is -28.51% indicating that contract price is considerably lower if compared to the estimated value. Such difference can be attributed to two potential causes: (1) the estimated value was not set correctly, in other words, it is overestimated and (2) the competition between individual suppliers on the market is pushing the market price down. On the other hand, when regarding the AP_CP values, it is clear that projects tend to increase the actual value of the works carried out compared to the price resulting from the works contract.

TABLE 2. Basic statistics of the dataset

Variable	Min	Max	Mean	Median
	%			
CP_EV	-17.33	-46.65	-29.25	-28.51
AP_CP	-3.80	12.51	3.62	2.46
AP_EV	-15.47	-48.67	-26.68	-24.00

It is clear from the market analysis which includes the bid prices of the contractors in each tender, that the bid prices of each unique contract have a relatively wide range. Table 3 shows the contract price (CP in Column b) of each public tender and the maximum relative difference of contract price from the bid price of the most advantageous bid which was assessed on the basis of the lowest tender price criterion (Column c) and the relative difference between the contract price and the expected value (Column d).

It is clear from the comparison of the relative differences in Table 3 Columns c and d that the maximum bid price for Projects 6, 7, 8, 11, 13, 15 and 16 is close to the estimated value of the project, in other cases the estimated value is always higher.

TABLE 3. Market analysis of individual tenders

ID	CP [EUR]	Max relative difference of bid price from CP [%]	Relative difference of EV from CP
a	b	c	d
1	2 279	12.38	17.33
2	930	10.09	40.01
3	1 732	52.82	37.31
4	1 240	18.14	30.83
5	1 660	15.10	26.73
6	1 845	20.13	22.54
7	1 126	45.60	46.65
8	945	23.74	28.48
9	3 427	8.74	22.59
10	734	64.59	40.62
11	1 791	36.71	30.07
12	605	39.93	28.55
13	2 296	21.40	19.25
14	1 898	10.04	30.74
15	2 296	19.41	25.12
16	3 108	19.41	21.21

It is possible to identify projects where CP may be considered to be of an exceptionally low bid price nature by looking at Figure 1. In particular, Projects 2, 7 and 10 show a CP_EV value lower than -40% , which means that their CP has fallen by more than 40% compared to the EV . Given the fact that the decrease in bid prices is dependent on the number of bids submitted in the tender (Hanák & Muchová), it was further investigated whether there is any relationship existing between NoT and CP_EV . The R^2 value of a logarithmic trend line is 0.1213 indicating that there is no strong relationship between examined variables (Fig. 2a). Therefore, it cannot be statistically claimed that a higher number of tenderers cause a higher difference between EV and CP .

Analysis of the AP_CP variable reveals how the actual price paid by the contracting

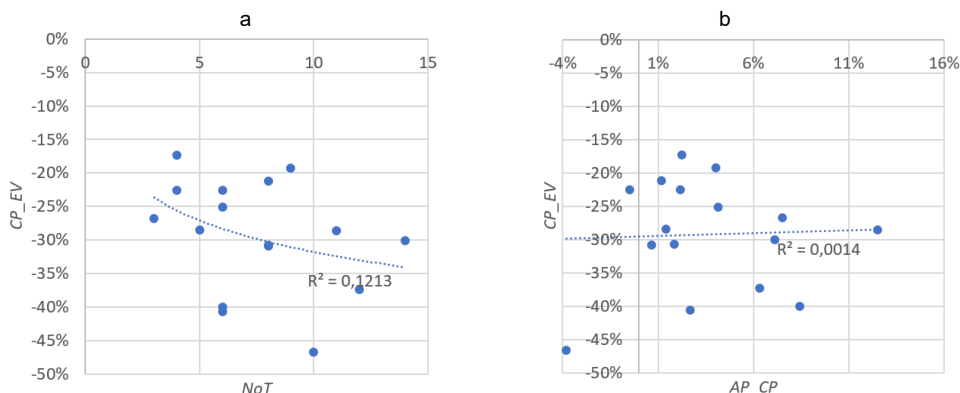


FIGURE 2. Relation between NoT and CP_EV (a), and CP_EV and AP_CP (b)

authority after the competition of the project has changed when compared to the contract price. Both the mean and the median values are close to 0% (3.62 and 2.46% respectively). Accordingly, it can be stated that generally, award prices and contract prices values do not differ much from each other. Nevertheless, if minimum and maximum values are considered (−3.80 and 12.51%), it is clear that for individual projects there can be significant changes made to the budget. It might be of interest to check whether the higher value of AP_CP is connected to the lower value of CP_EV . In particular, this idea leads to the potential application of the bidding strategy of submitting lower (CP) bids in the tender procedure followed with the expectation of AP increase e.g. as a result of extra works, i.e. unbalanced bidding (Nyström & Mandell, 2019).

Data in Figure 2b clearly shows that there is no relation between the examined variables CP_EV and AP_CP . For example, for Project 4 (that is the project with the $CP_EV = -30.83\%$), CP is almost equal to AP ($AP_CP = 0.68\%$), thus there was no change to the project price during its implementation. In contrast, Project 12 with a similar value of CP_EV ($CP_EV = -28.55\%$) reaches

$AP_CP = 12.51\%$. From this, we can conclude that variations between CP and AP depend not just on extra works, but also on cancelled work and other types of amendments that can be caused by various causes.

Finally, when taking into consideration the results of CP_EV and AP_CP analysis, it is not surprising that AP_EV values are close to the CP_EV values. Of course, several relative differences can be observed, e.g. for Project 12 for which $CP_EV = -28.55\%$ and $AP_CP = -19.61\%$. Results of the above-stated analyses indicate the need for qualitative analysis, which may help to reveal the causes of differences between CP and AP . In particular, such analysis needs a detailed study of project contractual documentation related to its real implementation.

Analysis of contractual documentation for project implementation

In order to understand the causes of variations between CP and AP , an in-depth study of contractual documentation has been conducted for all 16 analysed projects. In particular, attention has been paid to the contracts for work and all related amendments that were negotiated in connection with modifi-

cations to the project during its implementation phase. Table 1 provides the number of amendments for each project. Data suggests that negotiation on amendments belongs to the common practice for road construction projects. The number of amendments varies from 1 to 6 for a particular contract.

When all the contracts for work with amendments were collected, the causes of project modifications were sought. It has been revealed that modifications mostly relate to the changes in the scope and extent of the project (i.e. extra work and cancelled work).

The actual causes of changes in construction costs, the difference between the contract price and the final price of individual

TABLE 4. The frequency of main causes of changes in construction costs of projects under research during their implementation

Cause of change	Project number
C1: Completion to/change in technical design	1, 16
C2: Increase in asphalt layers and milling area	2, 8
C3: No need for implementation documentation and geometric plans	2
C4: Unbearable subsoil/ /replacement of base layer	3, 9, 11, 13, 14, 15
C5: Replacement of unsuitable material	4, 5, 6, 13, 14, 16
C6: Conflicts with existing utilities	6, 9, 11, 12
C7: Demolition of unknown structure	6, 11, 12
C8: Change in rock classification	11
C9: Emergency condition of the culvert Culvert disrepair	12
C10: Requests from other organisations (police, technical building management)	10, 13
C11: Reinforcement of diversion routes	14
C12: Another acreage	7

projects recorded in the amendments to the contracts between the contracting authority and the construction contractor are summarized in Table 4.

In total, causes were grouped into 12 categories, where unbearable subsoil/replacement of underlayer and replacement of unsuitable material were the most frequent. This is mainly due to inadequate structural testing during the construction phase and refinement of the survey plan according to reality, i.e. change of the scope of work project/reality. Due to the fact that these projects are carried out in built-up areas, unplanned conflicts with existing utilities and current requirements of administrations, e.g. public lighting or requirements for the addition of traffic signs, also appear to be a more frequent cause.

Conclusions

It is clear from the overall project analysis that there is a relatively high level of interest from contractors in public works contracts for regional road construction, which is evident from the number of contractors who tendered for the contracts under research (3 to 14 tenders) in the sample studied. The market has therefore significantly reduced the construction costs in the first phase compared to the expected value. Another issue is the difference between the contract price and the final price, which in all cases has increased due to various implementation reasons, among which, in the project area, the survey and design work – unbearable subsoil leading to the replacement of the proposed underlayer, changes in material properties, conflicts with existing utilities or the need to demolish unknown structures during the project. The relative differences between the

contract price and the final price can be considered satisfactory (the mean 3.62% and the median 2.46% based on an interval between –3.8 and 12.51%).

Information and knowledge about the cost progress in the implementation phase should lead to the refinement of the expected value in particular, which is a very important aspect of investment activities, as it is one of the basic items of information on how many financial resources will be needed for the implementation of the project, what type of tender needs to be launched and whether the investor is able to finance the project from his own or other available sources (especially EU subsidies). From the managerial perspective, the findings presented in this paper aim to help construction professionals, among others, by identifying the most common causes of negotiating contractual amendments for road construction projects.

It was unfortunately not possible to proceed to a more detailed analysis that would allow, for example, to study the detailed financial impact of the specific identified causes on the construction project due to the extent of the documentation and the structure of the data available. Following research could therefore provide further interesting findings in this respect, which have the potential to help investors to prepare projects in a way that would further minimise the need to adjust the scope/method of works and negotiate contractual amendments.

Acknowledgements

This paper has been worked out under the project of the specific research at the Brno University of Technology FAST-S-21-7472 – Management of Economic Processes in Construction Engineering.

References

- Adel, K., Elyamany, A., Belal, A. M. & Kotb, A. S. (2016). Developing parametric model for conceptual cost estimate of highway projects. *International Journal of Engineering Science*, 6 (7), 1728–1734.
- Bhaskaran, R., Palaniswamy, N. & Rengaswamy, N. S. (2006). Life-cycle cost analysis of a concrete road bridge across open sea. *Materials Performance*, 45 (10), 51–55.
- Cantarelli, C. C., Flyvbjerg, B., Molin, E. J. & Wee, B. van (2010). Cost overruns in large-scale transportation infrastructure projects: explanations and their theoretical embeddedness. *European Journal of Transport and Infrastructure Research*, 10 (1). <https://doi.org/10.18757/ejtr.2010.10.1.2864>
- Chong, U. & Hopkins, O. (2016). An international experience on the evolution of road costs during the project life cycle. *Transport Policy*, 48, 60–66. <https://doi.org/10.1016/j.tranpol.2016.02.010>
- Hanák, T. & Muchová, P. (2015). Impact of competition on prices in public sector procurement. *Procedia Computer Science*, 64, 729–735. <https://doi.org/10.1016/j.procs.2015.08.601>
- Hanák, T. & Serrat, C. (2018). Analysis of construction auctions data in Slovak public procurement. *Advances in Civil Engineering*, 2018, 1–13. <https://doi.org/10.1155/2018/9036340>
- Kennedy, J., Pantelias, A., Makovšek, D., Grewe, K. & Sindall, J. (2018). *Risk pricing in infrastructure delivery: making procurement less costly*. Paris: International Transport Forum. Retrieved from: https://www.itf-oecd.org/sites/default/files/docs/risk-pricing-in-infrastructure-delivery_1.pdf
- Korytářová, J. & Papežíková, P. (2015). Assessment of large-scale projects based on CBA. *Procedia Computer Science*, 64, 736–743.
- Loulizi, A., Bichiou, Y. & Rakha, H. (2019). Use of life cycle cost analysis and multiple criteria decision aid tools for designing road vertical profiles. *Sustainability*, 11 (24), 7127. <https://doi.org/10.3390/su11247127>
- Makovšek, D., Tominc, P. & Logožar, K. (2012). A cost performance analysis of transport infrastructure construction in Slovenia. *Transportation*, 39 (1), 197–214. <https://doi.org/10.1007/s11116-011-9319-z>

- Nyström, J. & Mandell, S. (2019). Skew to win, not to profit – unbalanced bidding among informed bidders. *Journal of Public Procurement*, 19 (1), 46–54. <https://doi.org/10.1108/JOPP-03-2019-024>
- Odeck, J., Welde, M. & Volden, G. H. (2015). The impact of external quality assurance of costs estimates on cost overruns: empirical evidence from the norwegian road sector. *European Journal of Transport and Infrastructure Research*, 15 (3), 286–303. <https://doi.org/10.18757/ejtir.2015.15.3.3079>
- Peško, I., Mučenski, V., Šešljija, M., Radović, N., Vujkov, A., Bibić, D. & Krklješ, M. (2017). Estimation of costs and durations of construction of urban roads using ANN and SVM. *Complexity*, 2017, 2450370. <https://doi.org/10.1155/2017/2450370>
- Petroutsatou, K., Georgopoulos, E., Lambropoulos, S., & Pantouvakis, J. P. (2012). Early cost estimating of road tunnel construction using neural networks. *Journal of Construction Engineering and Management*, 138 (6), 679–687. [https://doi.org/10.1061/\(asce\)co.1943-7862.0000479](https://doi.org/10.1061/(asce)co.1943-7862.0000479)
- Petrusheva, S., Car-Pušić, D. & Zileska-Pancovska, V. (2019). Support vector machine based hybrid model for prediction of road structures construction costs. *IOP Conference Series: Earth and Environmental Science*, 222 (1), 012010. <https://doi.org/10.1088/1755-1315/222/1/012010>
- Pilger, J. D., Machado, E. L., Assis Lawisch-Rodriguez, A. de, Zappe, A. L. & Rodriguez-Lopez, D. A. (2020). Environmental impacts and cost overrun derived from adjustments of a road construction project setting. *Journal of Cleaner Production*, 256, 120731. <https://doi.org/10.1016/j.jclepro.2020.120731>
- Susanti, B., Wirahadikusumah, R. D., Soemardi, B. W. & Sutrisno, M. (2019). Life cycle cost analysis of a PBC pilot projector for road in Indonesia. *IIUM Engineering Journal*, 20 (2), 57–69. <https://doi.org/10.31436/iiumej.v20i2.1075>
- Tijanić, K., Car-Pušić, D. & Šperac, M. (2020). Cost estimation in road construction using artificial neural network. *Neural Computing and Applications*, 32 (13), 9343–9355. <https://doi.org/10.1007/s00521-019-04443-y>
- Wang, Y. R., Yu, C. Y. & Chan, H. H. (2012). Predicting construction cost and schedule success using artificial neural networks ensemble and support vector machines classification models. *International Journal of Project Management*, 30 (4), 470–478. <https://doi.org/10.1016/j.ijproman.2011.09.002>
- Zákon ze dne 19. dubna 2016 o zadávání veřejných zakázek. 134/2016 Sb.

Summary

Analysis of road construction projects price changes in the selected phases of their life-cycle. This paper deals with an analysis of causes that lead to the change in price (value of construction costs) of road infrastructure projects in selected phases of the building structure life-cycle, more specifically procurement and construction phases, with the aim to refine the price estimation in the estimated value determination phase. The sample of regional road construction projects in the South Moravian Region (Czech Republic) documentation forms the basis for the research. The methodological procedure is aimed at monitoring changes in the value of construction costs during the preparation and implementation phase of the construction. Estimated values, contract prices and actual prices of individual projects are compared to determine them and the reasons for their differences are discussed. The changes (decrease) in the values of construction costs determined by estimated value and contract price show the strong influence of the construction market and the interest of construction companies in the implementation of public works contracts in the field of road infrastructure projects. The relative differences range up to 47%. The changes (increase) in construction costs determined by contract price and actual price are much lower, up to 13%, and result from specific situations during the implementation of the construction, for which subsoil bearing capacity problems and material changes were determined as the most significant.

Mimoza DUSHI  <https://orcid.org/0000-0002-1853-6829>

Albert BERILA   <https://orcid.org/0000-0003-0754-269X>

University of Prishtina, Faculty of Mathematics and Natural Sciences, Kosovo

DETERMINING THE INFLUENCE OF POPULATION DENSITY ON THE LAND SURFACE TEMPERATURE BASED ON REMOTE SENSING DATA AND GIS TECHNIQUES: APPLICATION TO PRIZREN, KOSOVO

Key words: population density, *LST*, *SUHI*, GIS, remote sensing, Prizren

Introduction

Population (demographic pressure), in the process of urbanization, influences different types of natural land cover to be destroyed and changed/replaced with impervious materials very common in urban areas, such as concrete, asphalt, stone, metal, glass, and other materials which have low albedo values and which absorb heat, causing the released energy to increase (Buyantuyev & Wu, 2009; Harlan & Ruddell, 2011; Santamouris, Synnefa & Karlessi, 2011). All of these developments cannot escape at all without radical changes. Such changes affect the reduction of the amount of oxygen produced by the natural soil cover; reduction in evaporation; increase

of surface flow (urban runoff); absorption, storage, and increase of heat; deterioration of air quality; deterioration of water quality, etc. (Berila & Dushi, 2021).

The process of urbanization has undergone a great and rapid development due to the high growth of the population. Such processes, which directly affect people, are of great importance. Therefore, such and similar processes lead to only one possible path: positive development (Morefield, Fann, Grambsch, Raich & Weaver, 2018; Berila & Isufi, 2021a). Developments which in themselves have rapid rates and large changes, the effects, of course, will not be satisfactory. Such processes, during development, produce effects that are harmful. These effects consist of: increase of surfaces with impervious materials; reduction/destruction/damage of green areas; reduction/destruction/damage of natural surfaces; empowerment of materials

with low albedo values – increase of temperature, etc. All these effects that we mention, to a large extent, are encountered in cities.

Based on the information discussed in the paragraphs above it is more than understandable and logical that if we were to make a comparison between cities and rural areas in terms of heat, we would clearly see that the temperatures will be higher in the former. It is precisely such effects and processes that have led to the emergence in these areas of a very harmful phenomenon with a host of negative effects – urban heat island (UHI) – a phenomenon in which higher temperatures are encountered in urban areas compared to peripheral or rural areas (Wang, Zhang, Tsou & Li, 2017). It is very important to note that the UHI phenomenon can appear in all areas in which natural surface changes are made with artificial ones and in those cases when the earth is left completely bare, regardless of whether it is in urban, peripheral, or rural area (Ursu, 2019). The increase of human activities in the cities will make the UHI phenomenon even stronger. This phenomenon, with all its negative effects, will seriously endanger the human population (especially those living in cities) (Mohajerani, Bakaric & Jeffrey-Bailey, 2017; Peres, Lucena, Rotunno Filho & de Almeida França, 2018). It is crucial that the municipalities, or other governmental authorities, emphasize the dangerousness of the UHI phenomenon, while proposing solutions (as much as possible).

The UHI phenomenon has three types – depending on how the temperature is measured (Fabrizi, Bonafoni & Biondi, 2010; Sherafati, Saradjian & Rabbani, 2018; Berila & Isufi, 2021b; Isufi, Berila & Bulliqi, 2021):

a) Canopy layer heat island (CLHI) – this layer lies approximately at the average height of buildings and is determined by

measuring the air temperature at a height of 2 m above the ground. The CLHI has usually been measured using sensors mounted on fixed meteorological stations (Nichol, Fung, Lam & Wong, 2009; Clay et al., 2016; Berila & Isufi, 2021b; Isufi et al., 2021).

- b) Boundary layer heat island (BLHI) – lies above the CLHI layer and can reach a thickness of up to 1 km. It is measured using special platforms, such as radiosondes and aircraft (Berila & Isufi, 2021b; Isufi et al., 2021).
- c) Surface urban heat island (SUHI) – difference in radiant temperature between urban and non-urban surfaces. The measurement/determination of this layer is done using thermal remote sensors (Berila & Isufi, 2021b; Isufi et al., 2021).

Science has made significant progress in how the UHI phenomenon can be measured. In regard to the method used by researchers, which entirely depends on the data the researchers has, the tools they retains, and the accuracy required. In cases when in the study area there are different restrictions on measuring the UHI phenomenon, such as the lack of equipment/instruments for measuring temperature and their inhomogeneous distribution (as in our case of the study area), then it is necessary to use GIS and remote sensing techniques (Berila & Dushi, 2021). Using them to measure the UHI phenomenon represents SUHI, which is determined using geospatial technology through the calculation of the land surface temperature (Voogt & Oke, 2003; Despini et al., 2016; Pour & Voženilek, 2020).

During the hot season(s) and the day, SUHI values get higher and vice versa (Roth, Oke & Emery, 1989; Yuan & Bauer, 2007). The UHI phenomena have a lot of seasonal variation and the temperature values meas-

ured with remote sensing techniques will also depend on the materials from which the buildings are built, the orientation and density of the buildings, etc. Consequently, a UHI can also appear in a sparsely populated area due to building construction materials and related activities.

The Republic of Kosovo has not yet been able to escape/avoid such changes and all the negative effects they bring. Due to the high density/activities of the population, the caused changes, and the surfaces with impervious materials, in the second largest city of Kosovo—Prizren, have caused quite noticeable challenges to appear, which require very careful and quick solutions.

The main goal of our work is to make a connection between the atmosphere and the land surface temperature in order to reach the identification of all areas that are affected

and face the SUHI phenomenon; to map the summer SUHI for the entire Municipality of Prizren in order to see whether the cadastral zones with the highest population density (greater emphasis of human activities) are the ones that face the most with this phenomenon. Our other goal is to help the city leaders identify the areas that are attacked and endangered by the SUHI phenomenon so that they can take immediate action to mitigate this phenomenon in order that the population of those areas can live as healthy as possible.

Study area

Prizren is the second largest city in the Republic of Kosovo after Prishtina. The coordinates of Prizren are $42^{\circ}00'$ and $42^{\circ}20'$ N and $20^{\circ}30'$ and $21^{\circ}00'$ E (Fig. 1). It is a town

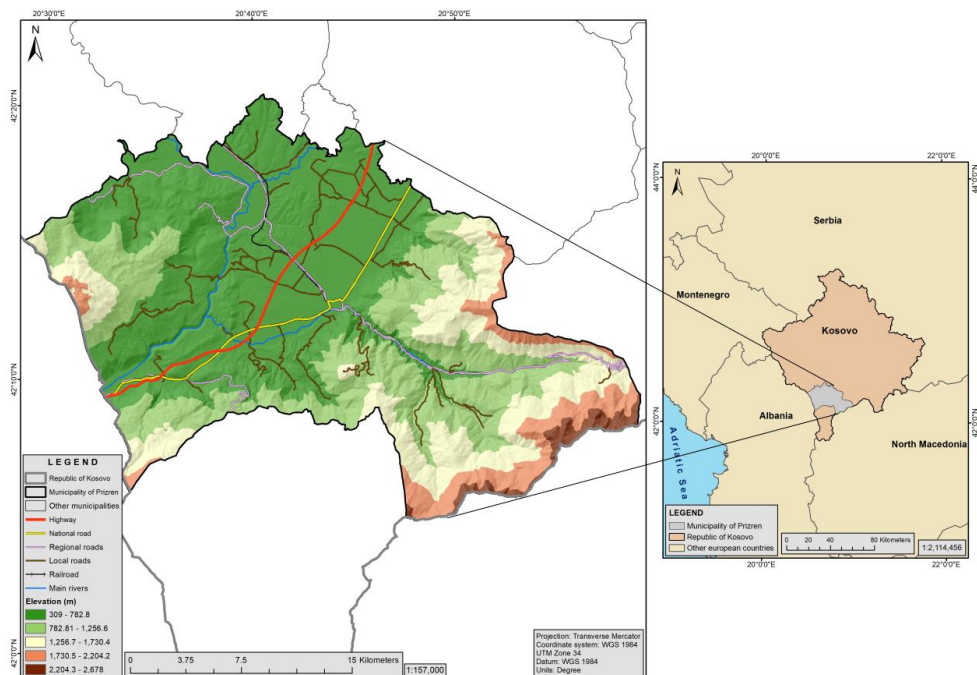


FIGURE 1. Location of the study area

located on the slope of Sharri Mountain and along the Lumbardhi (Bistrica) river. The climate of Prizren has continental characteristics with a slight influence of the Mediterranean climate at lower altitudes, while in the mountains the harsh alpine climate dominates (UN-HABITAT, 2012). These climatic characteristics and mountain terrain are the reasons for the rich natural resources that contribute to the economic development of the country and the region (Universiteti Teknik i Stambollit, Urban Design Studio, Plan&Art [UTS, UDS & Plan&Art], 2012).

We have compiled Figures 2 and 3 to have a clearer picture of the distribution of settlements in the city of Prizren, as well as to highlight and distinguish areas urbanized from areas with vegetation. Figure 2 presents CORINE land cover (CLC) of our study area

of 2018 downloaded at the European Environment Agency (EEA). The main extension and predominance belong to the forest vegetation – at the edges of the southern, eastern, and western part. In the central and northern part, the area is occupied by activities of the population. Settlements are distributed in the Prizren area quite densely compared to the mountainous parts where we see a lower density of settlements. An uncontrolled and unplanned expansion is observed especially towards the main arterial roads. In particular the increase along the northwestern part poses a risk to agricultural land where there is irrigation infrastructure, which means bypassing the great potential for agricultural production. Misuse of agricultural land for construction has caused the degradation of natural resources and unsustainable develop-

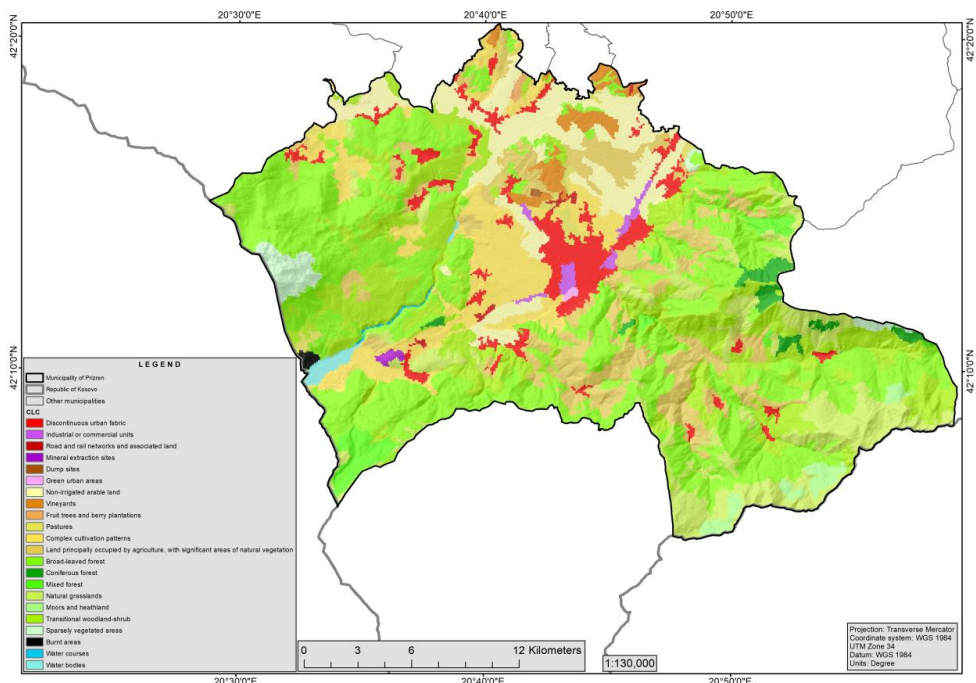


FIGURE 2. CORINE land cover of the study area

ment. A large part of the agricultural land has been lost because of illegal gravel and quarry mining activities. The land is constantly being occupied with stone mining facilities which in turn causes the formation of informal settlements on the surrounding agricultural lands (UTS, UDS & Plan&Art, 2012).

Figure 3 presents a false-color composition of the optical satellite image of Landsat 8 – composition 7 6 4 (R: SWIR 2, G: SWIR 1, B: Red). Based on presented data, it is noticed that the built-up area lies mainly in the north, in the west, and in the central parts. Such an extension has been determined by the topography of this area. Most of the settlements are concentrated in the city center. The expansion of settlements continues along the north and the main road arteries that run through Prizren.

Data and methods

There are various methods for determining the surface heat of a given area. In our study, we determined the surface heat of the city of Prizren by calculating *LST* through GIS and remote sensing using satellite image of Landsat 8. This paper used the satellite image of Landsat 8 on 8 August 2021. This satellite image had a negligible percentage of cloud cover (0.01%) and we used the United States Geological Survey (USGS) website (<https://earthexplorer.usgs.gov>) to download it (Table 1). Our satellite image has been downloaded from Collection 1 and at a Level 1.

For the compilation of all maps in this study we used the program ArcGIS 10.5. In Figure 4 we have made a schematic presentation of the whole methodology that we

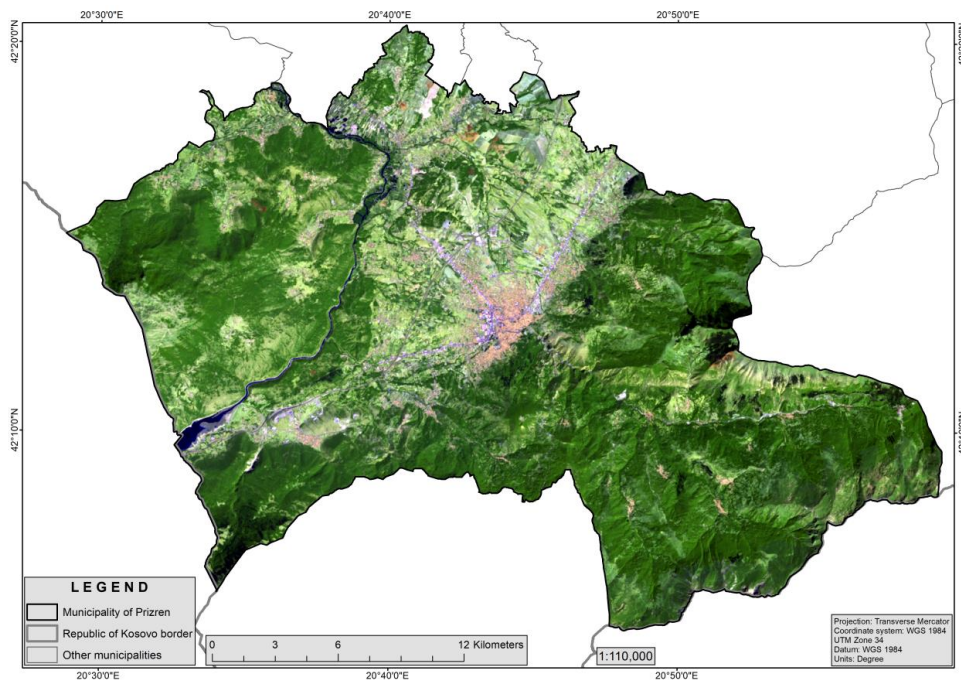


FIGURE 3. A false-color composition of optical satellite image of our study area (R: SWIR 2, G: SWIR 1, B: Red)

TABLE 1. Characteristics of the satellite image used in this study

Sensor type	Date	Path/Row	Cloud cover	Spatial resolution	Format	Source
Landsat 8 OLI/TIRS	08.08.2021	185/31	0.01%	30 m	tiff	https://earthexplorer.usgs.gov

have used in this paper. In this figure, we have presented in a general way all the steps we have taken to come to the mapping of the SUHI phenomenon and to determine the impact of population density on it. Whereas in the following sections, this article presents a detailed calculation for each part, in order to have better understanding of the methodology being used.

In Landsat 8 sensor satellite images, thermal data is stored in the form of digital numbers (DN) (Berila & Isufi, 2021a). These numbers represent cells (pixels) that have not yet been calibrated into units (Käfer et al., 2020) that make sense (meaningful units). An important step to be taken is the return to radiance of DNs (Isaya Ndossi & Avdan, 2016).

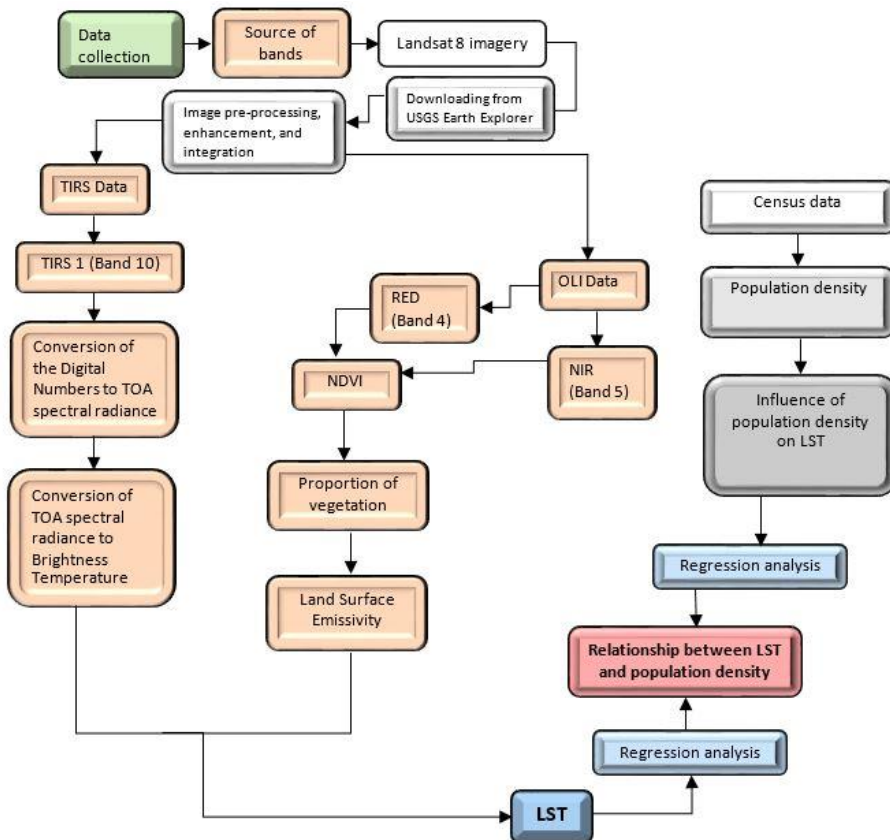


FIGURE 4. Flowchart depicting methodology

The following equation was used to convert DNs of Band 10 (TIRS 1) to spectral radiance (United States Geological Survey [USGS], 2019) in the Landsat 8 TIRS sensor (Isaya Ndossi & Avdan, 2016; Salih, Jasim, Hassoon & Abdalkadhum, 2018; Berila & Isufi, 2021a; Berila & Dushi, 2021; Isufi et al., 2021):

$$L_{\lambda} = M_L \cdot Q_{cal} + A_L \quad (1)$$

where:

L_{λ} – TOA spectral radiance [$W \cdot m^{-2} \cdot sr^{-1} \cdot \mu m^{-1}$],

M_L – band-specific multiplicative rescaling factor from the metadata,

Q_{cal} – quantized and calibrated standard product pixel values (DN),

A_L – band-specific additive rescaling factor from the metadata (Salih et al., 2018; Berila & Isufi, 2021a; Isufi et al., 2021; Berila & Dushi, 2021). The metadata of the satellite image is presented in Table 2.

Then, in the Landsat 8 satellite image MTL file, the reflectance rescaling coefficients were obtained. This was done to transform the OLI band into TOA planetary reflection (Adeyeri, Akinsanola & Ishola, 2017). As per the above-mentioned calculation, the following equation was used (Adeyeri et al., 2017):

$$\rho\lambda' = M_p Q_{cal} + A_p \quad (2)$$

where:

$\rho\lambda'$ – TOA planetary reflectance,

M_p – band-specific multiplicative rescaling factor,

A_p – band-specific additive rescaling factor.

Making the correction of TOA reflection with the angle of the sun, then is (USGS, 2019):

$$\rho\lambda = \frac{\rho\lambda'}{\cos(\theta_{sz})} = \frac{\rho\lambda'}{\sin(\theta_{se})} \quad (3)$$

where:

$\rho\lambda'$ – TOA planetary reflectance,

θ_{sz} – local solar zenith angle, $\theta_{sz} = 90^\circ - \theta_{se}$ [$^\circ$],

θ_{se} – local elevation angle of the sun [$^\circ$] (USGS, 2019).

The dark object subtraction (DOS) method was used to remove small reflection values (due to air diffusion) (Chavez, 1996; Adeyeri et al., 2017). We used this method using ENVI 5.3 software as we did not have any other alternative for atmospheric measurements at our disposal (Adeyeri et al., 2017). The equation of an image corrected with DOS is (Adeyeri et al., 2017):

$$L_1 P = L_1 \min - L_1 (DO1\%) \quad (4)$$

where:

$L_1 \min$ – radiance corresponding to the minimum DN from the sum of all the pixels from the image [$W \cdot m^{-2} \cdot sr^{-1} \cdot \mu m^{-1}$],

TABLE 2. Metadata of the satellite image

Band	Variable	Description	Value
10	–	thermal band	–
	K_1	thermal constant	774.8853
	K_2		1321.0789
	M_L	band-specific multiplicative rescaling factor	3.3420E-04
	A_L	band-specific additive rescaling factor	0.10000

$L_1(DO1\%)$ – radiance of the dark object (DO) assumed to have a reflectance of 0.01 [$W \cdot m^{-2} \cdot sr^{-1} \cdot \mu m^{-1}$] (Adeyeri et al., 2017).

In our study we used TIRS Band 10 because of the better performance it has shown compared to Band 11 (Montanaro, Gerace, Lunsford & Reuter, 2014; Adeyeri et al., 2017; Berila & Dushi, 2021).

Calculation of brightness temperature

The next step is to use constant values given in the metadata to convert spectral radiation to brightness temperature (T_b). In order to convert radiance to brightness temperature, Equation (5) has been used in the study (Isaya Ndossi & Avdan, 2016; USGS, 2019; Yuvaraj, 2020; Berila & Dushi, 2021; Isufi et al., 2021).

$$T_b = \frac{K_2}{\ln\left[\frac{K_1+1}{L_\lambda}\right]} \quad (5)$$

where:

- T_b – at-sensor brightness temperature [K],
- L_λ – spectral radiance of thermal Band 10 [$W \cdot m^{-2} \cdot sr^{-1} \cdot \mu m^{-1}$],
- K_1 – band-specific thermal conversion constant from the metadata [$W \cdot m^{-2} \cdot sr^{-1} \cdot \mu m^{-1}$],
- K_2 – band-specific thermal conversion constant from the metadata [K].

From the metadata for the given scene, it is possible and should be derived the values of K_1 and K_2 (Isaya Ndossi & Avdan, 2016; Yakar & Bilgi, 2019).

Estimation of land surface emissivity

To calculate land surface temperature (LST), one of several options that exist is to evaluate land surface emissivity (LSE) through normalized difference vegetation index ($NDVI$) method (Kamran, Pirnazar

& Bansouleh, 2015; Jiménez-Muñoz, Sobrino, Gillespie, Sabol & Gustafson, 2016). The $d\varepsilon$ is the effect of the geometrical distribution of natural surfaces and internal reflections (Igun & Williams, 2018; Carrasco et al., 2020; Isufi et al., 2021; Berila & Dushi, 2021).

To calculate the emissivity, we rely on the following equation:

$$d\varepsilon = (1 - \varepsilon_s)(1 - F_v)F_{\varepsilon_v} \quad (6)$$

where:

- ε_v – vegetation emissivity,
- ε_s – soil emissivity,
- F_v – fractional vegetation,
- F – shape factor whose mean is 0.55 (Sobrino, Jiménez-Muñoz & Paolini, 2004; Igun & Williams, 2018; Guha & Govil, 2020; Berila & Dushi, 2021; Isufi et al., 2021).

$$\varepsilon = \varepsilon_v \cdot F_v + \varepsilon_s(1 - F_v) + d\varepsilon \quad (7)$$

where:

- ε – emissivity.

From Equations (6) and (7), ε may be determined by the following equation (Yuvaraj, 2020; Berila & Dushi, 2021; Isufi et al., 2021):

$$\varepsilon = 0.004 \cdot F_v + 0.989 \quad (8)$$

The proportion of vegetation (F_v) is calculated based on the following equation (Wang et al., 2015; Yuvaraj, 2020; Berila & Dushi, 2021; Isufi et al., 2021):

$$F_v = \left[\frac{NDVI - NDVI_{\min}}{NDVI_{\max} - NDVI_{\min}} \right]^2 \quad (9)$$

The following equation is used to calculate $NDVI$ with the help of Landsat visible Band 4 (Red) and NIR (Band 5) images

(Yuvaraj, 2020; Berila & Dushi, 2021; Isufi et al., 2021):

$$NDVI = \frac{NIR-Red}{NIR+Red} = \frac{Band\ 5-Band\ 4}{Band\ 5+Band\ 4} \quad (10)$$

where:

NIR – near-infrared pixel values,

Red – red band pixel values (Alemu, 2019).

The value of *NDVI* ranges between –1.0 and 1.0 (Alemu, 2019; Yuvaraj, 2020). High *NDVI* values indicate healthy vegetation while low values indicate less or no vegetation (Berila & Dushi, 2021; Isufi et al., 2021).

Calculation of land surface temperature

The final step of estimating *LST* is as follows (Weng, Lu & Schubring, 2004; Alemu, 2019; Yuvaraj, 2020; Berila & Dushi, 2021; Isufi et al., 2021):

$$LST = \frac{T_b}{\{1 + [\lambda \frac{T_b}{\rho}] \ln \varepsilon\}} \quad (11)$$

where:

λ – wavelength of emitted radiance by Landsat 8 ($\lambda = 10.8$ acc. to the NASA) [μm],

T_b – brightness temperature from which the *LST* values [K],

ε – land surface emissivity,

ρ – given by the following equation (Yuvaraj, 2020; Berila & Dushi, 2021; Isufi et al., 2021):

$$\rho = h \frac{c}{\sigma} = 14,388 \mu\text{m} \cdot \text{K}^{-1} \quad (12)$$

where:

h – Planck's constant ($h = 6.626 \cdot 10^{-34}$) [$\text{J} \cdot \text{s}^{-1}$],

σ – Boltzmann constant ($\sigma = 1.38 \cdot 10^{-23}$) [$\text{J} \cdot \text{K}^{-1}$],

c – velocity of light ($c = 2.988 \cdot 10^8$) [$\text{m} \cdot \text{s}^{-1}$] (Alemu, 2019; Yuvaraj, 2020; Berila & Dushi, 2021; Isufi et al., 2021).

There are various factors that can affect the generation and strengthening of *LST*. In this paper we have tried to make a connection between *LST* and population density. To achieve this, *LST* was first calculated – from satellite thermal data – while the population density data by cadastral zones of the Municipality of Prizren were obtained from the 2011 Kosovo Census, classified into four classes – from the least dense to the densest. These data, to have a better presentation on the map, are represented by proportional circles in black (Fig. 5). We have mapped and located these black circles as population density based on the spatial distribution of settlements through a topographic map with a scale of 1:25 000. Through this topographic map, we identified all settlements in each cadastral area of the Municipality of Prizren. And the last step was to place these points in each center of these settlements. This was done to make the relationship between population density and the spatial distribution of *LST* pixel values as real and fair as possible. The next step was to connect these layers of spatial data. For this, we used GIS techniques using ArcGIS 10.5 software. Using this software, we superposed these two layers of spatial data – as seen in Figure 5. All this work has been done to study and highlight the effect and importance of population density – as one of the main factors – in increasing and strengthening the values of *LST*.

Results and discussion

In this paper, the data of the 2011 Kosovo census were used and a map representing the population density and *LST* in the city of

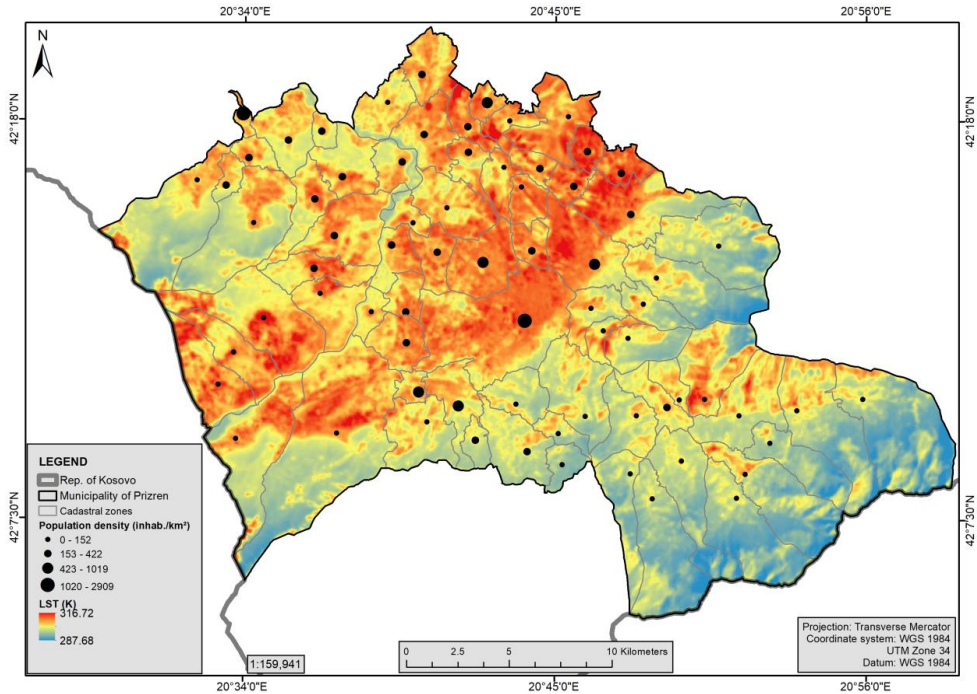


FIGURE 5. Spatial distribution of land surface temperature and population density of Prizren

Prizren was compiled. The population density was classified into four classes, starting from the least dense to the densest. Figure 5 clearly shows that the surfaces with the highest density are mainly the northern and central parts. Making the connection of population density with *LST* we can see that exactly in those areas where the highest population density is distinguished, are the areas (pixels) with the highest *LST* values. Here, the pixels with the lowest values are those with 287.68 K, while the highest values of *LST* reach 316.72 K. It is very important to understand the relationship that exists between *LST* and population density. Figure 5 shows that the lowest values of *LST* have natural surfaces – forests, water surfaces, parks, etc., while, on the other hand, higher values of *LST* can be distinguished in areas where the activities of the population are

prominent and in spaces in which the surface of the earth is bare. Thus, if we compare natural surfaces with artificial ones, we notice that they have lower temperature values because they retain their freshness due to the reflection they make to the solar radiation.

The largest distribution of settlements is in the Prizren plain (center), while in the mountainous parts they begin to decrease. As the center of Prizren has experienced an uncontrolled expansion (especially towards the main arterial roads), the continuous expansion and extension of informal settlements pose a great risk in the loss of agricultural land and its transformation. A transformation of this natural surface is done with surfaces that are impervious, reducing the values of albedo and further strengthening the surface temperature (cause of heat absorption).

To know the relationship between *LST* and population density, and to determine the impact of the latter on the former, Figure 6 presents the regression analysis between these two variables. From the results achieved, a strong positive connection can be noticed between the two. The logarithmic regression (*R*) value is 0.8206 – showing a strong positive relationship. So, with the increase of population density, the values of *LST* are also increasing. This clearly indicates that an increase in population density will inevitably cause an increase in *LST* values. All this happens due to the increase of activities undertaken by the population in these areas.

In all areas with high density, the population takes a series of actions that change the natural surfaces due to the increase in demand. The most noticeable changes are the increase in the use of materials that have low albedo values. These actions are allowed to happen because there is no application of

strict regulation in terms of planning in the city of Prizren. With this unplanned development trend, *LST* values will continue to rise to the extent that the health of the population will be extremely endangered.

The logarithmic regression equation between population density and *LST* is $y = 2.3254 \ln(x) + 295.59$. In addition, through this equation *LST* values can be predicted in case of increase of the (known) population density number for the future. It is population density that explains the variance of *LST* growth in urban areas. In *LST* values of cities, one of the main, important, and representative factors of such a rise is population growth. So, in other words, population density is being presented as the main factor and contributor to this urban change – in relation to the increase in *LST* values (Landsberg, 1981). Separating each factor that contributes to the increase in *LST* values in this major problem is not easy to do. However, one of those factors has shown and

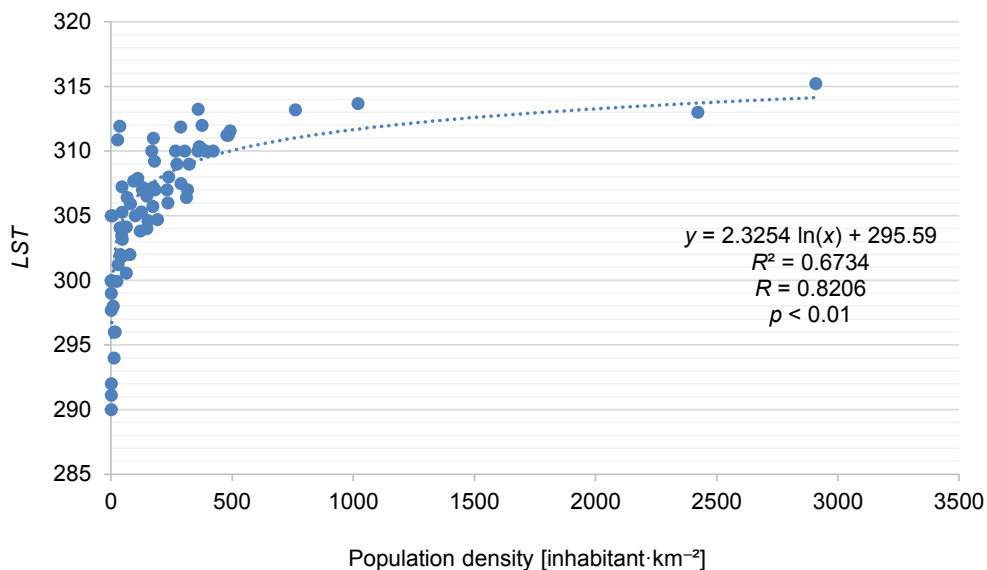


FIGURE 6. Scatter plot between land surface temperature and population density

proved that it has a strong connection with *LST* or the UHI phenomenon is the population density (Lo & Faber, 1998). The small number of meteorological stations in which the temperature of the earth's surface is measured – both in the past and today – is presented as a big obstacle because, in this way, there is no fair and accurate representation for all study area. Facing such situations, the solution is to measure the land's temperature using thermal satellite data. This study clearly presents the spatial change of *LST* in Prizren. One of the main factors that clearly contribute to the increase of *LST* values in our study area is the high population density. This study of ours highlights a close link that exists between *LST* and population density. Statistical analysis of logarithmic regression reveals that the population is a factor that contributes to the increase of *LST* values, thus making the UHI phenomenon to be generated and strengthened precisely in those parts – also creating the microclimate of Prizren.

Similar results as in our paper were seen in the work of Li et al. (2014) on the impact of land cover and population density on soil surface temperature – Wuhan (China). The results of this study showed that the regions with high *LST* were concentrated in residential and industrial areas with low vegetation coverage, in which the population with their activities had made continuous changes. Similar results have been reported by Mallick (2021). In his work on seasonal characteristics of surface temperature with *NDVI* and population density in the National Capital Region (India), he finds that the high population density is one of the main contributing factors in generating and enhancing UHI intensity and in creating a microclimate.

Song et al. (2020) in the study on the effects of building density on soil surface temperature in China, found that in increasing *LST* values, in addition to the density of buildings, climate also plays an important role – the drier the climate, the greater the impact of the density of buildings on increasing *LST* values. Gang, QuiPing, RongBo and DongSheng (2019) in their work on the effects of land use, population density, and altitude on the UHI phenomenon found that *LST* is significantly related to population density, altitude, and proportions of different types of land use. According to them, the larger the artificial surface, the more powerful the UHI intensity and vice versa.

The biggest environmental challenge of the Municipality of Prizren is the irrational use of natural resources, which results in pollution and degradation of the environment, which is affecting the further strengthening of the SUHI phenomenon. The unplanned development of agricultural land resulting from the use of it for the construction of settlements along the main regional roads has resulted in a major loss – it should be borne in mind that any change and replacement of natural to artificial areas only contributes to the deterioration of the situation with SUHI.

Conclusions

This study of ours uses geospatial technology to present as clearly and correctly as possible the spatial distribution of *LST* and its relationship with the density of the population living in Prizren. The satellite image on 8 August 2021 was used to determine the impact of population density on the strengthening of the earth's surface temperature. To do this, *LST* was calculated and Landsat 8

TIRS and OLI bands were used. For the entire Municipality of Prizren, *LST* showed that it has a great connection with vegetation, strengthening once again what is now known that the greener areas, the fresher it will be and vice versa. On the other hand, the cartographic representation of the spatial distribution of *LST* clearly showed that areas in which the population density is high increase the impact of the SUHI effect. All areas affected by the SUHI phenomenon were identified for the entire Municipality of Prizren. These areas are located mainly in the north, center, and west. It is in these areas that the density and activities of the population are most pronounced. Based on this, we conclude that areas in which the population density is high have a significant effect on the generation and strengthening of the phenomenon harmful to the population such as SUHI.

The importance of the maps in which the SUHI phenomenon is defined is also shown by our study. This is because it becomes possible to identify all areas in which this harmful phenomenon causes concern for residents living. Also, these types of maps help municipal administrators to act against this phenomenon in those areas where *LST* values are high, such as replacing black materials with materials with high albedos, expanding of green areas, the expansion of water areas for more freshness, the application of green roofs and a series of other actions which make the life of these citizens healthier.

We raise the concern for policymakers in the Municipality of Prizren to take all steps which minimize the SUHI effect as soon as possible. Studies like ours should raise the alarm in the whole human society for a better life. At the same time, we need strict control of all actions of the population because this

trend of increasing population density, increasing demand for water, land, energy, etc., which is characterizing Prizren, will make its surroundings lose its existing green spaces. Based on this, the authors raise alarm and concern to government institutions to take all this information in this paper with the utmost seriousness and use it for all future activities which are planned to take place in Prizren.

References

- Adeyeri, O. E., Akinsanola, A. A. & Ishola, K. A. (2017). Investigating surface urban heat island characteristics over Abuja, Nigeria: Relationship between land surface temperature and multiple vegetation indices. *Remote Sensing Applications: Society and Environment*, 7, 57–68.
- Alemu, M. M. (2019). Analysis of Spatio-Temporal Land Surface Temperature and Normalized Difference Vegetation Index Changes in the Andassa Watershed, Blue Nile Basin, Ethiopia. *Journal of Resources and Ecology*, 10 (1), 77–85.
- Berila, A. & Dushi, M. (2021). Measuring Surface Urban Heat Island in response to population density based on Remote Sensing data and GIS techniques: application to Prishtina, Kosovo. *Folia Geographica*, 63 (2), 38–57.
- Berila, A. & Isufi, F. (2021a). Two decades (2000–2020) measuring urban sprawl using GIS, RS and landscape metrics: a case study of Municipality of Prishtina (Kosovo). *Journal of Ecological Engineering*, 22 (6), 114–125.
- Berila, A. & Isufi, F. (2021b). Mapping summer SUHI and its impact on the environment using GIS and Remote Sensing techniques: a case study on Municipality of Prishtina (Kosovo). *European Journal of Geography*, 12 (3), 113–129.
- Buyantuyev, A. & Wu, J. (2009). Urban heat islands and landscape heterogeneity: linking spatiotemporal variations in surface temperatures to land-cover and socioeconomic patterns. *Landscape Ecology*, 25 (1), 17–33.

- Carrasco, R. A., Pinheiro, M. M. F., Junior, J. M., Cicerelli, R. E., Silva, P. A., Osco, L. P. & Ramos, A. P. M. (2020). Land use/land cover change dynamics and their effects on land surface temperature in the western region of the state of São Paulo, Brazil. *Regional Environmental Change*, 20 (3), 1–12.
- Chavez, P. S. (1996). Image-based atmospheric corrections – revisited and improved. *Photogrammetric Engineering and Remote Sensing*, 62 (9), 1025–1036.
- Clay, R., Guan, H., Wild, N., Bennett, J., Vinodkumar & Ewenz, C. (2016). Urban Heat Island traverses in the City of Adelaide, South Australia. *Urban Climate*, 17, 89–101.
- Despini, F., Ferrari, C., Bigi, A., Libbra, A., Teggi, S., Muscio, A. & Ghermandi, G. (2016). Correlation between remote sensing data and ground based measurements for solar reflectance retrieving. *Energy and Buildings*, 114, 227–233.
- Fabrizi, R., Bonafoni, S. & Biondi, R. (2010). Satellite and ground-based sensors for the urban heat island analysis in the city of Rome. *Remote Sensing*, 2 (5), 1400–1415.
- Gang, W., QiuPing, Z., RongBo, X. & Dong-Sheng, G. (2019). On impacts of land use, population density and altitude on the urban heat island. *Journal of Yunnan University – Natural Sciences Edition*, 41 (1), 82–90.
- Guha, S. & Govil, H. (2020). Land surface temperature and normalized difference vegetation index relationship: a seasonal study on a tropical city. *SN Applied Sciences*, 2 (10), 1–14.
- Harlan, S. L. & Ruddell, D. M. (2011). Climate change and health in cities: impacts of heat and air pollution and potential co-benefits from mitigation and adaptation. *Current Opinion in Environmental Sustainability*, 3 (3), 126–134.
- Igun, E. & Williams, M. (2018). Impact of urban land cover change on land surface temperature. *Global Journal of Environmental Science and Management*, 4 (1), 47–58.
- Isaya Ndossi, M. & Avdan, U. (2016). Application of open source coding technologies in the production of Land Surface Temperature (LST) maps from Landsat: a PyQGIS plugin. *Remote Sensing*, 8 (5), 413. <https://doi.org/10.3390/rs8050413>
- Iusufi, F., Berila, A. & Bulliqi, S. (2021). Measuring UHI using Landsat 8 OLI and TIRS data with NDVI and NDBI in Municipality of Prishtina. *Disaster Advances*, 14 (11), 25–36.
- Jiménez-Muñoz, J. C., Sobrino, J. A., Gillespie, A., Sabol, D. & Gustafson, W. T. (2006). Improved land surface emissivities over agricultural areas using ASTER NDVI. *Remote Sensing of Environment*, 103 (4), 474–487.
- Käfer, P. S., Rolim, S. B. A., Diaz, L. R., Rocha, N. S. da, Iglesias, M. L. & Rex, F. E. (2020). Comparative analysis of split-window and single-channel algorithms for land surface temperature retrieval of a pseudo-invariant target. *Boletim de Ciências Geodésicas*, 26 (2), 1–17.
- Kamran, K. V., Pirnazar, M. & Bansouleh, V. F. (2015). Land surface temperature retrieval from Landsat 8 TIRS: comparison between split window algorithm and SEBAL method. *Third International Conference on Remote Sensing and Geoinformation of the Environment (RSCy2015)*, 9535, 11–22.
- Landsberg, H. E. (1981). *The urban climate*. Cambridge, MA: Academic Press.
- Li, L., Tan, Y., Ying, S., Yu, Z., Li, Z. & Lan, H. (2014). Impact of land cover and population density on land surface temperature: case study in Wuhan, China. *Journal of Applied Remote Sensing*, 8 (1), 084993. <https://doi.org/10.1117/1.JRS.8.084993>
- Lo, C. & Faber, J. B. (1998). Integration of landsat thematic mapper and census data for quality of life assessment. *Remote Sensing of Environment*, 62 (2), 143–157.
- Mallick, J. (2021). Evaluation of Seasonal Characteristics of Land Surface Temperature with NDVI and Population Density. *Polish Journal of Environmental Studies*, 30 (4), 3163–3180.
- Mohajerani, A., Bakaric, J. & Jeffrey-Bailey, T. (2017). The urban heat island effect, its causes, and mitigation, with reference to the thermal properties of asphalt concrete. *Journal of Environmental Management*, 197, 522–538.
- Montanaro, M., Gerace, A., Lunsford, A. & Reuter, D. (2014). Stray light artifacts in imagery from the Landsat 8 thermal infrared sensor. *Remote Sensing*, 6 (11), 10435–10456.

- Morefield, P., Fann, N., Grambsch, A., Raich, W., & Weaver, C. (2018). Heat-related health impacts under scenarios of climate and population change. *International Journal of Environmental Research and Public Health*, 15 (11), 2438. <https://doi.org/10.3390/ijer-ph15112438>
- Nichol, J. E., Fung, W. Y., Lam, K. & Wong, M. S. (2009). Urban heat island diagnosis using ASTER satellite images and “in situ” air temperature. *Atmospheric Research*, 94 (2), 276–284.
- Peres, L. F., Lucena, A. J., Rotunno Filho, O. C. & Almeida França, J. R. de (2018). The urban heat island in Rio de Janeiro, Brazil, in the last 30 years using remote sensing data. *International Journal of Applied Earth Observation and Geoinformation*, 64, 104–116.
- Pour, T. & Voženilek, V. (2020). Thermal data analysis for urban climate research: A case study of Olomouc, Czechia. *Geographia Cassoviensis*, 14 (1), 77–91.
- Roth, M., Oke, T. R., & Emery, W. J. (1989). Satellite-derived urban heat islands from three coastal cities and the utilization of such data in urban climatology. *International Journal of Remote Sensing*, 10 (11), 1699–1720.
- Salih, M. M., Jasim, O. Z., Hassoon, K. I. & Abdalkadhum, A. J. (2018). Land surface temperature retrieval from LANDSAT-8 thermal infrared sensor data and validation with infrared thermometer camera. *International Journal of Engineering & Technology*, 7 (4.20), 608–612.
- Santamouris, M., Synnefa, A. & Karlessi, T. (2011). Using advanced cool materials in the urban built environment to mitigate heat islands and improve thermal comfort conditions. *Solar Energy*, 85 (12), 3085–3102.
- Sherafati, S., Saradjian, M. R. & Rabbani, A. (2018). Assessment of surface urban heat island in three cities surrounded by different types of land-cover using satellite images. *Journal of the Indian Society of Remote Sensing*, 46 (7), 1013–1022.
- Sobrino, J. A., Jiménez-Muñoz, J. C. & Paolini, L. (2004). Land surface temperature retrieval from LANDSAT TM 5. *Remote Sensing of Environment*, 90 (4), 434–440.
- Song, J., Chen, W., Zhang, J., Huang, K., Hou, B. & Prishchepov, A. V. (2020). Effects of building density on land surface temperature in China: Spatial patterns and determinants. *Landscape and Urban Planning*, 198, 103794. <https://doi.org/10.1016/j.landurbplanning.2020.103794>
- UN-HABITAT (2012). *Prizren Municipal Development Plan 2025 Strategic Environmental Assessment (SEA) Report (draft)*. Kosovo. Retrieved from: http://unhabitat-kosovo.org/old/repository/docs/SEA_Prizren_draft_786745.pdf
- United States Geological Survey [USGS] (2019). *Landsat 8 (L8). Data Users Handbook*. LSDS-1574. Ver. 5.0. USGC EROS Center, Sioux Falls, SD. Retrieved from: https://prd-wret.s3.us-west-2.amazonaws.com/assets/palladium/production/atoms/files/LSDS-1574_L8_Data_Users_Handbook-v5.0.pdf
- Universiteti Teknik i Stambollit, Urban Design Studio, Plan&Art [UTS, UDS & Plan &Art] (2012). *Plani Zhvillimor i Komunës së Prizrenit 2013–2025*. Retrieved from: https://www.online-transparency.org/repository/docs/Plani_Zhvillimor_i_Komunes_se_Prizrenit_2013-20251.pdf [access 15.02.2021].
- Ursu, C. D. (2019). The Land Surface Temperature evolution (LST) using landsat scenes. Case study: the industrial platform Săvinești. *Geographia Technica*, 14 (2), 131–142.
- Voogt, J. A. & Oke, T. R. (2003). Thermal remote sensing of urban climates. *Remote Sensing of Environment*, 86 (3), 370–384.
- Wang, F., Qin, Z., Song, C., Tu, L., Karnieli, A. & Zhao, S. (2015). An improved mono-window algorithm for Land Surface Temperature retrieval from Landsat 8 thermal infrared sensor data. *Remote Sensing*, 7 (4), 4268–4289.
- Wang, H., Zhang, Y., Tsou, J. & Li, Y. (2017). Surface urban heat island analysis of Shanghai (China) based on the change of land use and land cover. *Sustainability*, 9 (9), 1538. <https://doi.org/10.3390/su9091538>
- Weng, Q., Lu, D. & Schubring, J. (2004). Estimation of land surface temperature-vegetation abundance relationship for urban heat island studies. *Remote Sensing of Environment*, 89 (4), 467–483.
- Yakar, İ. & Bilgi, S. (2019). Land Surface Temperature mapping by the use of Remote Sensing and GIS: case study of Istanbul

metropolitan area. In H. M. Yılmaz et al. (eds.), *X. Teknik Sempozyumu. Türkiye Ulusal Fotogrametri ve Uzaktan Algılama Birliği* (pp. 77–81). Aksaray: Basım.

Yuan, F. & Bauer, M. E. (2007). Comparison of impervious surface area and normalized difference vegetation index as indicators of surface urban heat island effects in Landsat imagery. *Remote Sensing of Environment*, 106 (3), 375–386.

Yuvaraj, R. M. (2020). Extents of Predictors for Land Surface Temperature Using Multiple Regression Model. *The Scientific World Journal*, 2020, 3958589. <https://doi.org/10.1155/2020/3958589>

Summary

Determining the influence of population density on the land surface temperature based on remote sensing data and GIS techniques: application to Prizren, Kosovo. The whole study was conducted for the Municipality of Prizren and aims to determine the effect that the population density has on land surface temperature (*LST*). All this was achieved through the connection of *LST* and population density. The free Landsat 8 satellite image downloaded

from the United States Geological Survey website was used and then processed using GIS and remote sensing techniques. To understand this relationship, we performed a regression analysis. This analysis showed a strong positive relationship with a value of $r = 0.8206$, emphasizing the important role that the population has in creating empowering areas that generate surface urban heat island (SUHI) effect. The results of the study clearly showed that in the northern, central, and western parts there are pixels with high *LST* values. This presentation corresponds with the population density, which means that it is precisely the actions of the population that help generate, display, and strengthen the harmful effect of the SUHI. The map in which the areas of high *LST* pixels are clearly identified is of great importance to the policymakers and urban planners of Prizren so that they can orient themselves in these areas and take all actions necessary to minimize this harmful effect which is worrying citizens. If it continues with unplanned development, the peripheral parts of Prizren are seriously endangered by the damage of the spaces which offer protection (green spaces) from the SUHI phenomenon, and the future generations will suffer even worse than the current ones from these irresponsible actions.

Nguyen Minh NGOC¹✉  <https://orcid.org/0000-0002-2664-5558>

Pham Hong CUONG²

Tran Thanh SON¹

Nguyen Van NAM¹

Nguyen Thanh PHONG¹

¹ Hanoi Architectural University, Vietnam

² Vietnam Academy for Water Resources (KLORCE), Vietnam

EXPERIMENTAL STUDY OF THE HYDRAULIC JUMP LENGTH IN A SMOOTH TRAPEZOIDAL CHANNEL

Key words: jump length, roller length, hydraulic jump, trapezoidal channel, spillway

Introduction

A hydraulic jump is a phenomenon that occurs in an open flow when the flow depth expands suddenly from less than the critical depth to greater than the critical depth (Chow, 2009). The jump in practice has many applications, such as energy dissipation of the flow, sludge thickening unit of water treatment system or water oxygen saturation by mixing air into water etc.

The jump is characterized by three basic parameters, which are the conjugate depths (y_1, y_2) and the jump length. The jump length is distinguished by the length of the roller zone (Giglou, Giglou & Minaei, 2013) and the estimated length of the jump (Movahed, Mozafari, Davoodmaghami & Akbari, 2018).

For rectangular channels, the length of the jump has been studied in many different cases, the equations for calculating the length are very plentiful and the equations have considered many factors affecting the length of the hydraulic jump. Meanwhile, research on the length of the jump in the isosceles trapezoidal channel is still few and studies are still limited, the studies are shown in Table 1.

TABLE 1. The studies of the jump length in the trapezoidal channel

References	Equation	Characteristics
Posey & Hsing (1938)	$L_j = 5y_2 \left(1 + 4 \sqrt{\frac{T_2 - T_1}{T_1}} \right)$ where $T_i = b + 2m \cdot y_i$	Trapezoidal channel, still basin.
Silvester (1964)	$\frac{L_j}{y_2 - y_1} = 7.1(1 + 10M)$ where $M = \frac{m \cdot y_1}{b} < 0.25$	Trapezoidal channel, still basin
Rajaratnam & Subramanya (1968)	$\frac{L_j}{y_1} = 5.08Fr_1 - 7.82$ with $Fr_1 \geq 4.4$	Trapezoidal channel, still basin.
Ohtsu (1976)	$\log_{10} \left(\frac{L_j}{\Delta E} \right) = 1.71\eta + 0.315m + 1.58$ where $\Delta E = E_1 - E_2$ and $\eta = \frac{\Delta H}{E_1}$	Trapezoidal channel, still basin.
Wanoschek & Hager (1989)	$\frac{L_j}{y_1} = 9.75(Fr_1 - 1)^{1.01}$	Trapezoidal channel, still basin.
Afzal & Bushra (2002)	$\frac{L_j}{y_2} = 6.9(1 - \alpha)$ where $\alpha = \frac{y_1}{y_2}$	Trapezoidal channel, still basin.
Kateb (2014)	$\frac{L_j}{y_1} = 9.58Fr_1 - 24.59$ with $\begin{cases} 3.46 \leq Fr_1 \leq 13.17 \\ -0.005 \leq i \leq 0.02 \\ 0.031 \leq M \leq 0.093 \end{cases}$	Trapezoidal channel with angle of side slope 76.2° and bed width 0.2 m.
Siad (2018)	$\frac{L_j}{y_1} = 9.97Fr_1 - 0.307$ with $\begin{cases} 2.09 \leq Fr_1 \leq 10.51 \\ 0.0 \leq X_i \leq 1.0 \end{cases}$ X_i is the distance from the toe of the jump to the end of the trapezoidal channel.	Trapezoidal channel with angle of side slope 73°, bed width 0.2 m and length $L_{j\text{ref}} = 4$ m. This channel is continuous with rectangular channel has dimension of a bed width 0.6 m and length 7 m.
Fatehi Nobarian, Hajikandi, Hassanzadeh & Jamali (2019)	Relationship diagrams between geometric features (L_j and y_2/y_1) and energy of the jump in the trapezoidal channel.	Trapezoidal channel, still basin with three types of side slopes (1 : 1, 1 : 0.58 and 1 : 0.26) and bed width 0.2 m

In this study, we are only focusing on analyzing the length of the jump after a spillway in the horizontal trapezoidal channel with a side slope 1 : 1 and upstream Froude number from 4.0 to 9.0 (steady jump).

Analyzing factors affecting the jump length in the trapezoidal channel

The momentum equation for the roller zone of the hydraulic jump, as flowing:

$$F_1 - F_2 - F_\tau = M_2 - M_1 \quad (1)$$

where:

F_1, F_2 – hydrostatic forces,

M_1, M_2 – momentum fluxes,

(in which Subscripts 1 and 2 represent the upstream and downstream cross-section of the hydraulic jump, respectively).

Equation (1) has been shown in some studies about the hydraulic jump, such as the study of Palermo and Pagliara (2017), Movahed et al. (2018), in which integrated shear stress (F_τ) is determined as follows:

$$F_\tau = \tau_0 \cdot L_r \cdot \bar{P} \quad (2)$$

τ_0 – average shear stress between the two sections 1 and 2,

L_r – roller length,

\bar{P} – averaged of wet perimeter between upstream and downstream sections.

Equation (2) was given by Frank (2016) and Movahed et al. (2018) shown in studies of the hydraulic jump.

According to P_i theorem of Buckingham, using Equation (1) for the horizontal trapezoidal channel, it can be written:

$$f(L_r, y_1, y_2, V_1, m, \rho, g) \quad (3)$$

From Equation (3) to write:

$$\beta \left(\frac{L_r}{y_1}, \frac{y_2}{y_1}, \frac{b}{y_1}, m, Fr_{D1} \right) \quad (4)$$

$$\Rightarrow \frac{L_r}{y_1} = \Phi \left(\frac{y_2}{y_1}, M_1, Fr_{D1} \right) \quad (5)$$

Equation (5) is consistent with experimental studies on the jump length shown in Table 1. Thus, the data that needs to be collected on an experimental model for studying the jump length include the sequent depths (y_1, y_2) and the flow rate (Q).

Experimental setup

Experimental model was set up in the Vietnam Academy for Water Resources (KLOORCE). The model consists of an ogee spillway, a straight-line trapezoidal channel is made of glass with the steel skeleton frame.

The experimental system (Figs. 1 and 2) is designed with the components:

- Experimental tank (1): The water is continuously supplied to the tank by a pump, with a supply flow equal to the flow over the spillway.
- Spillway (2): is an ogee spillway and the dimension of a 45 cm height, a 65 cm width and radius of the toe $R = 1$ m. The water flows through the spillway (2) will create a supercritical flow, thereby making the jump in the trapezoidal channel (3).
- Trapezoidal channel (3): it has a smooth bed, 0.55 m width, 0.8 m depth and 0.4 m length with a side slope $m = 1 : 1$, it is placed horizontally and is set up with the cross-section shown in the section (1–1).
- Downstream step (4): This is a hole 20 cm deeper than the bottom of the channel,

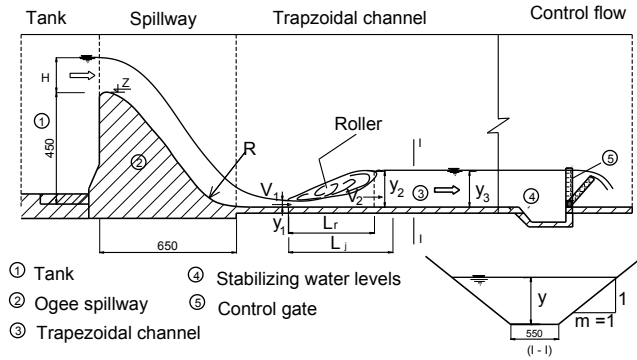


FIGURE 1. Plan of the experimental equipment

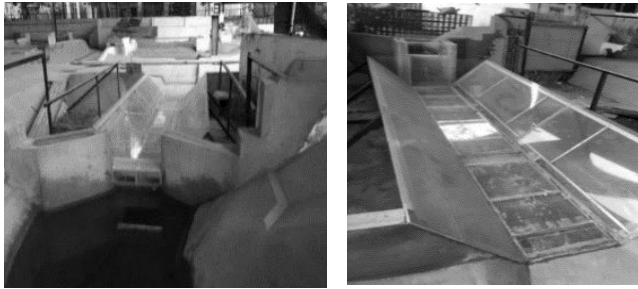


FIGURE 2. Panoramic view of experimental model

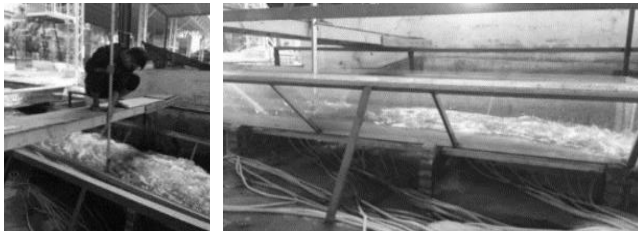


FIGURE 3. Measuring data and hydraulic jump with $Q = 118 \text{ l}\cdot\text{s}^{-1}$ and $Fr_{D1} = 4.19$

used to create flow stability at the end of the experimental model.

- Control gate (5): Controls the change of water level in the channel (3), creating different cases of the jump.

For each case of the jump in the trapezoidal channel, the values to be collected in the experiment include: the flow rate (Q), the conjugate depths (y_1, y_2) and the roller

length (L_r). The conjugate depths were determined through a levelling staff (Fig. 3) and a surveying equipment. The roller length (L_r) is measured with a ruler, initially marking the beginning of the jump (the position with y_1), based on the observation of surface roller and the water surface to determine the end of the roller in the hydraulic jump. The experimental values are shown in Tables 2 and 3.

TABLE 2. Experimental data range

Parameter	Symbol	Unit	Max	Min
Discharge	Q	$\text{m}^3 \cdot \text{s}^{-1}$	0.04	0.193
Initial depth of hydraulic jump	y_2	m	0.03	0.093
Secondary depth of hydraulic jump	y_1	m	0.141	0.396
Upstream Froude number	Fr_{D1}	–	3.5	8.9
Ratio coefficient of side slope and flow depth with bed width	M	–	0.169	0.058

TABLE 3. Data of the hydraulic jump in the trapezoidal channel of bed width $b = 55$ cm

Value	$\frac{L_r}{y_1}$	$M_1 = \frac{m \cdot y_1}{b}$	Fr_{D1}	$\frac{y_2}{y_1}$	$\frac{y_1}{y_2}$
Maximum	34.21	0.17	8.94	10.26	0.29
Minimum	14.49	0.05	3.55	3.48	0.10

Establishing an empirical equation to determine the roller length of the jump

Relationship between the jump length and influential factors

Studying the factors affecting the jump length, MS Excel 2019 software is used to analyze the correlation functions, these relationships are expressed based on the largest coefficient R^2 . The correlation relationships between the characteristics of the jump are shown as follows.

Effect of the conjugate depths

According to Figure 4, the correlation between the roller length (L_r) and the height of the jump ($y_2 - y_1$) is not high, the coefficient R^2 is 0.72.

The height of the jump ($y_2 - y_1$) has a relationship with the jump length, this has been shown in some studies of the jump length. This relationship is shown in Figure 5.

The conjugate depths of the jump and the jump length can have a rather deep relationship, which is shown in the empirical equations for the jump length in rectangular and trapezoidal channels.

The relationship between the jump length and the conjugate depth features is shown in Figure 5 and 6.

From the analysis charts (Figs. 5 and 6), it is found that the relationship between the jump length values and the conjugate depth ratio is very close ($R^2 > 0.9$), which is also shown in the jump length equations in a prismatic channel. When the equation is established to compute the jump length, the ratio of the conjugate depths is also a necessary and important parameter. The relationship between the ratio L_r/y_1 and y_1/y_2 or y_2/y_1 is a nonlinear function.

A general observation of the relationship between the roller length ratio (L_r/y_1) with the sequent depth ratio in Figures 6 and 7 shows that these relationships are very strong, the coefficient $R^2 > 0.9$. Besides, Figure 5 shows

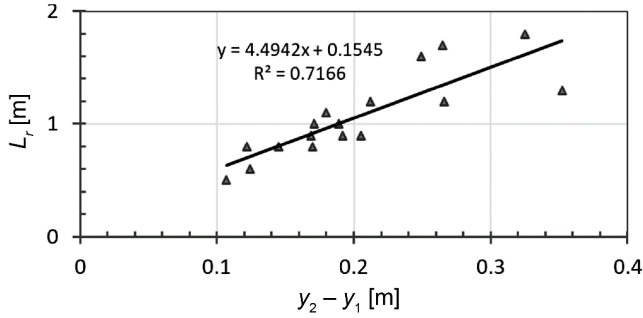


FIGURE 4. Diagram of the relationship between L_r and $y_2 - y_1$

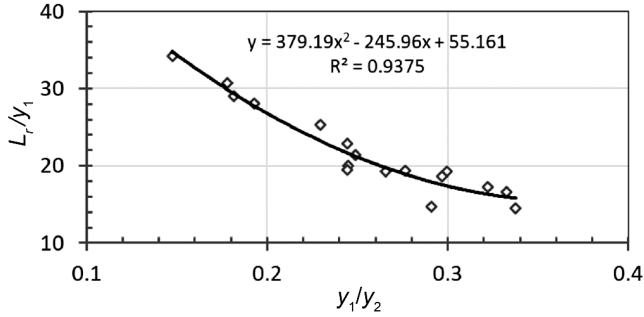


FIGURE 5. Relationship between ratio L_r/y_1 and y_1/y_2

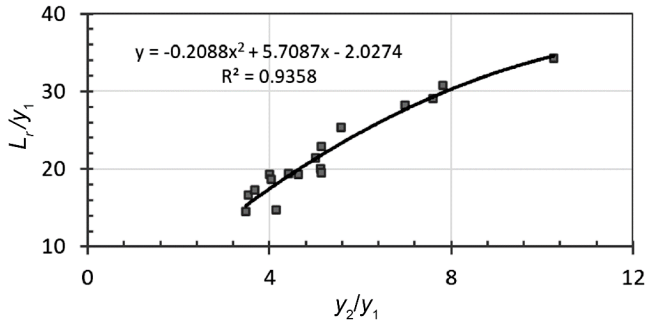


FIGURE 6. Relationship between ratio L_r/y_1 and y_2/y_1

the relationship between the roller length (L_r) and the jump height ($y_2 - y_1$) with the coefficient $R^2 = 0.7$ (moderate correlation). Therefore, a relationship is to be found with a higher correlation coefficient by combining the above analyzes. As a result of that, the

relationship between (L_r/y_1) and $\left(\frac{y_2 - y_1}{y_1}\right)$ is shown as Figure 7.

As shown in Figure 7, the correlation coefficient is very strong, the coefficient R^2 is very large ($R^2 = 0.94$), which shows the close relationship of these factors with each other.

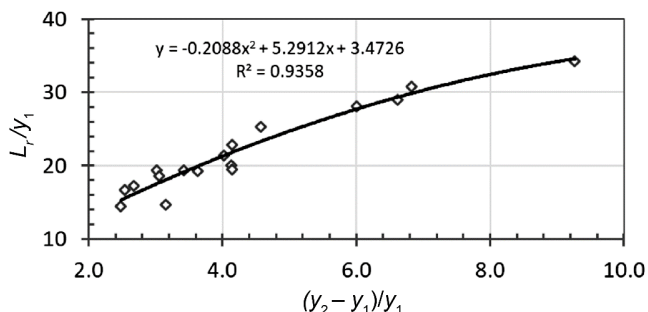


FIGURE 7. Relationship between ratio L_r/y_1 and ratio $(y_2 - y_1)/y_1$

Relationship between the roller length and the inflow Froude number

The inflow Froude number is an important parameter, from Equation (6) it can be seen that the Froude number is closely related to the jump length.

From the experimental data of the physical model, we have the following relationship presented in Figure 8.

The relationship between the ratio (L_r/y_1) and the inflow Froude number (Fr_{D1}) according to Figure 8 is shown that the coefficient R^2 is very strong ($R^2 = 0.93 > 0.9$). Thus, the relationship between the jump length and Froude number tends to converge strongly, which is consistent with some equations for calculating the jump length in prismatic

channels and tends to be similar to studies in the trapezoidal channel of Kateb (2014), Siad (2018), Al-Fatlawi, Al-Mansori and Othman (2020).

Relationship between the roller length and Reynolds number

The Reynolds number is an important parameter in the study of the flow, the Reynolds number characterizes inertial and viscous forces. The Reynolds number is also a characteristic parameter for the flow state. This relationship is expressed in Figure 9.

As shown in Figure 9, the relationship between the jump length and Reynolds number is wide dispersion. Therefore, establishing the relationship between the jump length and the

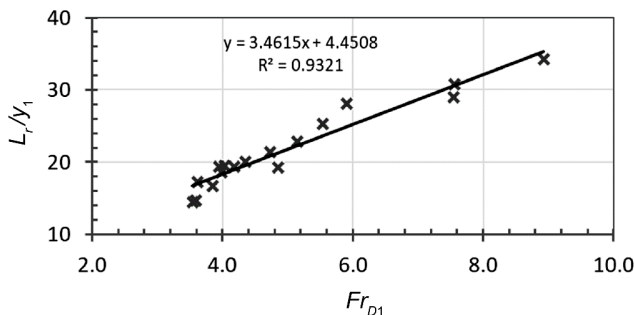


FIGURE 8. The graph of the relationship between the ratio L_r/y_1 and the inflow Froude number (Fr_{D1}) of the jump

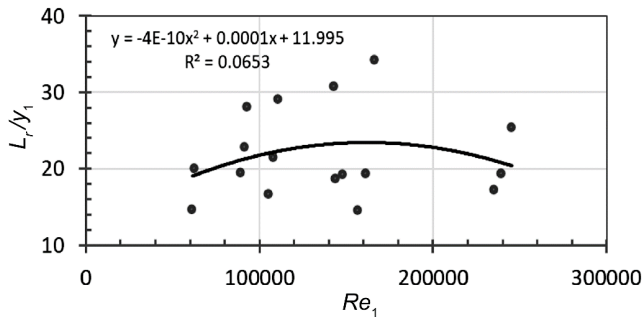


FIGURE 9. Relationship between the ratio L_r/y_1 and the inflow Reynolds number

Reynolds number is not very meaningful and it is difficult to establish the effect of the Reynolds number on the jump length. This parameter is removed when analyzing the influencing factors in the jump length equation.

Relationship between the length and the energy of the hydraulic jump

The jump length and the hydraulic jump energy have a close relationship, which is clearly shown in the empirical equations for the jump length on the prismatic channel. The authors used the energy factor to determine the empirical jump length equation.

Comprehensively, to evaluate the factors affecting the jump length, it is necessary to

define the relationship between the jump length and the hydraulic jump energy. This relationship is shown in Figures 10 and 11.

As the result in Figures 10 and 11, it shows that the jump length is closely related to the hydraulic jump energy, the coefficient R^2 is very strong ($R^2 > 0.9$). The relationship between the jump length and the energy has been demonstrated in the study of Ohtsu (1976). This factor should be included in the jump length equation.

Effecting the second depth on the roller length of the hydraulic jump

From the above, it is shown that the ratio between L_r/y_1 is closely correlated with other hydrodynamic factors of the jump. Consider-

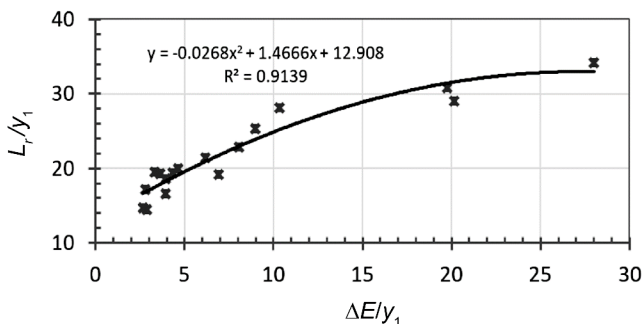


FIGURE 10. Relationship between ratio L_r/y_1 and ratio $\Delta E/y_1$

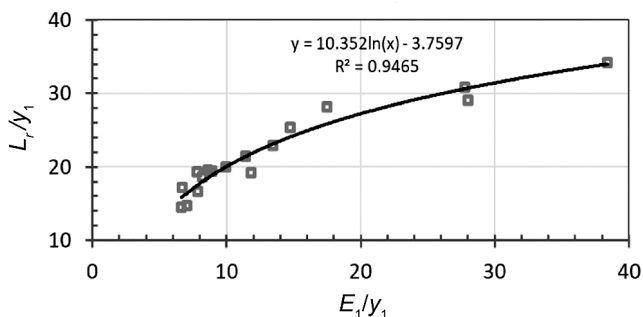


FIGURE 11. Relationship between ratio L_r/y_1 and ratio E_1/y_1

ing further the relationship between the jump length and the downstream hydraulic jump depth (y_2).

As shown in Figures 12, 13 and 14, the coefficients R^2 is very small ($R^2 < 0.5$), the correlation is weak, the graph also shows the

dispersion of experimental points. So, this relationship is not suitable to establish the jump length equation.

From the analysis of empirical relationships, it shows that Equation (6) clearly presents the factors affecting the jump length,

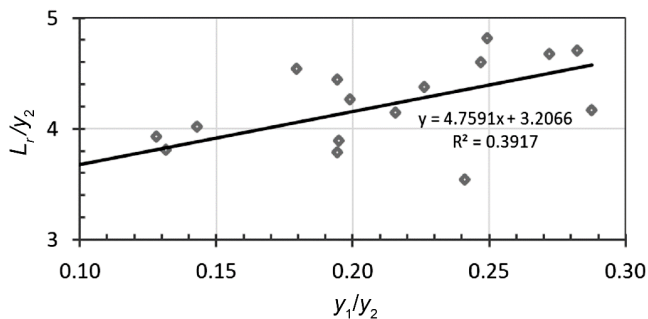


FIGURE 12. Relationship between the ratio L_r/y_2 and y_1/y_2

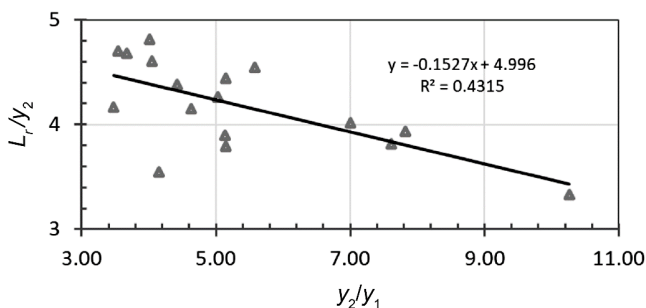


FIGURE 13. Relationship between the ratio L_r/y_2 and y_2/y_1

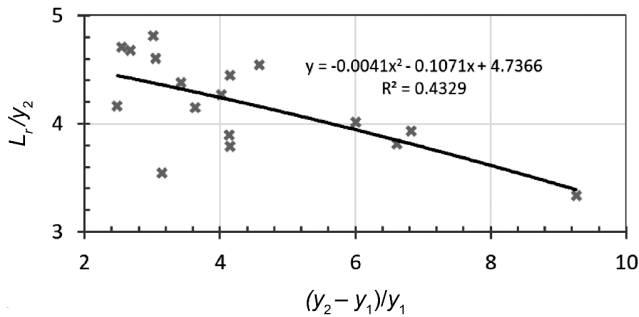


FIGURE 14. Relationship between the ratio L_r/y_2 and the ratio $(y_2 - y_1)/y_1$

thereby determining the basis for establishing empirical equations about the jump length in the smooth trapezoidal channel.

Establishing empirical equations

Based on the analysis of the relationship between the influential factors and the jump length, the measured data on the experimental model and the structure of the existing equations were used to establish the roller length equations in the trapezoidal channel. Analyzing data and to build some empirical equations in Table 4.

Analyzing and evaluating the new experimental equations

Analyzing the observed data

Evaluating the experimental equations (L_r) according to strong statistical indicators (MEA , MSE , $RMSE$, $MAPE$ and R^2) for the experimental data is presented in Table 5.

The observation of Table 5 shows that the coefficients R^2 of the empirical equations are very strong ($R^2 > 0.9$). Evidently, the coefficient R^2 of the empirical equation L_{r4} is not the largest ($R^2 = 0.97$), but the other sta-

TABLE 4. The empirical roller length of the hydraulic jump

Symbol	Equation	R^2	Characteristics
L_{r1}	$\frac{L_r}{y_1} = 2.285 + 2.956Fr_{D1} + 1.896\frac{y_2 - y_1}{y_1} - 0.142\frac{\Delta E}{y_1}$	0.977	–
L_{r2}	$L_r = 1.850(1.716 + 10.872M)(y_2 - y_1)$	0.903	Silvester (1964)
L_{r3}	$\frac{L_r}{y_1} = 4.952Fr_1^{0.986} + 1.679$	0.962	Rajaratnam & Subramanya (1968), Kateb (2014), Siad (2018)
L_{r4}	$\frac{L_r}{y_1} = 6.607\left(\frac{y_2}{y_1}\right)^{0.276}\left(1 - \frac{A_1^2}{A_2^2}\right)Fr_{D1}^{0.484}$	0.970	–

tistical indicators are in best level ($MEA = 0.047$, $MSE = 0.004$, $RMSE = 0.062$ and $MAPE = 4.8\%$), so this equation will be used to analyze the data of Wanoschek and Hager (1989).

TABLE 5. Statistical indicators

Equation	MEA	MSE	RMSE	R ²	MAPE [%]
L_{r1}	0.098	0.015	0.121	0.977	10.395
L_{r2}	0.079	0.012	0.111	0.903	8.138
L_{r3}	0.186	0.043	0.207	0.962	18.333
L_{r4}	0.047	0.004	0.062	0.970	4.846

Analyzing the testing data

Using data from the experiment of Wanoschek and Hager (1989) with the bed width 0.2 m and side slope 1 : 1 to test the proposed equation with the case of Froude numbers from 4.0 to 9.0 and some data with condition $y_1 < 3$ cm is to be removed.

The statistical analysis between the measured and calculated values is in Table 5.

As shown in Table 6, the calculation results of the empirical equation L_{r4} for the test-

ing data gave good results, in which the coefficients R^2 are strong ($R^2 \approx 0.9$), other statistical indicators are also smaller than 0.11 and the $MAPE$ is 6.8%. This shows that the empirical equation L_{r4} is very suitable in calculating the jump length for the trapezoidal channel.

TABLE 6. Statistical indicators by Wanoschek and Hager (1989)

Equation	MEA	MSE	RMSE	R ²	MAPE [%]
L_{r4}	0.097	0.013	0.113	0.892	6.844

The predicted and measured values of the study are very concentrated and maximum error within 10% (Fig. 15).

Applying the empirical equation L_{r4} to the data of Wanoschek and Hager (1989), has shown the agreement between the measured and calculated values, the largest error is 12%.

In general, as the test results in Figures 15 and 16 show that the empirical equation L_{r4} has good reliability when calculating the hydraulic jump roller length in the trapezoidal channel. The calculation data error is about $\pm 10\%$ compared to the observed values.

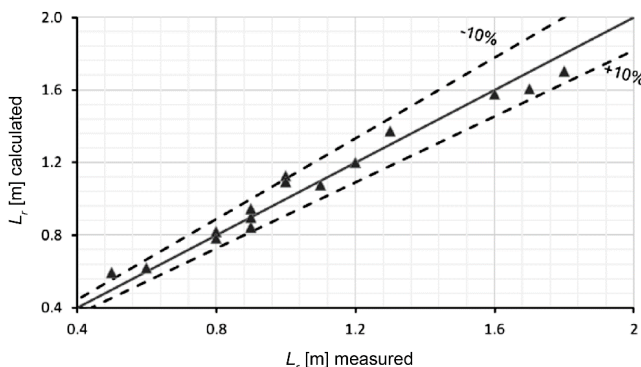


FIGURE 15. Comparison between the observed values and computed by the empirical equation L_{r4}

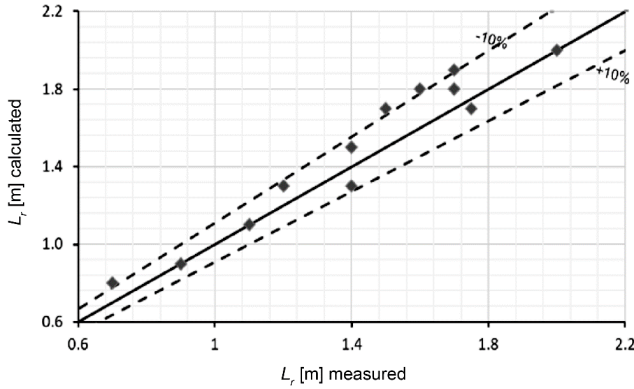


FIGURE 16. Comparison between the observed values (Wanoschek & Hager, 1989) of the testing data and those computed by the empirical equation L_{r4}

Conclusions

Research on determining the roller length in the trapezoidal channel plays an important role in the design of constructions, which uses the phenomenon of the jump. In practice, the jump length is often not determined by theoretical equations, but through experimentation to establish the equations.

In this study, empirical equations to determine the jump length in trapezoidal channel has been established to serve as a basis for studying the factors affecting the jump length.

Since then, statistically, the factors affecting the jump length have been drawn, and through the experimental data of the physical model, the correlation between the roller length and the influential factors have been found. It is relatively shown that close relationship between the hydraulic jump roller length and influential factors were determined. The correlation coefficient of the jump length with the inflow Froude number is $R^2 = 0.935$, with the jump height ($y_2 - y_1$) is $R^2 = 0.904$, with the conjugate depth ratio (y_1/y_2 and y_2/y_1) of $R^2 = 0.9596$ and

$R^2 = 0.972$, respectively, with the energy dissipation ratio ($\Delta E/y_1$) is $R^2 = 0.915$.

Based on the multivariable nonlinear analysis for the factors affecting the jump length, the empirical equation L_{r4} has been established based.

The results of the analysis of statistical indicators show that the empirical equation L_{r4} has the best indicators compared to the remaining equation, such as the coefficient $R^2 = 0.97$ (very strong correlation). The evaluation criteria such as *MEA*, *MSE*, *RMSE*, have values of 0.047, 0.004 and 0.062, respectively, which is the smallest in comparison to all equations, especially the mean absolute percentage error is very small (*MAPE* = 4.8%). Thus, the empirical equation L_{r4} has great efficiency in calculating the jump length in the trapezoidal channel.

The result of testing with data of Wanoschek and Hager (1989) also showed that the calculation efficiency of the formula is very strong: the $R^2 \approx 0.9$ (strong correlation); other statistical indicators are also very close to zero (*MEA* = 0.097, *MSE* = 0.013); the *MAPE* is very small (6.8%).

In this study, it is proposed to use the empirical equation L_{r4} to calculate the hydraulic jump roller length in a horizontal trapezoidal channel in the case with the side slope 1 : 1 and the inflow Froude number from 4.0 to 9.0 (the steady jump). From there, it will serve as a basis for the design of the energy dissipation construction or the other constructions using the hydraulic jump phenomenon.

References

- Afzal, N. & Bushra, A. (2002). Structure of the turbulent hydraulic jump in a trapezoidal channel. *Journal of Hydraulic Research*, 40 (2), 205–214.
- Al-Fatlawi, T. J., Al-Mansori, N. J. & Othman, N. Y. (2020). Laboratory study of stilling basin using trapezoidal bed elements. *Scientific Review Engineering and Environmental Sciences*, 29 (4), 409–420.
- Chow, V. T. (2009). *Open channel hydraulic*. Caldwell: The Blackburn Press.
- Fatehi Nobarian, B., Hajikandi, H., Hassanzadeh, Y. & Jamali, S. (2019). Experimental and analytical investigation of secondary current cells effects on hydraulic jump characteristics in trapezoidal channels. *Tecnologia y ciencias del agua*, 10 (3), 190–218.
- Frank, M. W. (2016). *Fluid mechanics*. New York: McGraw-Hill Education.
- Giglou, A. N., Giglou, T. N. & Minaei, A. (2013). Analytical analysis of the hydraulic jump roller length in open channel. *Life Science Journal*, 10 (6s), 669–673.
- Kateb, S. (2014). *Etude theorique et experimentale de quelques types de ressauts hydrauliques dans un canal trapezoidal [Theoretical and experimental study of some types of hydraulic jumps in a trapezoidal channel]* (PhD thesis). The University of Mohamed Khider Biskra, Biskra.
- Movahed, S. A. M., Mozaffari, J., Davoodmashghi, D. & Akbari, M. (2018). A semi-analytical equation to estimate hydraulic jump length. *Periodica Polytechnica Civil Engineering*, 62 (4), 1001–1006.
- Ohtsu, I. (1976). Free hydraulic jump and submerged hydraulic jump in trapezoidal and rectangular channels. *Proceedings of the Japan Society of Civil Engineers*, 1976 (246), 57–72.
- Palermo, M. & Pagliara, S. (2017). A review of hydraulic jump properties on both smooth and rough beds in sloping and adverse channels. *Acta Scientiarum Polonorum. Formatio Circumiectus*, 16 (1), 91–105.
- Posey, C. J. & Hsing, P. S. (1938). Hydraulic jump in trapezoidal channel. *Engineering News Record*, 121, 797–798.
- Rajaratnam, N. & Subramanya, K. (1968). Profile of the hydraulic jump. *Journal of the Hydraulics Division*, 94 (3), 663–674.
- Siad, R. (2018). *Hydraulic jump in a sharply widened trapezoidal channel* (doctoral thesis). The University of Mohamed Khider Biskra, Biskra.
- Silvester, R. (1964). Hydraulic jump in all shapes of horizontal channels. *Journal of the Hydraulics Division*, 90 (1), 23–55.
- Wanoschek, R. & Hager, W. H. (1989). Hydraulic jump in trapezoidal channel. *Journal of Hydraulic Research*, 27 (3), 429–446.

Summary

Experimental study of the hydraulic jump length in a smooth trapezoidal channel. The paper showed the result of investigation of the hydraulic jump length in a trapezoidal channel. In this study, the basic factors that affect the length (L_j) and roller length (L_r) of the hydraulic jump were investigated by a physical trapezoidal channel's model. The experiment carried out in purpose to establish a new empirical equation for calculating the roller length (L_r) of the jump in the horizontal trapezoidal channel with the upstream Froude number 4.0 to 9.0 (the steady jump). The hydraulic characteristics of forced jump were measured and statistically calculated using MS Excel software. The results of data analysis showed

that the *MAPE* was relatively small ($< 5\%$), and $R^2 > 0.9$ (strong correlation between predicted and observed values) and other statistical indicators are less than 0.1 ($MSE = 0.004$, $RMSE = 0.062$, $MEA = 0.047$). Therefore, the equation found could be appropriated and applied to calculate characteristics of hydraulic jump trapezoidal channel.

Instruction for Authors

The journal publishes in English languages, peer-reviewed original research, critical reviews and short communications, which have not been and will not be published elsewhere in substantially the same form. Author of an article is required to transfer the copyright to the journal publisher, however authors retain significant rights to use and share their own published papers. The published papers are available under the terms of the principles of Open Access Creative Commons CC BY-NC license. The submitting author must agree to pay the publication charge (see Charges).

The author of submitted materials (e.g. text, figures, tables etc.) is obligated to restricts the publishing rights. All contributors who do not meet the criteria for authorship should be listed in an Acknowledgements section of the manuscript. Authors should, therefore, add a statement on the type of assistance, if any, received from the sponsor or the sponsor's representative and include the names of any person who provided technical help, writing assistance, editorial support or any type of participation in writing the manuscript.

Uniform requirements for manuscripts

The manuscript should be submitted by the Open Journal System (OJS) at <https://srees.sggw.edu.pl/about/submissions>. All figures and tables should be placed near their reference in the main text and additionally sent in a form of data files (e.g. Excel, Visio, Adobe Illustrator, Adobe Photoshop, CorelDRAW). Figures are printed in black and white on paper version of the journal (color printing is combined with an additional fee calculated on a case-by-case basis), while on the website are published in color.

The size of the manuscript should be limited up to 10 pages including overview, summary, references and figures (the manuscript more than 13 pages is unacceptable); Please set the text format in single column with paragraphs (A4 paper format), all margins to 25 mm, use the font Times New Roman, typeface 12 points and line spacing one and half.

The submitted manuscript should include the following parts:

- name and SURNAME of the author(s) – up to 5 authors
- affiliation of the author(s), ORCID Id (optional)
- title of the work
- key words
- abstract (about 500 characters)
- text of the paper divided into: Introduction, Material and Methods, Results and Discussion, Conclusions, References and Summary
- references in APA style are listed fully in alphabetical order according to the last name of the first author and not numbered; please find the details below
- post and mailing address of the corresponding author:

Author's address:

Name, SURNAME

Affiliation

Street, number, postal code, City

Country

e-mail: address@domain

- Plagiarism statement (<https://srees.sggw.edu.pl/copyright>)

Reference formatting

In the Scientific Review Engineering and Environmental Sciences the APA 6th edition style is used.

Detailed information

More information can be found: <https://srees.sggw.edu.pl>

